Stability Analysis and Reduced Order Modeling of a Separating Shear Flow

by

Daehyun Wee

B.S., Mechanical Engineering (1996)
Seoul National University

Submitted to the Department of Mechanical Engineering
in Partial Fulfillment of the Requirements for the Degree of

Master of Science in Mechanical Engineering

at the

Massachusetts Institute of Technology

June 2002

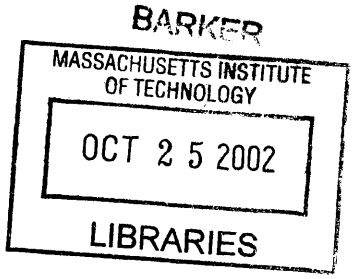

Signature of Author .....
Department of Mechanical Engineering
May 24, 2002

Certified by .....
Anuradha M. Annaswamy
Principal Research Scientist and Lecturer
Thesis Supervisor

Certified by .....
Ahmed F. Ghoniem
Professor
Thesis Supervisor

Accepted by .....
Ain A. Sonin
Chairman, Department Committee on Graduate Students

Stability Analysis and Reduced Order Modeling of a Separating Shear Flow

by

Daehyun Wee

Submitted to the Department of Mechanical Engineering
on May 24, 2002, in Partial Fulfillment of the
Requirements for the Degree of
Master of Science in Mechanical Engineering

Abstract

Thermoacoustic instability in premixed combustors occurs occasionally at multiple frequencies, especially in configurations where flames are stabilized on separating shear layers that form downstream of sudden expansions or bluff bodies. While some of these frequencies are related to the acoustic field, others appear to be related to shear flow instability phenomena. It is shown in this paper that shear flows can support self-sustained instabilities if they possess absolutely unstable modes. The associated frequencies are predicted using mean velocity profiles that resemble those observed in separating flows, and are shown to match those derived from experimental and numerical investigations. It is also shown that the presence of density profiles compatible with premixed combustion can affect this frequency and can change the absolute instability mode into a convectively unstable mode thereby reducing the possibility of the generation of self-sustained oscillations.

The results from the stability analysis are combined with POD-Galerkin procedure to yield a reduced-order model. For POD-Galerkin procedure, we tested two different methods. One is the conventional 'standard' procedure, and the other is a modified version using 'nested spatial weighting'. The later one is shown to be more effective to suppress the effect of extended domain of simulation and that of uncertain downstream boundary condition at the same time. This method can be easily adopted for other problems sharing the same issues.

Thesis Supervisor: Anuradha M. Annaswamy
Title: Principal Research Scientist and Lecturer

Thesis Supervisor: Ahmed F. Ghoniem
Title: Professor

Acknowledgments

First, I would like to thank Professor Annaswamy and Professor Ghoniem for their guidance through the past 2 years. Their efforts have been invaluable resources to carry out my research.

I owe a great deal to my colleagues, Youssef Marzouk, Sungbae Park and Tongxun Yi. Youssef and Sungbae shared their valuable time for discussion on the topics included in this thesis, and Tongxun provided results from his numerical simulation of backward-facing step flows.

I am very grateful to my parents, Youngin Wee and Hearyan Koh, for their love, support and guidance. I also thank other members of my family, including my brother and grandparents. Special thanks to my wife, Jiheyon Kim, for her support during the past years.

I also want to thank Ms. Leslie Regan, who gave me two additional weeks to revise this thesis after the official due date. I'm sure that this thesis would be much worse without all those improvements made during that period.

Finally, I thank Professor Chomsky in Department of Linguistics and Philosophy for his presence in MIT. Although he will never know that I mentioned him in this short series of acknowledgements, his keen discernment and unyielding courage makes me feel proud of being a member of this institute more than any technical and scientific achievement made by the institute does.

This work has been sponsored by the National Science Foundation, grant no. ECS 9713415, and the Office of Naval Research, grant no. N00014-99-1-0448, and the Air Force Office of Sponsored Research, F49620-00-C-0038.

Contents

I Introduction

Thermoacoustic instability, which manifests itself as growing pressure oscillations, is predominantly due to destabilizing interactions between acoustics and heat-release rate perturbations. Characterized by a positive Rayleigh index, obtained when the pressure and heat release perturbations are in phase, the instability occurs normally at frequencies that are associated with acoustic modes that can be identified as a longitudinal, azimuthal, or bulk mode depending on the configuration of the combustor. These interactions have been modeled in a number of recent investigations by including acoustics and heat-release dynamics as primary components [1-7].

In some of the combustor configurations, however, the combustion instability occurs at multiple frequencies, not all of which can be identified with acoustics. In these combustors, a "hydrodynamic" instability has been argued to be the source of the oscillation [8-12]. In particular, the phenomenon of vortex shedding has been observed in combustors equipped with sudden expansions, bluff-bodies, swirlers, etc., all of which are utilized for flame stabilization in premixed systems. A representative configuration of these separating flows is a backward-facing step or dump combustor that has been used extensively in experimental and numerical studies, both for non reacting as well as reacting flows [13-16]. The pressure power spectra measured in these experiments often exhibit multiple peaks, some of which are easily related to existing acoustic modes, but others are not. This raises the possibility that other "resonance" phenomena play a role in determining the overall instability characteristics. Whether the resonances form due to acoustic forcing or through other mechanisms has not yet been proven, but the existence of vortices in these cases, which raises the possibility that shear layer dynamics may be involved in the resonance, is confirmed by visualization studies that show flames wrapping around large vortical structures. As summarized by Najm et al. [17], the frequency of the most active oscillations in non reacting flows, or the corresponding vortex shedding frequency, satisfies, in most cases, the criterion $0.05 < St < 0.1$, where the Strouhal number is based on the step height and the mean upstream flow speed. Numerical calculations of the same flow, although they are mostly limited to relatively low Reynolds numbers, reproduce the same result. The question that arises is whether these self-sustained oscillations produced by a hydrodynamic instability can

cause the heat release to be perturbed and as a result feed energy into the acoustic field, thereby producing additional resonant frequencies.

As a representative example of non reacting and reacting flow data, the pressure power spectrum in the experiment of Cohen et al. [13] shows three peaks at 48, 96 and 124 Hz in the reacting flow, and a dominant peak close to 100Hz in the non reacting flow. Solutions, analytical in 1D and numerical in 2D, of the acoustic wave equation predict the presence of the modes at 48 Hz and the 124 Hz, as the quarter mode and three-quarter modes of the system, but not the mode at 96 Hz. Moreover the experimental data show that while these two modes appear as broad peaks, the 96 Hz peak is significantly sharper, implying that the latter is generated perhaps by a different mechanism. It is interesting to note that the 96 Hz mode scales to a Strouhal number of 0.092, indicating that its origin may be related to hydrodynamic instability.

In this thesis, an attempt to derive a reduced-order model of reacting shear flow in a combustor with a backward-facing step is made. Using linear stability theory of shear flow and applying it to separating flows, it is explored whether these flows can support self-sustained oscillations similar to those observed in experimental studies. These results are suitably combined with a POD-based analysis to derive a reduced-order model. In Chapter II, the basic linear stability theory of shear flows is introduced. Using the Green's function for perturbed Euler equation and asymptotic evaluation of integrals, the frequency and the growth rate of the hydrodynamic mode are calculated, and the conditions under which the frequency corresponds to the absolutely unstable mode are delineated. Detailed numerical simulations were performed to obtain the mean velocity profiles, and the results from the linear stability analysis are compared with the numerical results.

Based on the results from Chapter II, using numerical data, a reduced order model is constructed for potential use in active control design using POD-Galerkin procedure in Chapter III. We also address the problem of extended domain of simulation on the procedure, and give a possible solution of the problem, namely, 'nested spatial weighting' approach. We also provide an example of application of this method onto a backward-facing step flow.

II Stability Analysis of Separating Shear Flows

In this section, the separating flow downstream of a backward-facing step is analyzed using linear stability analysis. The objective of the analysis is to determine conditions under which the shear flow can support self-sustained oscillations arising from intrinsic instabilities, even in the absence of upstream perturbations or resonance with other oscillations such as those due to acoustics. These forms of instabilities are known as absolute instability and have been shown to arise in a number of shear flows [18, 19].

This chapter is organized as follows. In Section II.1, basic formulation of linear stability analysis is described. In Section II.2, the concepts discussed in Section II.1 is applied to separating shear flows, and the effect of flow parameters including the local shear layer thickness and the magnitude of the backflow on the local stability properties is examined, and how these local phenomena may be used to predict global properties is explained. The unstable frequency is compared with the predictions obtained from a numerical investigation of the unsteady flow. In Section II.3, the analysis is extended to the case with finite density gradients across the layer to examine the impact of combustion of the absolute stability properties of the flow.

II.1 Formulation of Local Stability Analysis

In this section, we discuss the basic concepts of local stability analysis of shear flows. Section II.1.1 and Section II.1.2 give the basic formulation, which is classical. Readers who are familiar with linear stability analysis may skip these subsections. The part from Section II.1.3 to II.1.4 contains relatively recent results, that is, concepts of absolute and convective instabilities and their relation to the modal decomposition of a solution. Finally, in Section II.1.5, the cusp map method is presented as a simple method to determine the absolute characteristics of a given velocity profile.

II.1.1 Modal Analysis

Modal analysis is a tool to examine whether a given flow is linearly unstable or not. Let α be the wave number and ω be the frequency. c stands for the phase speed, $c = \omega/\alpha$. If it has an unstable mode, which has positive growth rate ω_i, the flow is said to be unstable. If not, the flow is stable.

We perform modal analysis in a 2-D inviscid flow, which is assumed to have a basic steady parallel flow $U(y)$. The streamwise coordinate is defined as the x-axis, and the other direction is defined as the y-axis. The governing equation for this flow is the Euler equation, which can be wrtitten in the following form.

$$\left[\frac{\partial}{\partial t}+\frac{\partial \Psi}{\partial y}\frac{\partial}{\partial x}-\frac{\partial \Psi}{\partial x}\frac{\partial}{\partial y}\right]\nabla^2\Psi = 0, \tag{1}$$

where $\Psi(x,y,t)$ is the stream function for the system. The scalar vorticity is given by $-\nabla^2\Psi$. The velocity field can be recovered as $u = \frac{\partial \Psi}{\partial y}$ and $v = -\frac{\partial \Psi}{\partial x}$.

To study stability, we separate the perturbed flow field from the mean flow field, so that we have

$$\Psi(x,y,t) = \overline{\Psi}(x,y) + \psi(x,y,t). \tag{2}$$

From the mean velocity profile, we get the following condition.

$$\frac{\partial \overline{\Psi}}{\partial x} = 0, \frac{\partial \overline{\Psi}}{\partial y} = U(y). \tag{3}$$

We substitute (2) and (3) into (1). Up to the linear perturbation terms, the equation becomes

$$\left[\frac{\partial}{\partial t}+U(y)\frac{\partial}{\partial x}\right]\nabla^2\psi - U''(y)\frac{\partial \psi}{\partial x} = 0. \tag{4}$$

Using separation of variables, we can assume that

$$\psi(x,y,t) = \phi(y)\exp[i\alpha(x-ct)]. \tag{5}$$

With some simple algebra, we get the Rayleigh equation,

$$\phi'' - \alpha^2\phi - \frac{U''}{U-c}\phi = 0. \tag{6}$$

To solve this equation, we need two boundary conditions. They come from the impermeability conditions at the upper and lower boundaries. They are given by

$$\phi(a) = \phi(b) = 0. \tag{7}$$

where $y = a$ and $y = b$ are the location of the lower and upper boundaries.

The system consisting of (6) and (7) gives a nontrivial solution only for particular pairs of (ω, α). Therefore it forms an eigenvalue problem, which leads to a dispersion relation $D(\alpha, c) = 0$ or equivalently $D(\alpha, \omega) = 0$. If one specify the mean velocity profile $U(y)$, we can solve the eigenvalue problem analytically or numerically, and get the dispersion relation by integration of the equation.

II.1.2 Temporal verses Spatial Analysis

To study the stability of a flow, we need to solve the eigenvalue problem defined by (6) and (7). We have two parameters to be determined, so what we can do is one of the following two things:

(i) Fix α, and obtain the corresponding ω.

(ii) Fix ω, and obtain the corresponding α.

Moreover, we have freedom of choice of α in the case (i) or ω in case (ii) over the whole set of complex numbers. However, we do choose two particular cases usually. One is temporal analysis, where we assume $\alpha \in R$ and try to find out the corresponding complex ω. The other is spatial analysis, where we assume $\omega \in R$ and try to find out the corresponding complex α. In temporal analysis, a mode is called unstable when it has a positive imaginary part of ω. In spatial analysis, a mode is called unstable when it has a negative imaginary part of α. We also call modes with real α as temporal modes, and those with real ω as spatial modes. The growth rate can be defined as the imaginary part ω_i of complex ω for temporal modes. It grows in time with the positive exponent ω_i. For spatial modes, the growth rate should be $-\alpha_i$. It grows in space with the positive exponent $-\alpha_i$.

Although both methods seem to have their own rights, the discrepancy between these two methods can be seen, if we consider modal decomposition of a solution starting from an initial disturbance. In reality, any initial disturbance we can physically specify should be localized, and

if we have localized initial disturbance, the disturbance will propagate with 'finite speed'. As the result of this fact, we must have a solution decaying as $x \to \pm\infty$. In time domain, we don't have to have this restriction. Instead of this locality condition, we have causality condition for time domain, but we don't discuss it here any more.

This locality condition in the space gives superiority to temporal analysis over spatial analysis. For real ω, the wave number α is rather chosen arbitrarily by the dispersion relation, so one cannot assure that it is always possible to find a proper modal decomposition of a localized disturbance. This is a big disadvantage for spatial modal analysis. On the other hand, we can describe any localized solution with the modes with real α. That is, physically meaningful modal decomposition is always possible with temporal modes.

Also, it can be restated as the following statement. For the spatial modes that cannot be used to decompose all physically meaningful solution, we may say that the set of spatial modes contains only part of physically meaningful modes. Instead of those omitted meaningful modes, it contains physically impossible modes. In this sense, spatial analysis is a mathematical artifact. The result from spatial analysis may be accepted only in particular cases, where the temporal analysis result can be recovered with the spatial analysis. Certainly, there are cases where spatial analysis can describe the experimental result much more easily, but the same result should be recovered with an equivalent temporal analysis, at least in principle. This argument can be given in a more sophisticated way. Before the sophistication, the concepts of absolute and convective instabilities should be examined.

II.1.3 Concepts of Absolute and Convective Instabilities

If we induce a localized initial disturbance, it can grow or decay. However, we can also see two different kinds of growth. One is the growth in place, and the other is the growth with movement. This term 'movement' seems ambiguous, but with Figure 1, it becomes clear. The first picture shows a moving envelope of wave packets. The second picture also shows some movement, but there is a great distinction from the first one. One edge of the envelope has a negative velocity, which means we have a growth on the line $x = 0$, so we have a growth in place. On the other hand, in the first picture, we cannot see any growth on the line $x = 0$. We separate these two

cases, and call the case as in the first picture a convectively unstable flow, and call the case as in the second picture an absolutely unstable flow.[1]

It should be noted that the objective of the analysis is to examine the long-term behavior of the flow near the step, i.e. at $x = 0$. From the discussion in the previous paragraph, it is easy to see that if the flow is absolutely unstable, it exhibits growing waves that are not convected out from the observation point, i.e. oscillations may persist, and the flow demonstrates the property of an unstable oscillator. For convectively unstable flows, the input is amplified downstream, and the growing waves are convected out as shown in Figure 1. It is obvious that only in the absolutely unstable case, oscillations persist at a frequency determined by the properties of the flow, i.e. the flow achieves self resonance, while in the convectively unstable case, external forcing or resonance with other oscillators must occur before overall sustained oscillations can be observed.

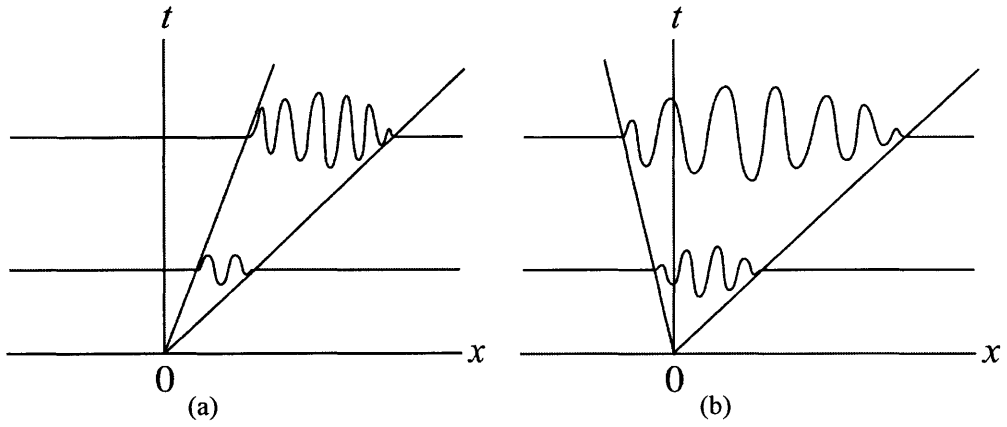

Figure 1 Distinction between two modes of growth: (a) convectively unstable flow; (b) absolutely unstable flow

[1] Note that the adjectives 'convectively unstable' and 'absolutely unstable' are placed before the term 'flow'. Modes cannot be called as absolutely unstable or convectively unstable, because all these concepts are based on group velocity and envelope of wave packets. Monochromatic modes do not satisfy any kind of this classification. Sometimes we use the term 'absolutely unstable mode' or 'absolute mode', but it has a different definition. Note that these concepts are also crucially related to the frame of reference. If we specify different inertial reference frame, the characteristics of absolute and convective instability changes. So, this concept is not Galilean invariant. However, we can determine which reference frame is exceptionally important for most practical cases.

To find out the condition determining the absolute or convective characteristics of a flow, we construct Green's function for (4). We put an impulse input at RHS, so now we have inhomogeneous equation.

$$\left[\frac{\partial}{\partial t}+U(y)\frac{\partial}{\partial x}\right]\nabla^2 G - U''(y)\frac{\partial G}{\partial x} = \delta(t)\delta(x)\delta(y). \tag{8}$$

Taking Fourier transforms in x and t, we have an inhomogeneous ODE with the Rayleigh equation in LHS.

$$\hat{G} - \alpha^2 \hat{G} - \frac{U''}{U-c}\hat{G} = \frac{\delta(y)}{i\alpha(U-c)}. \tag{9}$$

The boundary condition for $\hat{G}$ is given by (7), because the same impermeability condition should be satisfied by the flow described by the Green's function. $\hat{G}$ is related with G by the following inverse Fourier transforms.

$$\begin{aligned} \hat{G}(\alpha,y,t) &= \frac{1}{2\pi}\int_{L_\omega} \hat{G}(\alpha,y,\omega)\, e^{-i\omega t} d\omega \\ G(x,y,t) &= \frac{1}{2\pi}\int_{F_\alpha} \hat{G}(\alpha,y,t)\, e^{i\alpha x} d\alpha \end{aligned} \tag{10}$$

Just as in the case of inverse Laplace transform, the integral path L_ω in (10) should be placed over all singularities in ω plane to meet the causality condition. We are using temporal analysis, so the path F_α should be the real axis in α plane, as we mentioned in the previous section. See Figure 2.

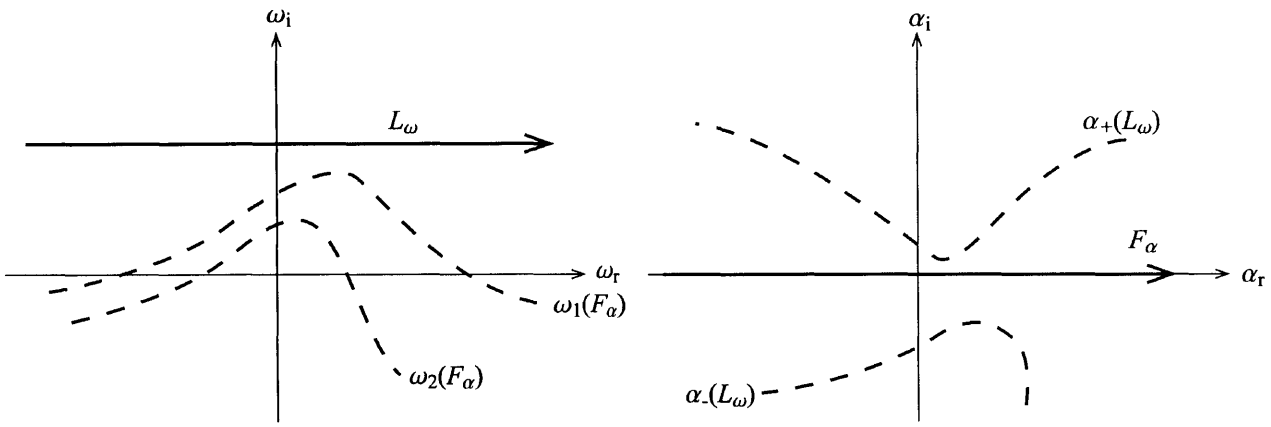

Figure 2 Illustrative sketch of typical integral paths. Dashed curves represent the singularities induced by dispersion relation.

To get the solution of (9) with the boundary conditions (7), we use method of variation of parameters. The homogeneous part of (7) is the Rayleigh equation, and we assume that we already have the solution for the homogeneous part. So, we have two solutions, which satisfy

$$\eta_{yy} - \alpha^2 \eta - \frac{U''}{U-c}\eta = 0. \tag{11}$$

These solutions are denoted by $\eta_1(y;\alpha,\omega)$ and $\eta_2(y;\alpha,\omega)$. These two do not have to satisfy the boundary condition given by (7), but we can make each of them satisfy one of the two boundary conditions by linearly combining the solutions. Hence, we assume that $\eta_1(a;\alpha,\omega) = 0$ and $\eta_2(b;\alpha,\omega) = 0$.

Applying the method of variation of parameters, we have

$$\hat{G}(y) = -\eta_1(y)\int \frac{\eta_2(y')F(y')}{W(y')}dy' + \eta_2(y)\int \frac{\eta_1(y')F(y')}{W(y')}dy', \tag{12}$$

where $F(y) = \delta(y)/\{i\alpha(U-c)\}$, and $W(\alpha,\omega)$ is the Wronskian of $\eta_1(y;\alpha,\omega)$ and $\eta_2(y;\alpha,\omega)$, that is $W = \eta_1\eta_2' - \eta_1'\eta_2$.[2]

The boundary conditions can be used to determine the integration constants below.

$$\hat{G}(y) = -\eta_1(y)\left[\int_{y'=b}^{y} \frac{\eta_2(y')F(y')}{W}dy' + C_1\right] + \eta_2(y)\left[\int_{y'=a}^{y} \frac{\eta_1(y')F(y')}{W}dy' + C_2\right] \tag{13}$$

Fortunately, we already have $\eta_1(a) = 0$ and $\eta_2(b) = 0$, so, for each boundary, we have

$$\begin{aligned}
\hat{G}(a) &= \eta_2(a)\left[\int_{y'=a}^{a} \frac{\eta_1(y')F(y')}{W}dy' + C_2\right] = 0 \\
\hat{G}(b) &= -\eta_1(b)\left[\int_{y'=b}^{b} \frac{\eta_2(y')F(y')}{W}dy' + C_1\right] = 0
\end{aligned} \tag{14}$$

Therefore, C_1 and C_2 are zero. Now, combining everything, the solution is

$$\hat{G}(y) = -\eta_1(y)\left[\int_{y'=b}^{y} \frac{\eta_2(y')F(y')}{W}dy'\right] + \eta_2(y)\left[\int_{y'=a}^{y} \frac{\eta_1(y')F(y')}{W}dy'\right] \tag{15}$$

The sign of the first integral can be changed.

---

[2] The Wronskian is independent of y.

$$-\eta_1(y)\left[\int_{y'=b}^{y}\frac{\eta_2(y')F(y')}{W}dy'\right]=\eta_1(y)\left[\int_{y'=y}^{b}\frac{\eta_2(y')F(y')}{W}dy'\right] \tag{16}$$

Now we can make the two integral into one.

$$\begin{aligned}\hat{G}(y)&=\left[\int_{y'=y}^{b}\frac{\eta_1(y)\eta_2(y')F(y')}{W}dy'\right]+\left[\int_{y'=a}^{y}\frac{\eta_1(y')\eta_2(y)F(y')}{W}dy'\right]\\&=\int_{y'=a}^{b}\frac{H(y,y')}{W}\delta(y')dy'\end{aligned} \tag{17}$$

$$\text{where } H(y,y')=\begin{cases}\dfrac{\eta_1(y)\eta_2(y')}{i\alpha(U(y')-c)} & y<y'\\ \dfrac{\eta_1(y')\eta_2(y)}{i\alpha(U(y')-c)} & y'<y\end{cases}$$

Fortunately, the integral can be evaluated very easily due to the existence of $\delta(y')$ in the integrand.

$$\hat{G}(y)=\int_{y'=a}^{b}\frac{H(y,y')}{W}\delta(y')dy'=\frac{H(y,0)}{W}=\begin{cases}\dfrac{\eta_1(y)\eta_2(0)}{i\alpha(U(0)-c)W} & y<0\\ \dfrac{\eta_1(0)\eta_2(y)}{i\alpha(U(0)-c)W} & 0<y\end{cases} \tag{18}$$

Actually, the Wronskian $W=\eta_1\eta_2'-\eta_1'\eta_2$ is nonzero, when we have linearly independent η_1 and η_2. If we have a nontrivial solution for the homogeneous equation, which satisfies both boundary conditions, upper and lower, then the nontrivial solution, η_{eigen}, can be both η_1 and η_2. In this case, there is no linear independency of η_1 and η_2. Therefore, this concludes that we have zero Wronskian whenever the homogeneous part satisfies the eigenvalue-eigenfunction relation, which is actually the dispersion relation for the Rayleigh equation $D[\alpha,\omega]=0$. This condition forms singularities as shown in Figure 2.

To get the Green's function, we should evaluate two integrals of (10). The first inverse Fourier transform from frequency domain into time domain can be done by adding all the residues of singularities on the frequency domain. These singularities come from the dispersion relation, as we mentioned just before.[3] Then the integral can be evaluated as follows.

---

[3] Actually, there are other singularities. It forms a branch cut in ω plane. However, this kind of singularities usually forms only stable modes, which are not important to study the asymptotic stability as $t\to\infty$.

$$\hat{G}(\alpha,y,t)=\frac{1}{2\pi}\times -2\pi i\,\mathrm{Res}(\omega_1)=-i\,\mathrm{Res}(\omega_1)=-i\,e^{-i\omega_1 t}\left[\frac{H(y,0)}{\partial W/\partial\omega}\right]_{\omega=\omega_1(\alpha)}$$
$$=-\frac{e^{-i\omega_1 t}}{\alpha(U(0)-\omega_1/\alpha)}\left[\frac{\eta_{\mathrm{eigen}}(y;\alpha,\omega)\,\eta_{\mathrm{eigen}}(0;\alpha,\omega)}{(\partial W/\partial\omega)}\right]_{\omega=\omega_1(\alpha)} \tag{19}$$

Here we only include the most unstable branch ω_1. Note that $H(y,0)$ is now defined on the singularity, where the Wronskian of two homogeneous solutions becomes 0, so $\eta_1=\eta_2=\eta_{eigen}$.

The second inverse Fourier transform can be evaluated by the method of steepest descent path. With this method, on each ray $\frac{x}{t}=\frac{d\omega_1}{d\alpha}(\alpha^*)$, it becomes

$$G(x,y,t)=\frac{1}{2\pi}\int\hat{G}\,e^{i\alpha x}d\alpha=-\frac{e^{\frac{i\pi}{4}}}{\sqrt{2\pi}}\times\frac{e^{i(\alpha^* x-\omega^* t)}}{\left[\left(\frac{\partial^2\omega_1}{\partial\alpha^2}\right)^*\cdot t\right]^{1/2}}\times\frac{iH^*(y,0)}{\left(\frac{\partial W}{\partial\omega}\right)^*} \tag{20}$$

This solution represents the impulse response of the flow on specific ray $\frac{x}{t}=\frac{d\omega_1}{d\alpha}(\alpha^*)$ for large time. Note that the superposed response of all modes is collapsed into one mode, which is corresponding to α^* and $\omega_1(\alpha^*)$. If this particular mode is unstable, then the flow shows a growing oscillatory behavior on the ray.

To find out whether the flow is absolutely unstable or absolutely stable, we should check the point $x=0$, that is, the ray $x/t=0$. On this ray, $\alpha_0=\alpha^*$ and $\omega_0=\omega_1(\alpha_0)$ satsify the following condition.

$$\frac{d\omega_1}{d\alpha}(\alpha_0)=0,\ \text{and}\ \omega_0=\omega_1(\alpha_0).^4 \tag{21}$$

We call this mode (ω_0, α_0) as the absolute mode of the flow, and correspondingly, we call α_0 as absolute wave number and ω_0 as absolute frequency. So, if this absolute mode has positive

[4] This mode has zero group velocity. So, we may think that for a fixed point, the long-term response will be dependent on the mode with zero group velocity, because all other modes will be swept out from the point eventually.

imaginary part $\omega_{0,i}$ of ω_0, the flow is absolutely unstable. If not, the flow is convectively unstable or stable.

II.1.4 Temporal verses Spatial Analysis (Revisited)

We return to the discussion about the validity of spatial analysis again. As we mentioned earlier, spatial analysis can be justified only when temporal analysis can reconstruct the result of spatial analysis. It can be restated in a mathematical fashion. If the integration paths, F_α and L_ω, for temporal analysis can be transformed into the integration paths corresponding to spatial analysis without crossing singularities, the two sets of integration paths give the same result, so two methods of analysis are considered equivalent. In such a case, spatial analysis is justified, and can be physically meaningful.

In other words, we may describe the method as follows. See Figure 3. Originally, the location of L_ω for temporal analysis is determined by the causality condition, so it is placed over all the singularities in ω plane. L_ω for spatial analysis should be on the real axis, so we should move it down. When we move down L_ω, it will eventually hit the upper most curve of singularities, $\omega_1(F_\alpha)$. However, we can also deform the path F_α, as far as the two asymptotic end points at the infinity remain at the same limit position. The curve $\omega_1(F_\alpha)$ moves down due to the change of F_α, so we can further lower L_ω. We repeat this process until F_α is finally caught by the two curves corresponding L_ω. When this pinching occurs, we cannot lower L_ω any more. If we can lower L_ω up to real ω axis before this pinching occurs, the spatial analysis result is acceptable, because it can be recovered by the temporal analysis result by a proper path deformation. If not, the spatial analysis for the flow is physically meaningless.

Actually, the pinching point corresponds to absolute wave number and absolute frequency. This implies that we may rewrite the condition as follows: If the flow is absolutely unstable, spatial analysis is physically meaningless. Only for convectively unstable media, it has its physical validity.

II.1.5 Cusp Map Method

To find out whether a flow is absolutely unstable or not, we must compute the actual absolute mode frequency and the growth rate for a particular flow. The cusp map method is a simple method to achieve this task.

We must find out the set of α and ω that satisfies the absolute mode frequency selection criterion (21), which is copied here.

$$\frac{\partial \omega}{\partial \alpha} = 0 \text{ at } \omega = \omega_0, \alpha = \alpha_0.$$

This condition can be rewritten for $\omega = \omega_r + i\omega_i$ and $\alpha = \alpha_r + i\alpha_i$. We set α_i as a constant, then we have

$$\frac{\partial \omega_r}{\partial \alpha_r} = \frac{\partial \omega_i}{\partial \alpha_r} = 0. \tag{22}$$

This condition implies that both derivatives of ω_r and ω_i vanishes at the point, that is, it forms a cusp point for the curve of $\omega(\alpha_r + i\alpha_i)$ for a constant value of α_i in the complex ω plane. The occurrence of a cusp point at the location of absolute frequency is also shown in Figure 3.

The occurrence of a cusp point at the absolute frequency can be used as a criterion to find out the absolute frequency for a particular flow. For each constant α_i, we compute the values of $\omega(\alpha)$ for different values of α_r and plot them on the complex ω plane. By adjusting the range of α_r and α_i, we can find a cusp point on ω plane as shown in Figure 4. This cusp point is corresponding to ω_0, which is the complex absolute mode frequency. We can successively improve the resolution by repeating the process for smaller regions in the complex α plane. In the following sections, we use this method to find out absolute frequency and growth rate for a particular mean velocity profile.

Mathematically more rigorous description of the method may be found in [21, 22].

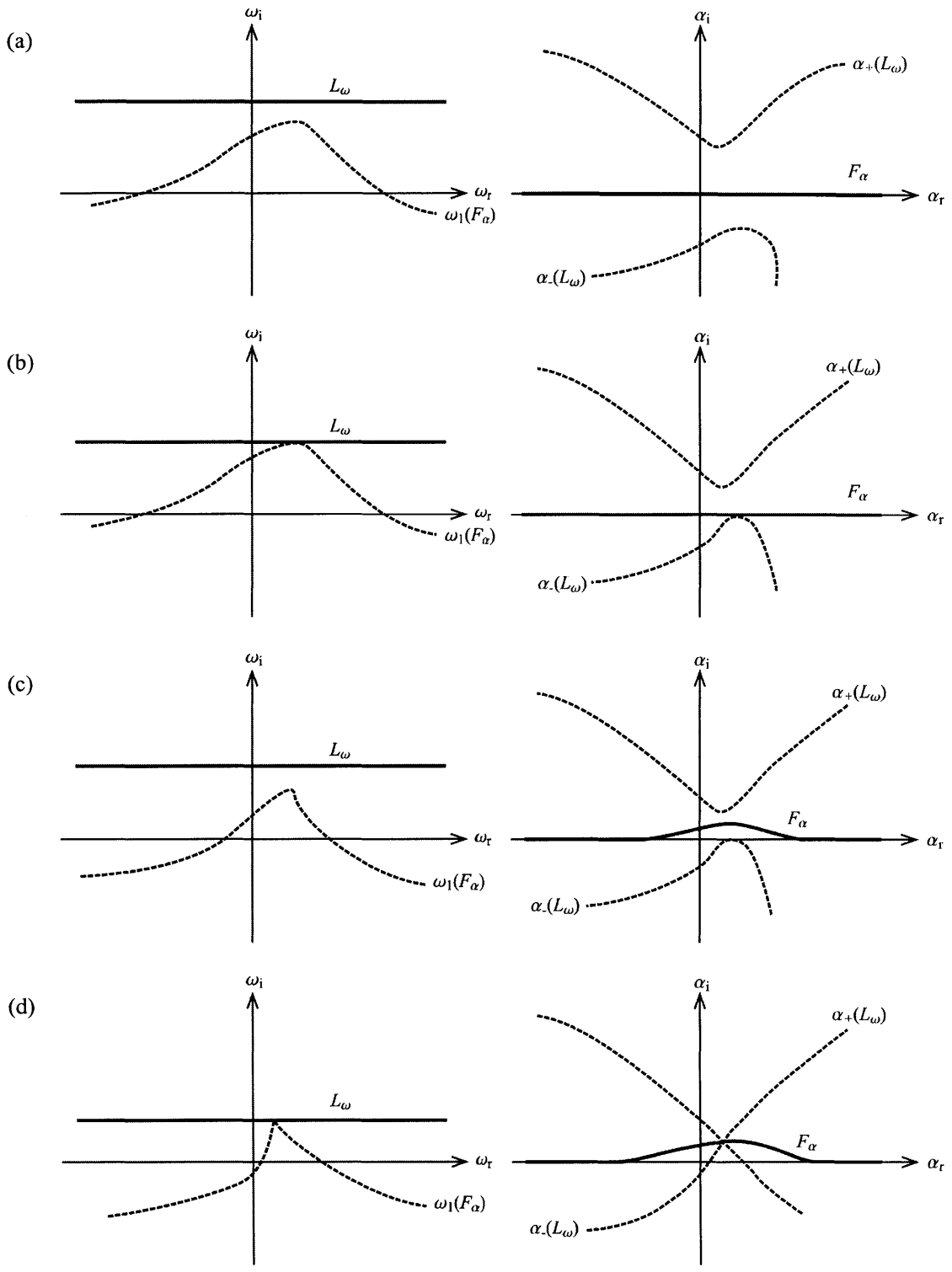

Figure 3 Illustrative sketch of successive path deformation. (a) shows the location of two integration paths for temporal analysis. First, L_ω is lowered to the limit (b). Then, F_α is moved to let L_ω be lowered further (c). This process can be repeated until pinching occurs (d). At this stage, no more deformation is possible.

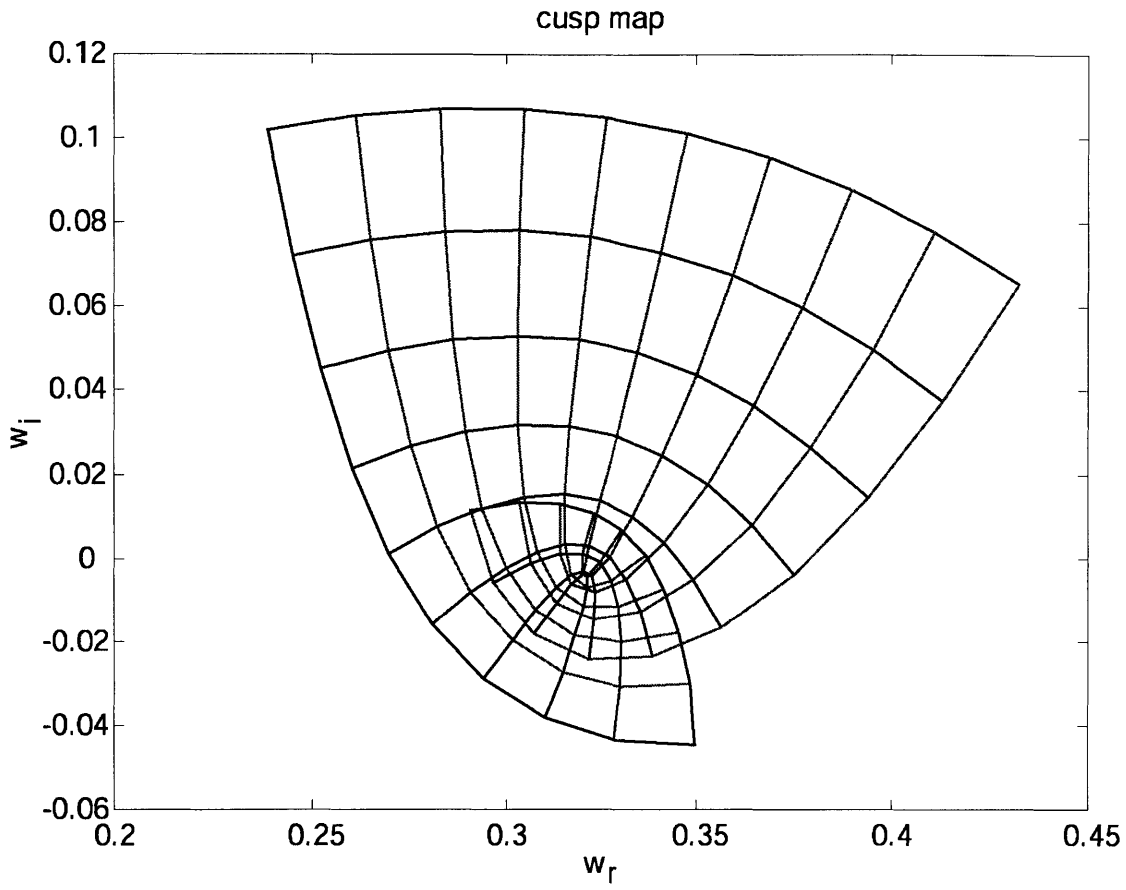

Figure 4 Application of the cusp map procedure. The map shows a cusp point near $\omega_0 \approx 0.325 - 0.005i$.

II.2 Absolute Modes for Separating Flows

In Section II.1, we described basic mathematical formulation of local stability analysis. There, the concepts of absolute and convective instabilities were introduced mathematically and physically. Especially, we mentioned that only absolutely unstable flows can show self-sustained resonance. We also showed that the dynamics of the shear flow is given by (20). It is very similar to that of a second-order oscillator with the absolute mode frequency ω_0 and the corresponding wave number α_0, which can be determined by (21). Also, we have described a practical method for calculating the absolute mode frequency ω_0.

In this section, the properties of the absolute mode are discussed in the context of a separating shear flow downstream of a backward-facing step. The complex frequency of the absolute mode, determined by (21), is evaluated using the cusp-map method [21, 22]. The following velocity profile is used to model a separating flow downstream a backward facing step;

$$U(y)=\frac{\beta-1}{2}+\frac{\beta+1}{2}\tanh\left(\frac{y}{\delta}\right)-\beta\tanh\left(\frac{y-a}{\delta_w}\right)-\tanh\left(\frac{y-b}{\delta_w}\right) \qquad (-a\le y\le b) \qquad (23)$$

where β is the ratio of backflow to the forward flow, δ defines the shear layer thickness, and δ_w is the boundary layer thickness at the wall. The last two terms are added to mimic the impact of the non-slip boundary condition. When δ and δ_w are reasonably small, the profile approximates the mean velocity distribution of step flows reasonably well. Figure 5 shows the mean velocity profile given by (23) for selected values of the parameters. We assume. These values are chosen to simulate the case with expansion ratio 2. We note that realistic values of β vary from 0.3 to 0.4 for the mean velocity profile in a backward-facing step flow at high Reynolds number.[5] We also note that in a typical recirculating flow, both the shear layer thickness and the backflow changes as we move downstream of the step. The profile given by (23), however, is intended to model the velocity distribution at a particular section, using the original assumption that the flow is parallel.

The absolute mode frequencies supported by these velocity profiles were calculated for various values of δ and β, and the results are depicted in Figure 6. Because the velocity profile

[5] See, for example, [14, 17, 23, 24].

given in (23) gives different flow rate for different parameters, we need to normalize the result. The Strouhal number is often based on the mean upstream velocity, U_0, we normalize the value of ω_0 as ω_0 / U_0, where $U_0 = \int_{y=-1}^{1} U(y)\,dy$.[6] Results show that for a fixed value of δ, the growth rate of the unstable mode switches from being convectively unstable to absolutely unstable as the backflow increases. Moreover, the growth rate of the absolutely unstable mode increases with increasing β. Similar observation can be made for δ; for a fixed backflow, decreasing δ can lead to an absolutely unstable flow, with further drop in δ causing an increase in the absolute mode growth rate. We also note that the mode frequency, $\omega_{0,r}$, is not strongly dependent on β, especially for larger values of δ, i.e. changes in the backflow, which is observed within the recirculation zone of a step flow, does not impact the frequency of the absolutely unstable mode significantly; they impact, however, the growth rate and hence absolute modes are more likely to originate at the section with strongest backflow. Because the shear layer thickness increases downstream of the step, reaching almost at the same order as the step height in the middle of the recirculation zone, we focus on the case with $\delta \cong 0.4$. This case corresponds to a shear layer thickness of almost unity, i.e. on the order of magnitude of the step height. As shown in Figure 6, $\omega_{0,r} \cong 0.6$ at $\delta \cong 0.4$, and the corresponding frequency of the absolute mode scales to $\mathrm{St} = \omega_{0,r} / 2\pi \cong 0.1$ for a range of β. This may explain the observation that strong fluctuations in backward-facing step flows occurs roughly near $\mathrm{St} = \dfrac{f\,h}{U_0} \cong 0.1$, where h is the step height and U_0 is the upstream mean velocity of the flow.

Using these results, we can classify the stability characteristics of the mean velocity profiles at each section of backward-facing step flows (see Figure 7). The objective of this classification is to determine the most likely origin of the most-unstable absolute mode within the recirculation zone, and its overall impact on the flow. At locations near the step, the shear layer is very thin, and the backflow is weak, and hence, according to Figure 6, the flow is absolutely stable. Near the middle of the recirculation zone, the mean velocity profile shows strong back flow, and the shear layer thickness is comparable to the step height; and hence the flow may become

[6] Because $U(y)$ is already a nondimensional velocity profile, this does not violate the dimension matching principle.

absolutely unstable at a frequency near $St \cong 0.1$. Note that, from previous observations, the frequency is only weakly dependent on the backflow and thus the absolute instability will be supported at the section of maximum backflow. Towards the end of the recirculation zone, the shear layer thickness remains almost the same, because the flow is bounded by the upper and lower walls, while the backflow diminishes. Figure 6 shows that under these conditions, the frequency should remain the same, $St \cong 0.1$, while the flow becomes absolutely stable.

The following global picture of a separating shear layer instability, which is supported by strong backflow, emerges form the previous analysis. Self-sustained oscillation occurring in the middle of the recirculation zone, where the backflow is strongest, propagates upstream and downstream. The frequency of these oscillations is determined by the thickness of the shear layer at the point of the initiation, i.e. the middle of the recirculation zone. The evidence from experimental measurements and numerical simulations is that the thickness of the shear zone around the middle of the recirculation zone is of the order of magnitude of the step height. Once these oscillations reach an absolutely stable but convectively unstable region, the flow becomes convectively unstable, i.e. oscillation at the local convective mode with the most unstable frequency may be excited. While the growth of these oscillations, associated with the convective mode at the step, are swept by convection downstream, those due to an absolutely unstable mode in the middle of the recirculation zone persist. With a sufficiently large region of absolutely instability, corresponding to a zone with sufficient backflow, the flow shows a behavior of an unstable oscillator. In this sense, the absolutely unstable section acts as a wave maker for the whole flow, and the frequency of the oscillation is given by $St \cong 0.1$. It should be noted that the experimentally observed frequency 96 Hz in [13] corresponds to $St = 0.092$ and is within this range.

To support the conclusions of this analysis regarding the source of sustained oscillations in the separating shear layer, a numerically obtained mean velocity profile for a backward-facing step flow is examined. Simulations are obtained using a two dimensional vortex code, running at Reynolds number of 5000.[7] These simulations have shown two vortex shedding phenomena, one large eddy which forms in the middle of the recirculation zone, and another smaller eddy that forms close to the step within a fraction of the period of large eddy formations. These results

[7] Re is based on the step height and the upstream average flow speed.

were obtained without forcing, except for the perturbations introduced due to numerical truncation errors and the statistical noise associated with the random walk simulation of diffusion. Similar results are obtained using finer numerical discretization indicating that it is unlikely that "numerical forcing" is the origin of the unsteadiness. Moreover similar unsteadiness has been observed in other simulations of the same flow, using different numerical methods both in two and three dimensional flows [23-26]. The persistence of these unsteady features and the fact they are observed numerically and experimentally support the claim that they arise due to some intrinsic dynamics, which may have its origin in the instability characteristics of the flow.

Results of the linear stability analysis of the numerical data are shown in Figure 8. For the purpose of the analysis, the mean velocity profiles corresponding to the average streamlines shown in Figure 5 have been calculated at about 30 sections across the recirculation zone and fitted to a mean velocity profile similar to (23), and the cusp-map method was used to analyze these profiles and determine the frequency of the absolute mode. As shown in Figure 8, the local absolute mode frequency shows a maximum growth rate near the point $x/H = 1.5$, i.e. close to the middle of the recirculation zone, as predicted before, and the frequency of the mode shows weak dependence on the location in the neighborhood of that point. In the numerical simulation, the formation of a large vortex occurs actively at the middle of the recirculation zone, which corresponds to the location of the maximum growth rate point. The corresponding Strouhal number is $St = 0.083$, also within the range of $St \cong 0.1$. This value is verified using the numerical simulation results. The locally dominant mode frequency decreases downstream, as shown in several experiments, and reaches a plateau towards the end of the reciruclation zone at values of $St \cong 0.08$.

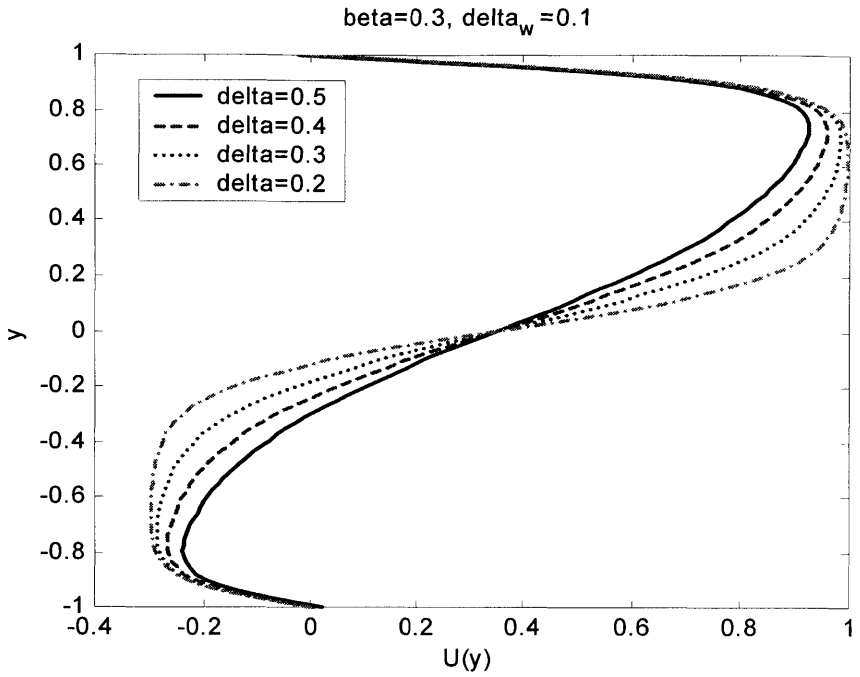

Figure 5 Velocity profile given by (16) for different flow parameters.

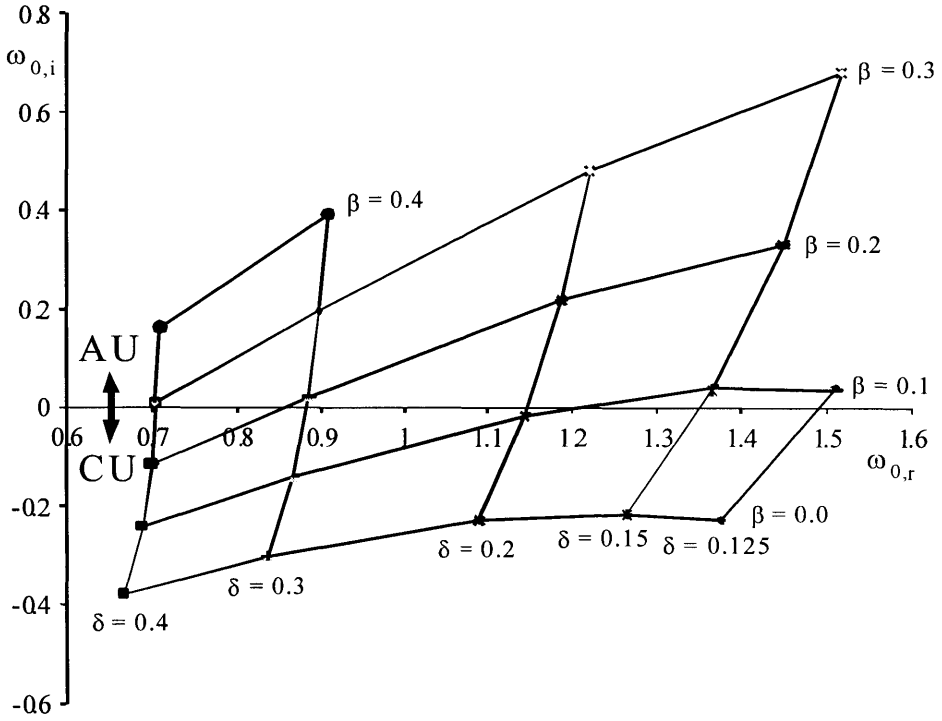

Figure 6 Absolute mode frequencies for the family of velocity profiles shown in equation (1), for different values of the shear layer thickness δ and the backflow β.

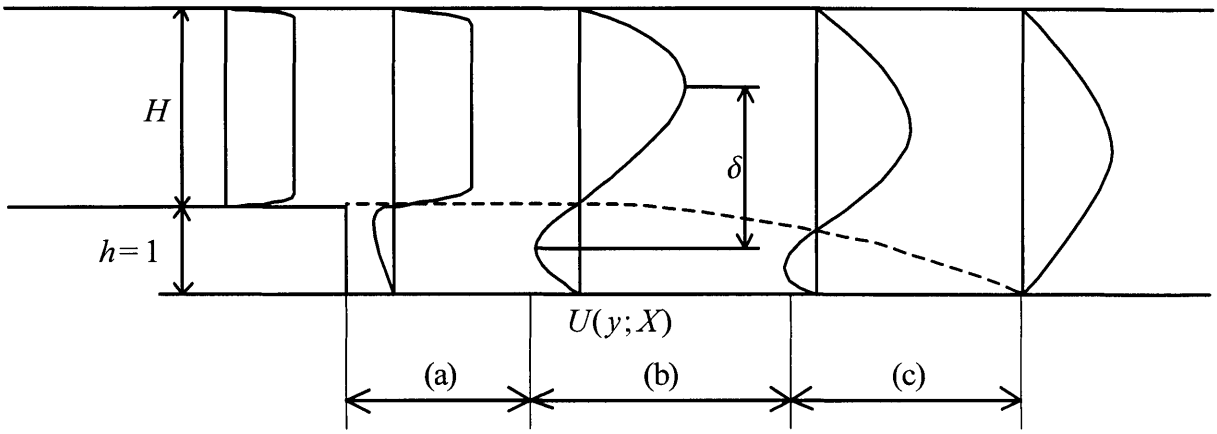

Figure 7 Schematic illustration of different regions in recirculation zone:

(a) $\delta < O(1)$ with weak backflow: local absolute frequency $\omega_0 \sim 1/\delta$ and locally absolutely stable.

(b) $\delta = O(1)$ with weak backflow: local absolute frequency St ~ 0.1 and locally absolutely unstable.

(c) $\delta = O(1)$ with weak backflow: local absolute frequency St ~ 0.1 and locally absolutely stable.

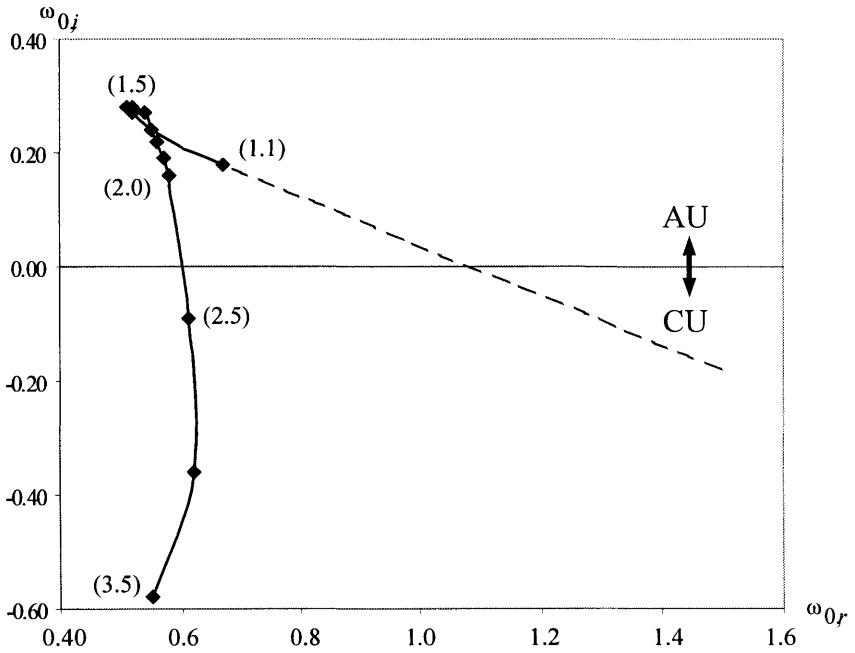

Figure 8 Local absolute mode frequencies for the mean velocity profiles obtained from the numerical simulation of a backward facing step flow at Re=5000. In the parenthesis next to the data point, the normalized location of the section (x/H) is shown. Note that x/H=0 at the step.

II.3 Shear Layer Instability in Reacting Flows

Flows we have examined so far are isothermal, i.e. with uniform density. When combustion occurs, it changes the shear layer characteristics by introducing a temperature gradient, which in turn gives rise to a density gradient, and affecting the mean velocity profile. To see the effect of the temperature gradient on the stability characteristics, we use the inviscid compressible Rayleigh equation, which is given in [21, 27]. At the subsonic limit:

$$\frac{d}{dy}\left[\frac{(U(y)-c)-U'(y)}{\Theta(y)}\frac{d\tilde{v}}{dy}\right]=\frac{\alpha^2}{\Theta(y)}(U(y)-c)\tilde{v} \tag{24}$$

where Θ is the normalized mean temperature profile.

Now, we assume the following mean temperature field.

$$\Theta(y)=\frac{1+\gamma}{2}+\frac{1-\gamma}{2}\tanh\left(\frac{y}{\delta}\right), \tag{25}$$

where γ is the temperature ratio, which represents a premixed combustion in shear layer. We assume that the thermal boundary layer thickness is of the same order of magnitude as the shear layer thickness. This choice mimics the case where the Prandtl number is near unity.

Keeping a, b and δ_w same as before, the absolute modes for various values of γ, β and δ is computed. The result is shown in Figure 9, 10 and 11. For frequency and growth rate, the values obtained are divided by $\int_{y=a}^{b}\frac{U(y)}{\Theta(y)}dy$ for normalization before plotting. As γ increases, the flow becomes "less absolutely unstable", i.e. combustion stabilizes the flow by inducing a temperature gradient across the shear zone. Moreover, the flow may switch to a convectively unstable mode at some critical value of γ. The absolute mode frequency $\omega_{0,r}$ shows weak dependency on the backflow parameter β as in the isothermal case. Previous studies of shear layer stability have indeed shown that the important parameters here is the density ratio, and simulations have been used to explain these effects [28]. In particular, the phase speed of the most unstable mode and the convective speed of eddies strongly depends on the density ratio, which suggests that the absolute mode characteristics determined in terms of the group velocity should also show a strong dependency on the density ratio.

It should be noted that the average locations of shear layer and the flame zone may not coincide. Instead a finite offset between the centerline of both may exit, supported by the fact

that the flame starts at the separation point and ends at the upper wall, as shown in [14], while the shear layer starts at the same point but moves downwards towards the lower wall. This offset tends to become larger at higher equivalence ratio as the burning velocity of the premixed flame increase forcing the flame to move towards the outer edges of the large eddies instead of burning closer to their centers. To study the impact of the offset, we replace y with $y-\Delta$ in (25). The impact of the offset is shown in Figure 12. At small temperature ratios, i.e. at conditions of lean combustion, the offset is expected to be very small. In any case, results show that, under these conditions, the offset has almost no impact of the mode frequency and growth rate. At higher temperature ratio, as the equivalence ratio moves towards stoichiometry, the offset is expected to be finite and results show that its impact becomes important: at small offset, the flow is convectively unstable, but at larger values, it becomes absolutely unstable. This is clearly shown in Figure 12 where the curve corresponding to $\omega_{0,i}/\omega_{0,r}=0$ delineates the border between the absolutely unstable and the convectively unstable regimes. It should be added here that the offset and the temperature ratio are not totally independent since, for the same fuel, they both depend on the equivalence ratio; in fact, it can be stated that they both increase as the fuel concentration in the mixture approaches stoichiometry. This is shown schematically by the thick arrow in Figure 12, where a line is drawn to connect qualitatively the possible trajectory of states of the flow as the equivalence ratio is increased from lean conditions to chemically stoichiometric conditions.

The second effect of combustion, that is changing the mean velocity profile due to the exothermic effects, is harder to identify. In general, there is a tendency for combustion to reduce the reattachment length and increase the velocity within the recirculation zone, with an associated rise in backflow. The investigation of these effects is a future task.

In summary, the results of linear stability analysis of shear flow show the following characteristics:

1. The shear layer instability can produce self-sustained oscillations. This is due to the presence of absolutely unstable modes which arise when the mean velocity profile shows a strong back-flow at sections where the shear layer thickness is relatively small.
2. The absolutely unstable modes in a backward-facing step flow show an oscillation frequency close to $St \cong 0.1$. The apparent universality of this value is explained by its dependence on the thickness of the layer, about a step height, and the value of backflow. Also, the predicted frequency matches the experimental observation (of St = 0.092) in [13].
3. The "global" separating shear layer mode frequency is the same as the local most absolutely unstable mode, i.e. the absolutely unstable mode with the highest growth rate within the separation zone.
4. The impact of these modes is most pronounced at the middle of the recirculation zone, while closer to the step small scale shedding due to other, most likely convective modes, is observed.
5. Large temperature gradients across the shear layer force the flow to become more absolutely stable, and hence stability characteristics can be affected by combustion. Flows at higher equivalence ratio can become absolutely unstable due to the offset between the shear layer and the flame boundary.

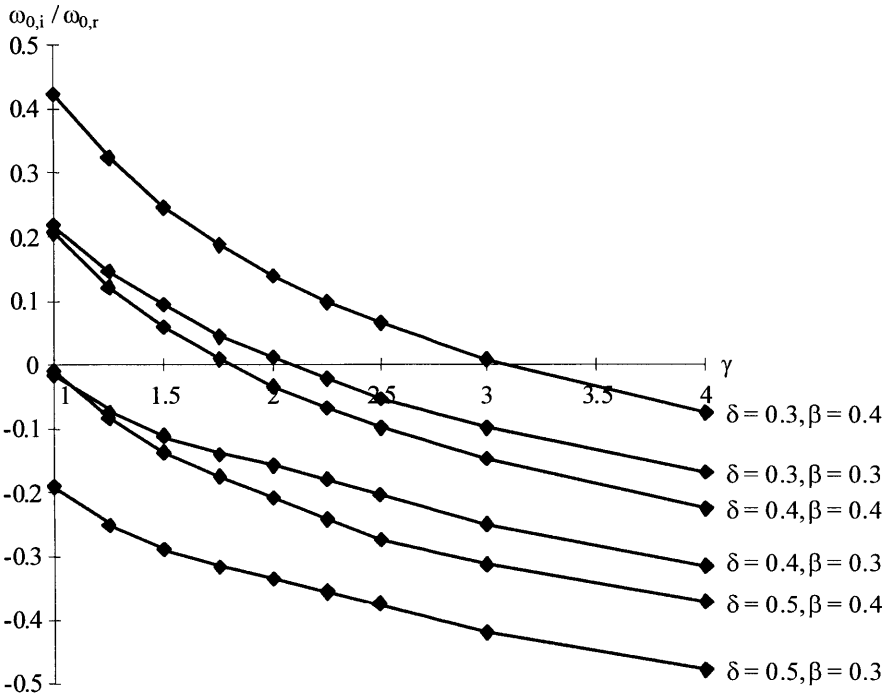

Figure 9 Relative growth rate $\omega_{0,i} / \omega_{0,r}$ of absolute mode for various values of γ, δ, and β.

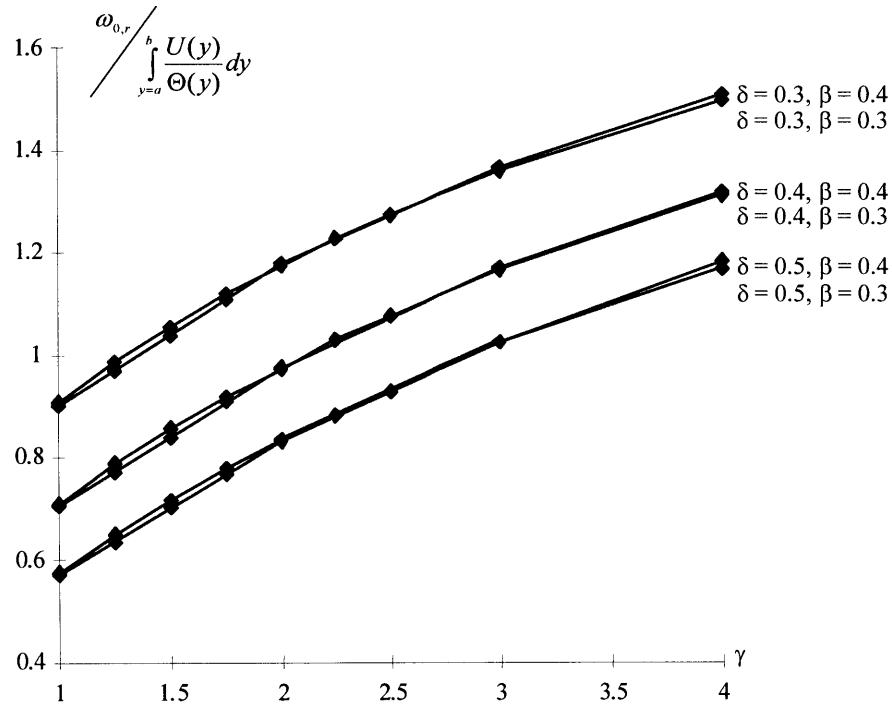

Figure 10 Normalized frequency of absolute mode for various values of γ, δ, and β.

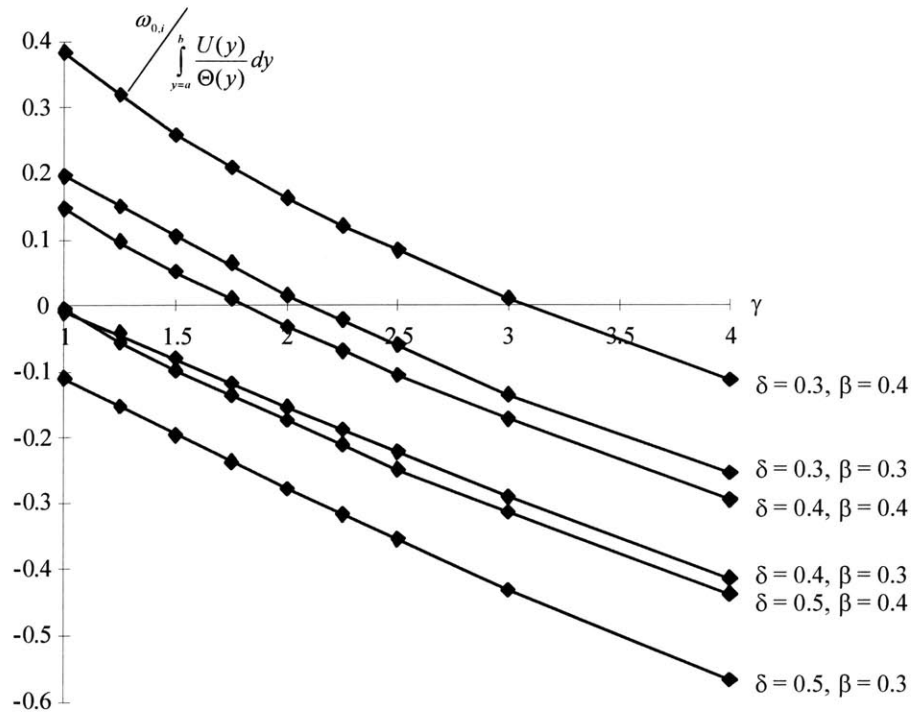

Figure 11 Normalized growth rate of absolute mode for various values of γ, δ, and β.

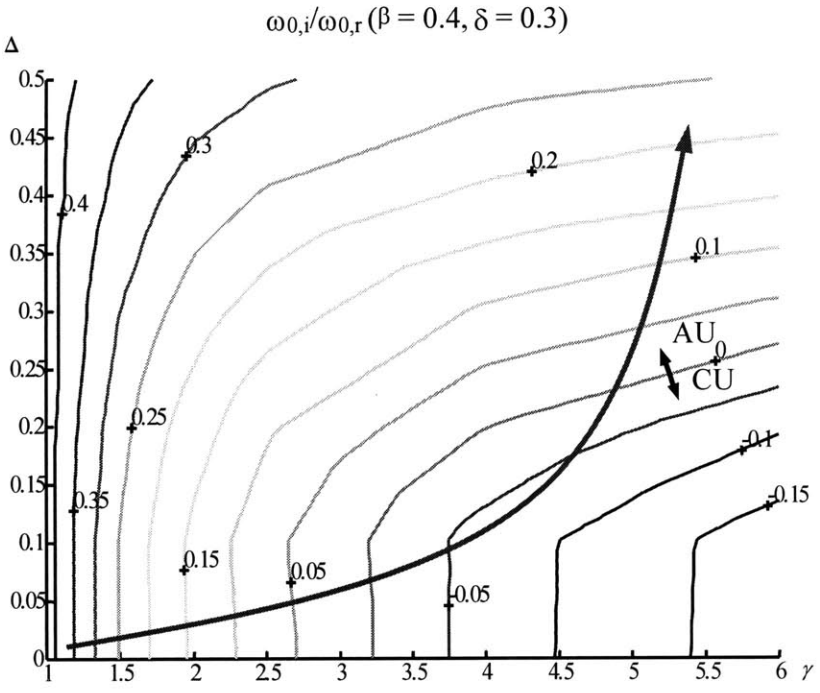

Figure 12 The impact of the temperature distribution on the properties of the absolute instability, shown in terms of the ratio of absolute growth rate to absolute frequency ($\omega_{0,i}/\omega_{0,r}$) for various values of temperature ratio γ and offset Δ with $\delta = 0.3$ and $\beta = 0.4$. The thick arrowed line shows a possible path for increasing the equivalence ratio.

III Reduced Order Modeling with POD-Galerkin Procedure

In Chapter II, we discussed the dynamics of shear layers in the context of linear stability analysis, and showed that it can generate self-sustained oscillations under certain conditions. These discussions and other experimental observations [8-13] demonstrate that a more comprehensive model of thermoacoustic instability must encompass the three components: acoustics, heat release dynamics, and shear layer dynamics.

The analytical tool used in Chapter II to describe shear-layer instability is the linear stability theory. While the theory may be used to gain insight into stability characteristics of shear flow and their possible role in "post transition states", and help explain and generalize results from numerical simulations, a quantitative model of shear layers cannot easily be obtained from linear stability analysis. On the other hand, while detailed numerical simulations can be made quite accurate, the huge computational resources needed for detailed simulations makes them insufficient for control applications. What is more useful is a reduced-order model for shear layer dynamics, that is capable of utilizing the available numerical results or experimental measurements to construct a more complete quantitative model of the overall combustion dynamics.

In this chapter, we discuss a tool to construct a reduced order model, POD-Galerkin procedure, and use numerical results to obtain a reduced order model of the flow field in the presence of hydrodynamic instability. In Section III.1, we discuss POD (proper orthogonal decomposition) as a tool to generate an optimal set of basis functions. In Section III.2, Galerkin projection of NSE (Navier-Stokes equation) is described. Also, we address the difficulty of dealing with the extended domain of the numerical simulation, and show how to resolve this difficulty within the context of backward-facing step flows in Section III.3. Finally we apply the method to a backward-facing step flow, and examine whether the procedure can capture the coherent dynamics of this type of flows.

Before going into the actual description of the method, we define several mathematical notations:

$\mathcal{D}(\Omega) = C_0^\infty(\Omega)$, $\mathcal{V} = \left\{ u \in \{\mathcal{D}(\Omega)\}^2, \nabla \cdot u = 0 \right\}$,

H = the closure of $\mathcal{V}$ in $\{L^2(\Omega)\}^2$, V = the closure of $\mathcal{V}$ in $\{H_0^1(\Omega)\}^2$.

When $u, v \in H$,

$(u,v) = \int_\Omega u(x) \cdot v(x)\, dx$ $\qquad$ $|u(x)|_{L^2} = (u,u)^{1/2}$

When $u, v \in V$,

$((u,v)) = \sum_{1 \le i,j \le 2} \int_\Omega \frac{\partial u_i}{\partial x_j} \frac{\partial v_i}{\partial x_j} dx$ $\qquad$ $\|u(x)\| = ((u,u))^{1/2}$

Note that (u,v) is a norm in H, and so is $((u,v))$ in V. Both spaces are Hilbert spaces with corresponding norms.

III.1 Proper Orthogonal Decomposition (POD) Method

POD has been used as a tool to extract coherent structures from numerical data in turbulence research [29], and has also been introduced as a systematic and optimal way to derive reduced-order models more recently [30, 31, 32].

In POD, one uses numerical or experimental results to construct a space of optimal basis functions that describe the different modes of the flow. This set of basis functions or modes obtained by POD is optimal in the sense that any other choice of basis functions shows larger error in the L^2 norm. In this section, we describe briefly the method itself.

We start from the given set of N data $u_n(x)$ $(n=1, 2, \cdots, N)$, which is called the set of snapshots.[8] Our task is obtaining an optimal basis function to describe this set of data, that is:

$$\text{Maximize } J = \frac{1}{N}\sum_{j=1}^{N}(u_j,\Phi)^2 \text{ subject to } (\Phi,\Phi)=1. \tag{26}$$

The problem defined by (26) can be expressed as an equivalent eigenvalue problem. To see this, we define

$$\mathbf{K}\Phi = \frac{1}{N}\sum_{j=1}^{N}\int_{\Omega} u_j(x)\{u_j(x')\cdot\Phi(x')\}dx' \tag{27}$$

then

$$(\mathbf{K}\Phi,\Phi) = \frac{1}{N}\sum_{j=1}^{N}\int_{\Omega}\int_{\Omega}\{u_j(x)\cdot\Phi(x)\}\{u_j(x')\cdot\Phi(x')\}dx'dx = \frac{1}{N}\sum_{j=1}^{N}(u_j,\Phi)^2. \tag{28}$$

Using (28), (26) can be restated as follows.

$$\text{Maximize } J = (\mathbf{K}\Phi,\Phi) \text{ subject to } (\Phi,\Phi)=1. \tag{29}$$

We solve (29) using Lagrange multiplier technique, and it leads to

---

[8] The term 'snapshot' usually implies that the data are obtained in a single run of experiment or simulation. Different snapshots are collected at different time steps. Because it is based only on a single run, the data is statistically acceptable, only when the system is ergodic. From now on, we assume the system is ergodic, and don't discuss this technical issue here any more.

$$(\mathbf{K}\Phi, \Phi') = \lambda(\Phi, \Phi') \tag{30}$$

which is equivalent to

$$\mathbf{K}\Phi = \lambda\Phi. \tag{31}$$

Now, it is clear that (26) is equivalent to an eigenvalue problem for the operator **K**. We further simplify (31) by assuming that $\Phi = \sum_{j=1}^{N} w_j u_j(x)$. Then, we have an eigenvalue problem for covariance matrix C:

$$CW = \lambda W$$

where

$$C_{ij} = \frac{1}{N}\int_{\Omega} u_i(x)u_j(x)dx \text{ and } W = [w_1 \; w_2 \; \cdots \; w_N]^{\mathrm{T}}. \tag{32}$$

We can repeat this process for another basis function. Eventually, each eigenvector from (32) gives one basis function, and the basis functions are orthogonal to each other. The eigenvalue corresponding to each basis function is equal to the average kinetic energy of that mode, i.e. $\lambda = \frac{(\mathbf{K}\Phi, \Phi)}{(\Phi, \Phi)} = \frac{1}{N}\sum_{j=1}^{N}(u_j, \Phi)^2$ when $(\Phi, \Phi) = 1$. It is customary that POD basis functions are ordered by the size of the corresponding eigenvalues, from the largest one to the smallest one. From now on, we also use this ordering scheme.

III.2 Galerkin Projection of Navier-Stokes Equation (NSE)

Galerkin projection based on $\Phi_1(x), \Phi_2(x), \cdots, \Phi_m(x)$ is the projection of the original PDE onto $\text{span}[\Phi_1(x), \Phi_2(x), \cdots, \Phi_m(x)]$. In this procedure, all the terms in the orthogonal space are considered as small and are neglected. This projection results in a nonlinear dynamical system, whose dimension is m, which is manageable for control purposes, if m is reasonably small. In the following, we briefly describe the procedure in the context of NSE without too much mathematical technicality.

When Ω is a bounded open set in R^2, whose boundary is denoted as Γ, the NSE is given by the following set of equations.

$$\tilde{u}_t + \tilde{u}\cdot\nabla\tilde{u} = \nu\Delta\tilde{u} - \nabla p,\ \nabla\cdot\tilde{u} = 0$$
$$\tilde{u}(x,0) = \tilde{u}_0(x),\ \ \tilde{u}(x,t) = \phi(x)\ \text{ on }\ x\in\Gamma \tag{33}$$

To incorporate the possibly inhomogeneous boundary condition on Γ, we subtract a divergence-free vector field $U(x)$ whose value is $\phi(x)$ on Γ from $\tilde{u}(x,t)$. The construction of $U(x)$ can be done by using Hopf's technique [33], but the common practice is simply setting the time-averaged velocity profile as $U(x)$.[9] We denote the resulting velocity field as $u(x,t)$, then

$$u_t + u\cdot\nabla u + u\cdot\nabla U + U\cdot\nabla u + U\cdot\nabla U - \nu\Delta u - \nu\Delta U - \nabla p = 0,\ \nabla\cdot u = 0$$
$$u(x,0) = u_0(x) = \tilde{u}_0(x) - U(x),\ u(x,t) = 0\ \text{ on }\ x\in\Gamma \tag{34}$$

We project the equations onto $\text{span}[\Phi_1(x),\Phi_2(x),\cdots,\Phi_m(x)]$.

$$\text{For all } 1\le j\le m,$$
$$(u_t + u\cdot\nabla u + u\cdot\nabla U + U\cdot\nabla u + U\cdot\nabla U - \nu\Delta u - \nu\Delta U - \nabla p,\Phi_j) = 0 \tag{35}$$
$$(u(x,0),\Phi_j) = (u_0,\Phi_j)$$

Using Green's theorem, we obtain

$$(\nabla p,\Phi_j) = \int_\Omega \nabla p\cdot\Phi_j\,dx = -\int_\Omega p(\nabla\cdot\Phi_j)\,dx + \int_\Gamma p(\Phi_j\cdot\hat{n})\,dx = \int_\Gamma p(\Phi_j\cdot\hat{n})\,dx$$
$$(\Delta v,\Phi_j) = \int_\Omega \Delta v\cdot\Phi_j\,dx = -((v,\Phi_j)) + \int_\Gamma(\nabla v\cdot\Phi_j)\cdot\hat{n}\,dx \tag{36}$$

where $\hat{n}$ is the outward-normal unit vector on Γ.

The boundary terms vanish when $u(x,t)$ satisfies homogeneous Dirichlet boundary condition and so does $\Phi_j(x)$. Using (36) with this particular boundary condition, we substitute $u(x,t) = \sum_{i=1}^{m}\alpha_i(t)\Phi_i(x)$ into (35), and get

$$\dot{\alpha}_i M_{ij} = A_{ij}\alpha_i + \alpha_i B_{ijk}\alpha_k + D_j,\ \ \alpha_i(0)M_{ij} = (u_0,\Phi_j)$$
$$\text{where}$$
$$M_{ij} = (\Phi_i,\Phi_j),\ \ A_{ij} = (U\cdot\nabla\Phi_i + \Phi_i\cdot\nabla U,\Phi_j) - \nu((\Phi_i,\Phi_j)),$$
$$B_{ijk} = (\Phi_i\cdot\nabla\Phi_k,\Phi_j),\ \ D_j = (U\cdot\nabla U,\Phi_j) - \nu((U,\Phi_j)). \tag{37}$$

---

[9] Hopf's technique is preferred by mathematicians, because we can bound the size of the product terms of $U(x)$ and $u(x,t)$ by a constant as small as we want by this method. When these product terms are small, we can extend the theory of NSE for homogeneous Dirichlet BC, which is relatively well established, to the case with inhomogeneous BC.

If the basis functions are orthogonal to one another, $M_{ij} = \delta_{ij}$; this is automatically true if we obtain the basis functions via POD method. Also, POD basis functions are optimal in the sense that they maximize the amount of projection of the given data sets. In this sense, the set of POD basis functions can be considered as one of the best choices of basis functions for Galerkin projection method.

However, we should note that there is no rigorous guarantee that this reduced dynamical system would represent the dynamics of the original PDE within reasonable accuracy. It is very easy to construct an example where the reduced dynamical system obtained by Galerkin projection method is even qualitatively different from the original system [34]. The convergence theorem for Galerkin projection method [35] does not help us evade from this difficulty, because the set of POD basis functions can never be complete in V.[10] In this context, the accuracy of the reduced dynamical system must be assessed a posteriori by comparing the reduced order simulation results with detailed – presumably exact – simulation results.

III.3 Extended Domain of Simulation and Modified POD–Galerkin Procedure

The procedure described in Sections III.1 and III.2 presents a basic framework for constructing a reduced order model, which may be adopted directly to modeling of a backward-facing step flow, we must note a possible problem. The problem necessitates the modification of the method.

Because of its spatially elliptic characteristics, NSE must have appropriate boundary conditions on the entire Γ, including the exit, to be well-posed. On the other hand, the exit boundary condition is uncertain for most cases, and we specify it rather arbitrarily. To avoid the possible adversary effect of this arbitrarily forced boundary condition at the exit, it is a usual practice to have the exit boundary as far as possible from the domain of interest. The simulation of a backward-facing step flow is not an exception. We are interested in the velocity field near the recirculation zone, which extends itself up to 5 or 6 step heights downstream from the step. However, in numerical simulation of a backward-facing step flow, we usually use a domain

[10] Even with very large number of modes, POD basis functions will only be able to capture the linear subspace of V, where the ergodic global attractor lies.

including more than 20 step heights downstream from the step to avoid the effect of the exit boundary condition.

Although the inclusion of the extended domain is a usual practice, it may harm the efficiency of the POD-Galerkin procedure badly. The basis functions obtained by maximizing L^2 norm in the whole domain may be optimized on the extended domain, whose area is much larger than that of our domain of interest. In backward-facing step flows, the situation can become worse by the small amplitude of oscillation near the step, where eddies are still at the initiation stage. As a result of these two effects, the optimization of POD basis functions ends up with optimization for the extended domain. This will result in poor reconstruction of the velocity profile in the recirculation zone, and it may harm the overall accuracy of reduced order model simulation, because the dynamics of backward-facing step flows seem to be dominated by the absolutely unstable region in the recirculation zone as described in Chapter II.

To resolve the problem, subdomain formulation has been proposed [30]. Although the detailed simulation is performed over the entire domain, including the extended downstream, POD basis functions are obtained by using the data over a smaller subdomain. In the context of backward-facing step flows, we compute L^2 norm only over a smaller subset of the whole domain, covering the recirculation zone. With this subdomain approach, we can limit the optimization process to the domain of interest.

However, this approach causes another problem. In III.2, we argued that the boundary contribution in (36) vanishes because of the boundary condition, and obtained (37). If we restrict the domain to a subdomain of the original simulation domain, we do not know what is the actual boundary condition imposed on this subdomain, and cannot eliminate the boundary contribution in (36). This unknown boundary condition will lead to an additional term that should be modeled in another way. Although we may find a reasonable model for these boundary contribution terms for special cases such as a wall layer model [30], the method of modeling these terms is not obvious in general. In the current situation, it is very hard to model these terms in an appropriate way.

Because subdomain formulation does not seem to be very promising, we propose another method to avoid the undesirable effect of extended domain and the issue of boundary terms at the same time. In this new approach, we use a weight function to emphasize a particular region. We

simply change the original maximization problem (26) into a new maximization problem of weighted projection, that is,

$$\text{Maximize } J = \frac{1}{N}\sum_{j=1}^{N}(u_j,\Phi)_W{}^2 , \tag{38}$$

where $(u,v)_W = \int_\Omega u(x)\cdot v(x)\,\tilde{w}(x)\,dx \ \ (\tilde{w}\ge 0)$.

We give more weight to the location of interest, and less weight to the rest of the domain. We may set $\tilde{w}(x)=0$ for some region to neglect the contribution of that region completely. We usually say that the region is masked when $\tilde{w}(x)=0$ for the region.

It is easy to check that (38) can be restated as an eigenvalue problem just as (26). We only need to modify the L^2 norm into the weighted norm, that is:

$$\tilde{\mathbf{K}}\Phi = \tilde{\lambda}\Phi \text{ where } \tilde{\mathbf{K}}\Phi = \frac{1}{N}\sum_{j=1}^{N}\int_\Omega u_j(x)\{u_j(x')\cdot\Phi(x')\}\tilde{w}(x)\,\tilde{w}(x')\,dx' . \tag{39}$$

Also, by assuming that $\Phi = \sum_{j=1}^{N} w_j u_j(x)$, we have an eigenvalue problem for a modified covariance matrix $\tilde{C}$:

$$\tilde{C}W = \tilde{\lambda}W$$

where

$$\tilde{C}_{ij} = \frac{1}{N}\int_\Omega u_i\,u_j\,\tilde{w}^2\,dx \text{ and } W = [w_1\ w_2\ \cdots\ w_N]^{\mathrm{T}} . \tag{40}$$

Once we obtain the new basis functions, we need to construct the reduced order model based on these basis functions. We may proceed as in Section III.2. The boundary terms still vanish, because homogeneous Dirichlet boundary condition is imposed on the original boundary. However, two different issues arise. First, although these new basis functions are orthogonal to one another with respect to the weight function, they are not orthogonal to each other in usual L^2 norm. Therefore, when we project NSE on these new basis functions, M_{ij} in (37) is no longer δ_{ij}, and we should invert a matrix to obtain explicit equations for $\dot{\alpha}_i$. Second, to obtain the initial conditions $\alpha_i(0)$, we use $\alpha_i(0) = (u_0,\Phi_i)_{\sim}$. As the result, we have

$$\begin{aligned}&\dot{\alpha}_i M_{ij} = A_{ij}\alpha_i + \alpha_i B_{ijk}\alpha_k + D_j, \ \ \alpha_i(0) = (u_0,\Phi_j)_W \\ &\text{where } M_{ij},\ A_{ij},\ B_{ijk} \text{ and } D_j \text{ are the same as those given in (37).}\end{aligned} \tag{41}$$

This procedure may be extended hierarchically with multiple weight functions. Let $\widetilde{w}_k(x) \geq 0$ be the kth weight function, where $k = 1, 2, \cdots, K$, and let $\widetilde{n}_k$ be the number of modes that are computed with the spatial weight $\widetilde{w}_k$, and we assume that N snapshots, $u_1, u_2, \cdots, u_N$, are given. POD method can be modified as:

1. Set the set of basis functions as an empty set, i.e., $\Psi = \{\}$. Set $k = 1$.
2. Set $\widetilde{w} = \widetilde{w}_k$, and solve (40).
3. Take the first $\widetilde{n}_k$ eigenvectors, $W_1, \cdots, W_{\widetilde{n}_k}$, and compute the corresponding POD basis functions. Put these basis functions into Ψ.
4. If $k = K$, break the loop, and Ψ will be the set of basis functions. Otherwise, take the orthogonal part of $u_1, u_2, \cdots, u_N$ to the elements of Ψ, and set these as new data, $u_1, u_2, \cdots, u_N$. Set $k = k + 1$.
5. Repeat from 2.

Galerkin projection of NSE onto the basis functions obtained from this modified POD method is also straightforward. It leads to (37), except that the initial condition should be computed from the following nested procedure:

1. Set $k = 1$.
2. Set $\widetilde{w} = \widetilde{w}_k$, and obtain $\alpha_i(0) = (u_0, \Phi_i)_{\widetilde{}}$ for the basis functions corresponding to $\widetilde{w}_k$.
3. If $k = K$, break the loop. Otherwise, take the orthogonal part of u_0 to the all basis functions corresponding to $\widetilde{w}_j$, $1 \leq j \leq k$, and set it as u_0. Set $k = k + 1$.
4. Repeat from 2.

Note that this 'nested weighting procedure' provides a method of enhancing the quality of reduced order models without increasing the overall number of modes. We may redistribute the number of the basis functions with a particular weight to get a more accurate tracking capability from the reduced order model. In some cases, it may give an efficient model, whose accuracy is

comparable to the accuracy of the model with larger number of modes obtained from the standard POD method. We will see the advantage of this approach in the next section.

III.4 Application to a Backward-facing Step Flow

As mentioned before, the numerical data were obtained from the two-dimensional simulation of a separating flow downstream of a backward-facing step using a vortex method code. The code is an improved version of an original code, which has been described extensively in the literature and used for several simulations of similar flows [17, 36]. The difference between this new code and the original one is that the current code uses an FEM based VIC scheme to enhance the efficiency of computing the advection of vortex blobs.

The computation was performed for the geometry described in Figure 13, where the step height h is 1, and the uniform inlet velocity is given by U_0, with Re=3700. The flow is absolutely unstable, and shows unsteadiness without forcing as expected by the reasoning in Chapter II. In this section, we apply the procedure described in the previous sections to this set of data.

III.4.1 Construction of Reduced Order Models

To obtain basis functions, 500 snapshots, $\tilde{u}_1(x), \tilde{u}_2(x), \cdots, \tilde{u}_N(x)$ $(N = 500)$, were collected at every 0.4 dimensionless time unit defined as h/U_0 from the detailed simulation results. From the collected data, we computed the average mean velocity field, $U(x) = \frac{1}{N}\sum_{j=1}^{N} \tilde{u}_j(x)$, subtracted it from the snapshots, and got $u_1(x), u_2(x), \cdots, u_N(x)$. From this set of data, $u_1(x), u_2(x), \cdots, u_N(x)$, we computed the POD basis functions and eigenvalues, which is proportional to the kinetic energy captured by each mode, using the procedure described in Section III.1. [11]

---

[11] In principle, the inner product in V should be computed by integration over the domain. However, it is approximately proportional to the inner product of the vectors, $\bar{u} = [u(x_1)\ u(x_2) \cdots u(x_n)]^T$ where x_j is the

The mean velocity profile, $U(x)$ is shown in Figure 14. The reattachment length shown in Figure 14 is slightly less than 5, which is within a reasonable range, while predictions from other 2D simulations of this type of flows usually give unreasonable reattachment length at high Reynolds number [25]. In the context of reduced order modeling, it may be considered way more accurate than necessary.

Accepting the accuracy of the data is adequate, we performed POD analysis on the data. We construct two sets of basis functions. The first one is based on the standard POD method, which is described in Section III.1. We label these as the standard POD basis functions. The second one is obtained with the modified POD method, which is described in Section III.3. These are referred as the modified POD basis functions.

Before going into the construction of modified basis functions, we will discuss the results from standard POD analysis. The first thing we can check by POD analysis is how much kinetic energy is concentrated on the first few number of modes. This can be seen as the index of the finite-dimensionality of the system. To find out the kinetic energy content, we can use the fact that the eigenvalue of the covariance matrix correspond to the average kinetic energy projected on each basis function. The eigenvalues and the cumulative kinetic energy–cumulative sum of eigenvalues–are obtained from standard POD analysis and shown in Figure 15 and Figure 16. The unsteady kinetic energy contained in the first 20 modes corresponds to about 75% of the total unsteady kinetic energy. This is less than what we have observed in other low Reynolds number flows [31, 32], and shows how challenging the reduced order modeling of this high Reynolds number flow is.

The next things we are interested in are the spatial structure of POD basis functions and the temporal behavior of their amplitudes. To check the spatial pattern, the first eight standard basis functions are plotted from Figure 17 to Figure 24. It can be easily recognized that there are pairings of odd and even numbered modes. One can be considered as a sine type wave, and the other can be considered as a cosine type wave, which is obtained by shifting the sine type wave. The pairing of low-order modes occurs naturally in convective flows, because the flow supports traveling waves in the streamwise direction. The fact that the flow supports the traveling wave

---

location of the jth grid point, if the domain is uniformly meshed. We assume this inner product of vectors as a correct representation of the inner product in V. Hence, it should be noted that the eigenvalue does not exactly correspond to the kinetic energy contained in each mode, but is proportional to it.

can be also verified by examining the temporal behavior of the amplitude of each POD basis function. To examine temporal behaviors, we projected the trajectory of the data on the subspace consisting of the paired basis functions as shown in Figure 25 and Figure 26. The amplitudes of the mth and nth basis functions, which are denoted by α_m and α_n here, form a circle if they are paired as one traveling wave. Clearly, this is true for the pairs of odd and even modes such as (α_1, α_2) and (α_3, α_4). Additionally, we can check the trajectory projected over the plane (α_1, α_3) to see the frequency ratio of these two variables. It is shown in Figure 27. The wedge-shaped curve implies that α_3 experiences two cycles for one cycle of α_1.

Another way to examine this pairing phenomenon is computing time correlation between amplitudes of basis functions. The time correlation between the amplitudes of the mth and nth basis functions are defined as follows.

$$g_{mn}(t) = \lim_{T\to\infty} \frac{\frac{1}{T}\int_{t'=0}^{T} \alpha_m(t'-t)\alpha_n(t')dt'}{\left(\frac{1}{T}\int_{t'=0}^{T}(\alpha_m(t'))^2 dt'\right)^{1/2}\left(\frac{1}{T}\int_{t'=0}^{T}(\alpha_n(t'))^2 dt'\right)^{1/2}}. \tag{42}$$

In practice, we use large number of snapshots to compute the average instead of computing the limit $T \to \infty$. Because the convolution integral in the numerator is interpreted as a multiplication in frequency domain, $g_{mn}(t)$ vanishes when α_m and α_n do not share oscillations at same frequency.

The time correlation functions for $m = 1$ and $m = 3$ are plotted in Figure 28 and Figure 29. For $m = 1$, we can clearly recognize that α_1 bears strong correlation to α_2 by observing that the amplitude of $g_{12}(t)$ is much larger than that of other curves. Also, we can identify the dominant frequency of α_1 by observing the period of $g_{12}(t)$. It is about 0.07, which lies in the range of $St = O(0.1)$. This again confirms the qualitative description of this type of flows given in Chapter II.

However, the case with α_3 is a little more complex. As shown in Figure 29, α_3 bears strong correlation to its conjugate α_4, but it also shows comparable correlation to α_6. This implies that α_3, α_4, α_5 and α_6 are all strongly correlated to one another. The dominant frequency of all these modes is about 0.14, which is twice of that of α_1 and α_2, as mentioned before. The

occurrence of strong correlation among α_3, α_4, α_5 and α_6 is not a surprise. The shapes of the 5th and 6th POD basis functions given in Figure 21 and Figure 22 show strong similarity to the 3rd and 4th POD basis functions given in Figure 19 and Figure 20. To show the similarity more clearly, we plot the vertical velocity component of these basis functions at $y = 1$ in Figure 30 and Figure 31. They all have the same wave length in the streamwise direction, but show different modulations of amplitude. The 3rd and 4th basis functions show large amplitude at the middle of the domain, and have an envelope with nodes at the step ($x = 4$) and at the exit boundary ($x = 24$). The 5th and 6th basis functions show large amplitude only near $x = 10$ and $x = 20$, and have a node of their envelope at $x = 14$, which is the middle point between the step and the exit boundary. Additionally, Figure 32 shows that the different modulation of the amplitude can match the 3rd and 5th basis functions very closely. This striking similarity of these basis functions implies that the 5th and 6th POD basis functions are actually variants of the 3rd and 4th ones. More precisely, the trajectory mostly lies on the span of the 3rd and 4th POD basis functions, but leaves the plane to go into the span of the 5th and 6th POD basis functions. This phenomenon can also be seen in the plot of amplitudes in Figure 33. The radius of the trajectory projected on the 5th and 6th basis functions, $\sqrt{{\alpha_5}^2 + {\alpha_6}^2}$, is amplified out of phase to that of the 3rd and 4th, $\sqrt{{\alpha_3}^2 + {\alpha_4}^2}$.

Also, we can find these basis functions experience a strong influence from the shape of simulation domain. Especially, the fact that the wave length of 'envelopes' for the 3rd, 4th, 5th and 6th basis functions are fairly large and actually comparable to the length of the overall domain Ω implies that this modulation of amplitudes may have been introduced by the numerically imposed exit boundary condition. It is more plausible that they all form one traveling wave in the streamwise direction in real flows, where the exit is located at a further downstream.

Finally, we compare the results of POD analysis to the results of linear stability analysis described in Chapter II. Although the quantitative model of this saturated flow cannot be obtained by linear stability analysis, some features can still be captured. For example, when we compute the local absolute mode frequency at $x = 5.7$, where the mean velocity profile $U(x,y)$ exhibits maximum back flow, we obtain $\omega_0 = 0.430 + 0.134i$, which corresponds to $St = \frac{\omega_{0,r}}{2\pi} = 0.0684$. This value is very close to the frequency of oscillation in (α_1, α_2) plane, which was $St \cong 0.07$. This result implies that the 1st and 2nd POD basis functions would be very

similar to the linear mode, which is the eigenfunction of the corresponding Rayleigh equation. We can check whether this is true by computing the eigenfunction of the Rayleigh equation corresponding the local absolutely unstable mode at x = 5.7. The result is shown in Figure 34. The perturbation streamfunction obtained by integrating the 1st POD basis function is very similar to the real part of the eigenfunction, and the same statement is true for the 2nd POD basis function and the imaginary part of the eigenfunction.[12] This seemingly unreasonable coincidence between the eigenfunction, which is based on the completely linear description, and the POD basis functions, which is based on the fully nonlinear simulation result, is actually not a big surprise, because the energy transfer from the mean velocity profile $U(x,y)$ to the fluctuation $u(x,y,t)$ is dominated by linear terms in NSE. To see this, we can check the fluctuation energy evolution equation obtained by taking the scalar product of (34) and $u(x,y,t)$. Using the divergence-free condition and the homogeneous Dirichlet BC for $u(x,y,t)$,

$$(u_t + u\cdot\nabla u + u\cdot\nabla U + U\cdot\nabla u + U\cdot\nabla U - \nu\Delta u - \nu\Delta U - \nabla p, u)$$
$$= \frac{1}{2}\frac{d}{dt}|u|_{L2}^2 + \nu\|u\|^2 + (u\cdot\nabla U, u) + (U\cdot\nabla U - \nu\Delta U, u) = 0. \qquad (43)$$
$$\text{(i)} \qquad \text{(ii)} \qquad \text{(iii)}$$

The nonlinear term $(u\cdot\nabla u, u)$ vanishes, and three groups contributing the evolution of fluctuation kinetic energy can be classified as: (i) viscous dissipation, (ii) linear interaction between U and u and (iii) the residue occurring because U is not a solution of steady NSE. (i) is positive definite and always stabilizing the flow. (iii) vanishes when we average it, because its dependency on u is linear, and the time average of u is 0. Therefore, the main energy transfer from the mean flow to the fluctuation is still dominated by the linear interaction (ii) even in the fully nonlinear regime, which in turn implies that the frequency of dominant oscillation and the shapes of the most energetic POD basis functions should be very similar to the result of linear stability analysis.

We can extend this analysis to higher order modes, for example, the 3rd, 4th, 5th and 6th ones. It can be considered as secondary instability analysis using the mean velocity profile and the 1st basis function as a base flow. We separate $u(x,y,t)$ in (34) into two parts, i.e.

---

[12] Note that the adjectives 'real' and 'imaginary' are arbitrarily chosen. We can multiply any complex constant to the eigenfunction, and the resulting function will remain as an eigenfunction corresponding to the same eigenvalue.

$u(x,y,t) = \alpha_1(t)\Phi_1(x) + u'(x,y,t)$.[13] By taking the scalar product of (34) and u', we have the following energy evolution equation for u'.

$$\frac{1}{2}\frac{d}{dt}|u'|_{L2}^2 + \nu\|u'\|^2 + \dot{\alpha}_1(\Phi_1,u') + \alpha_1(U\cdot\nabla\Phi_1 + \Phi_1\cdot\nabla U - \nu\Delta\Phi_1,u')$$
$$\text{(i)} \qquad \text{(ii)} \qquad \text{(iii)}$$
$$+ (U\cdot\nabla U - \nu\Delta U,u') + (u'\cdot\nabla U,u') + \alpha_1(u'\cdot\nabla\Phi_1,u') + \alpha_1^2(\Phi_1\cdot\nabla\Phi_1,u') = 0 \qquad (44)$$
$$\text{(iv)} \qquad \text{(v)} \qquad \text{(vi)} \qquad \text{(vii)}$$

To simplify the analysis, we assume that $u' \cong \alpha(t)\Phi(x)$. Then, we can group terms as follows: (i) viscous dissipation, (ii, iii) terms with average contribution proportional to $\overline{\alpha_1\alpha}$, (iv) the residue occurring because U is not a solution of steady NSE, (v) linear interaction between U and u', (vi) a term with average contribution proportional to $\overline{\alpha_1\alpha^2}$ and finally (vii) a term with average contribution proportional to $\overline{\alpha_1^2\alpha}$. (i), (iv) and (v) have the same effects as in (43), and we do not discuss them any more. The new players (ii), (iii), (vi) and (vii) are dependent on $\overline{\alpha_1\alpha}$, $\overline{\alpha_1\alpha^2}$ or $\overline{\alpha_1^2\alpha}$. Each term shows nontrivial contribution in different cases. When α_1 and α has the same frequency, the terms dependent on $\overline{\alpha_1\alpha}$ may have nontrivial contribution in average. This case can occur when u' has a conjugate mode of α_1 and Φ_1, i.e. α_2 and Φ_2, which has the same frequency as α_1 and Φ_1. However, as shown in Figure 25 and Figure 28, α_2 has a phase shift by 90 degree from α_1, so $\overline{\alpha_1\alpha_2}$ vanishes. This implies that (iii) does not contribute to the energy evolution of u' in average. Also, by the properties of POD basis functions, u' must be orthogonal to Φ_1, so (ii) vanishes, too. Therefore, to examine the higher order modes, we should examine (vi) or (vii), which have dependency on $\overline{\alpha_1\alpha^2}$ or $\overline{\alpha_1^2\alpha}$. These terms can act as exciting sources only when the frequency of α is the half (vi) or the twice (vii) of that of α_1. The half wave is not observed in this case, but we have the doubling of the frequency. The amplitudes of the 3rd, 4th, 5th and 6th basis functions all show oscillations at a frequency two times larger than that of the 1st and 2nd ones. This fact supports the argument that the term (vii), which originates

[13] We can put $u(x,y,t) = \alpha_1(t)\Phi_1(x) + \alpha_2(t)\Phi_2(x) + u'(x,y,t)$ instead of considering only the 1st basis function. However, the formula obtained from this substitution is unnecessarily complicating for the illustrative purpose of the formula.

from secondary instability analysis of the base flow, acts as a main energy source for these higher order modes. Also, because the wave length of $\Phi_1 \cdot \nabla\Phi_1$, which is in (vii), in the streamwise direction is the half of that of the 1st and 2nd basis functions, we conclude that the dominant wave length of the 3rd, 4th, 5th and 6th basis functions in the streamwise direction will be most likely half of that of the 1st and 2nd basis functions. By observing the shapes of basis functions from Figure 17 to Figure 22, we can find that this is roughly true at least at the downstream of the reattachment point.

Here, we finish our discussion of the standard basis functions. Now, we want to apply the 'nested weighting procedure' described at the end of Section III.3. We consider the following set of weighting functions. The domain of interest, Ω', is given in Figure 13. It includes the recirculation zone, and is slightly more extended to the downstream.

$$\begin{aligned} &\widetilde{w}_1(x) = 1 && \widetilde{n}_1 = 4 \text{ (corresponding to the first 4 modes),} \\ &\widetilde{w}_2(x) = \begin{cases} 1 & (x \in \Omega') \\ 0 & (x \in \Omega'') \end{cases} && \widetilde{n}_2 = 16 \text{ (corresponding to the next 16 modes).} \end{aligned} \tag{45}$$

(45) is chosen based on the observation made for the standard POD basis functions from Figure 17 to Figure 24. The basis functions from the 7th to 8th show localization of oscillations in small regions, while those from the 1st to the 4th are more or less continuously distributed over the whole domain Ω. Also, as described in the previous paragraph, the 5th and 6th basis functions probably are variants of the 3rd and 4th, modulated in a different way. With the discussion given in previous paragraphs, we conclude that the dynamics within Ω' and the dynamics within Ω'' are related mostly by the first 4 basis functions, which are continuously distributed, and the 5th and 6th basis functions try to capture intermittent behaviors or reflection from the exit boundary. Therefore, we try to capture the 'overall' dynamics by taking the first 4 standard modes, and then concentrate the next 16 modes on capturing the detailed dynamics within Ω', neglecting intermittent behaviors or reflection from the exit boundary. Finally, if the dynamics of the overall system is really dominated by the dynamics of absolutely unstable region in Ω' as described in Chapter II, we may hope that increasing the accuracy of projection in Ω' will also result in enhancement of overall quality of the reduced order model.

Using this line of reasoning, we applied the 'nested weighting procedure' in Section III.3 to (44), and obtained 20 modified basis functions. The resulting basis functions are different from those obtained from the standard POD method. One of the major differences is that these new

basis functions contain more detailed small-scale structures within Ω', which may be captured only with higher number of modes if we had used the standard POD method. In Figure 35, we can see the discrepancy between the length scales especially near the step.

With these sets of basis functions, reduced order models were constructed by Galerkin projection method. Two reduced order models were constructed based on the standard POD basis functions. One was based on 20 POD basis functions and the other was based on 40 POD basis functions. Using the 'nested weighting procedure' in III.3, we also constructed a reduced order model based on the 20 modified basis functions.

III.4.2 Simulation Using Reduced Order Models and Discussion

We may check the quality of these models in two different ways. One is checking the velocity tracking capability at a fixed location. The other is checking the overall velocity profile at a particular time. In either case, the result from detailed simulation is considered as a correct solution, and becomes a model for benchmarking.[14]

First, velocity tracking capability was tested. Each component of the velocity is plotted for 4 different locations within the recirculation zone for all three models and compared to the detailed simulation result. The plots are given from Figure 36 to Figure 39. We observed that all models eventually showed stronger unsteadiness than that observed in detailed simulation. This is due to the fact that the length scales captured by the models are still within the range of integral length scale. Because of this limitation, Kolmogorov-type energy cascading is blocked and the kinetic energy is accumulated. To compensate this lack of dissipation, implementation of an eddy viscosity mechanism has been proposed [30], but it introduces additional unknown parameters, which should be identified. We did not use the method to avoid additional complication. Anyway, the purpose is not to understand long-term dynamics but to capture short-term behavior, so the large amplitude for later time is not a major problem here.

---

[14] The integration of reduced order models was performed using `ode15s` suite in MATLAB. The default method of integration in `ode15s` suite is NDFs (numerical differentiation formulas), but we can also use Gear's method [37]. Here, we used Gear's method to ensure the stability of integration.

Focusing on the short-term tracking property only, we find that the reduced order model with 20 standard POD modes reproduces the detailed simulation results at most up to $t = 10$, which is less than one period of the dominant oscillation, while the other two models follow the results of detailed simulation almost up to $t = 14$ or more. Especially, the superiority of the 40 mode model over the 20 mode model is obvious.

This statement is not universally valid of course. All models have difficulty reproducing the flow field very near the step. In Figure 36, all models fail to predict the peak at $t = 4$. However, even at those locations, the 20 modified mode model and the 40 mode model predict the occurrence of dominant peak at $t = 6$, while 20 standard mode model shows a significant lag. The reason why the prediction based on reduced order model is inaccurate near the step seems to be the fact that small vortices near the step at their initiation stage are not well captured by POD basis functions. Another exceptional case is Figure 37, where the prediction based on 20 modified basis functions fails to show oscillations at early stage up to $t = 6$. However, the model still captures the behavior after $t = 6$ slightly better than the model based on 20 standard basis functions. This implies that the loss of small oscillations does not always degrade the overall prediction capability of the reduced order model significantly, and that the quality of the model should be verified by checking how the global flow field shape is similar to the one we have from the detailed simulation.

With this point in mind, we compared the overall velocity field rather than checking point-wise velocity at a fixed location. See the velocity profiles from Figure 40 to Figure 44. The velocity field described by the 20 standard mode model rapidly loses the similarity to the detailed simulation results. On the other hand, the model based on the 20 modified basis functions captures the behavior of large-scale structures up to much longer period.

All these results show that superior accuracy can be obtained by more number of modes, which is a natural consequence, but it also implies that the model tuned by spatial weighting technique works well without increasing the number of modes. Although this is only one example, it shows the possibility that we can increase the accuracy without increasing the required number of modes by introducing appropriate weight functions. Especially, other flow problems involving wake phenomena usually share the same dilemma of extended domain of simulation, and this method can be applied to them.

Finally, it should be noted that the 40 mode model does not improve the simulation result as much as we expected. The grid used to construct the reduced order model seems to be too coarse to compute the derivatives of higher order POD basis functions, which contain small-scale structures, and it may harm the overall accuracy of the 40 mode model badly. The evaluation of these spatial derivatives is required, because we used Galerkin projection method to construct the reduced order models. Hence, this issue of differentiation can be avoided if we use other approaches to construct reduced order models, for example, system identification. The method combining POD method and system identification to construct reduced order models has been tried to model aeroelastic systems [38], and the method can also be easily brought into the context of backward-facing step flows. It is not within the scope of the current research, and should be considered as one of possible extension of the current work.

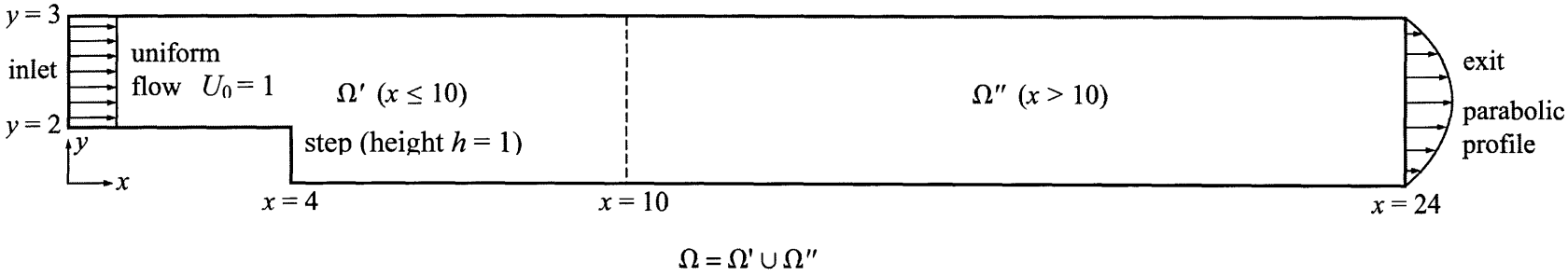

Figure 13 Illustrative sketch of the computational domain Ω, which is divided into two subdomains, Ω' and Ω''. Although we are only interested in the behavior of the system in Ω', Ω'' is included to avoid an unexpected effect of arbitrary boundary condition imposed on the exit. Note that the location of the step is $x = 4$.

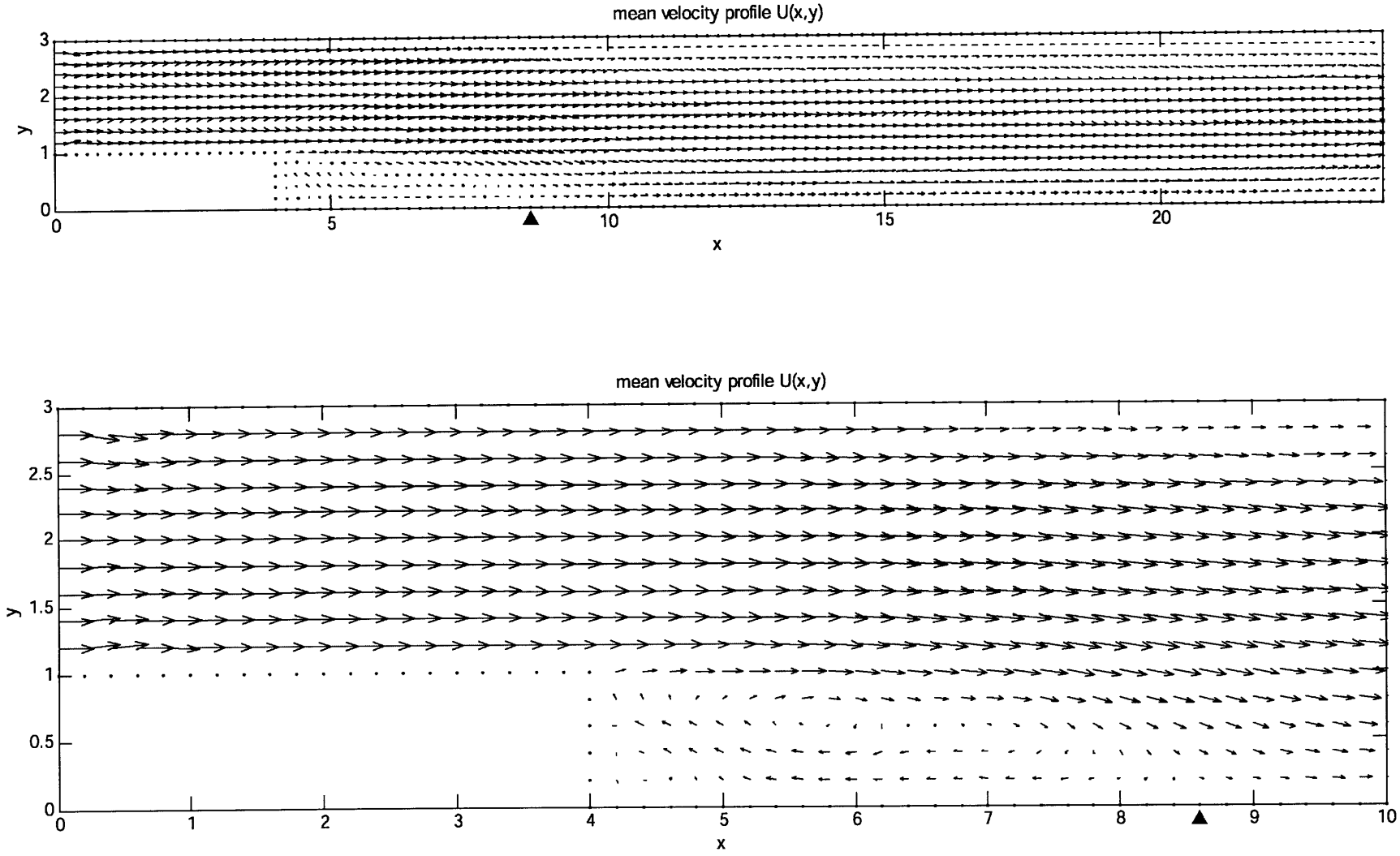

Figure 14 Mean velocity profile obtained by averaging 750 snapshots. The velocity profile in Ω' is magnified in the lower plot. The triangle locates the point of reattachment.

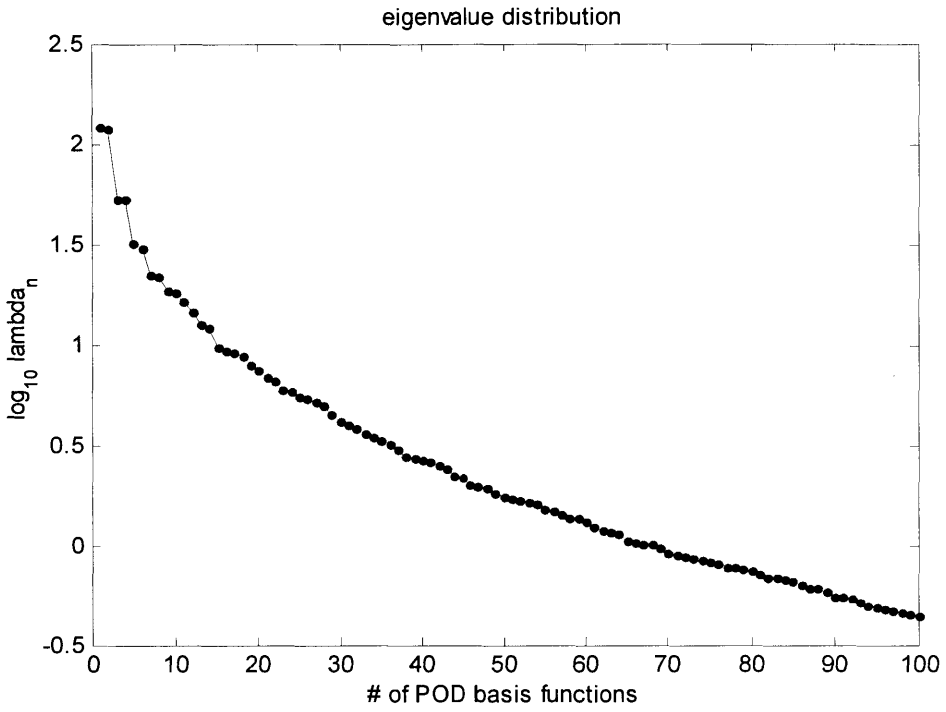

Figure 15 Eigenvalue distribution of covariance matrix *C*.

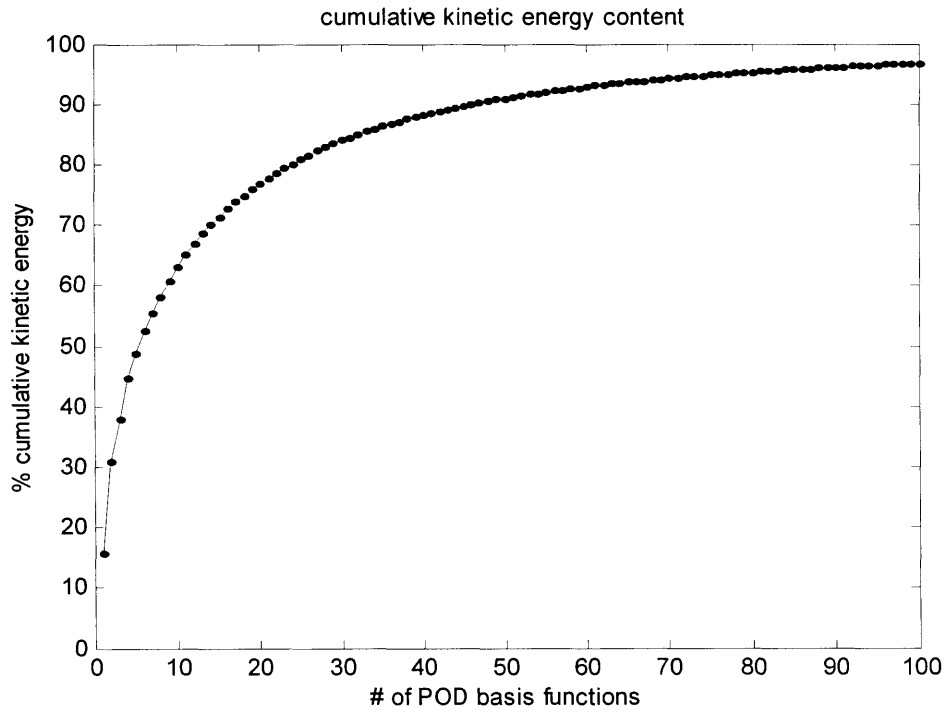

Figure 16 Cumulative kinetic energy distribution obtained by cumulative sum of eigenvalues of covariance matrix *C*.

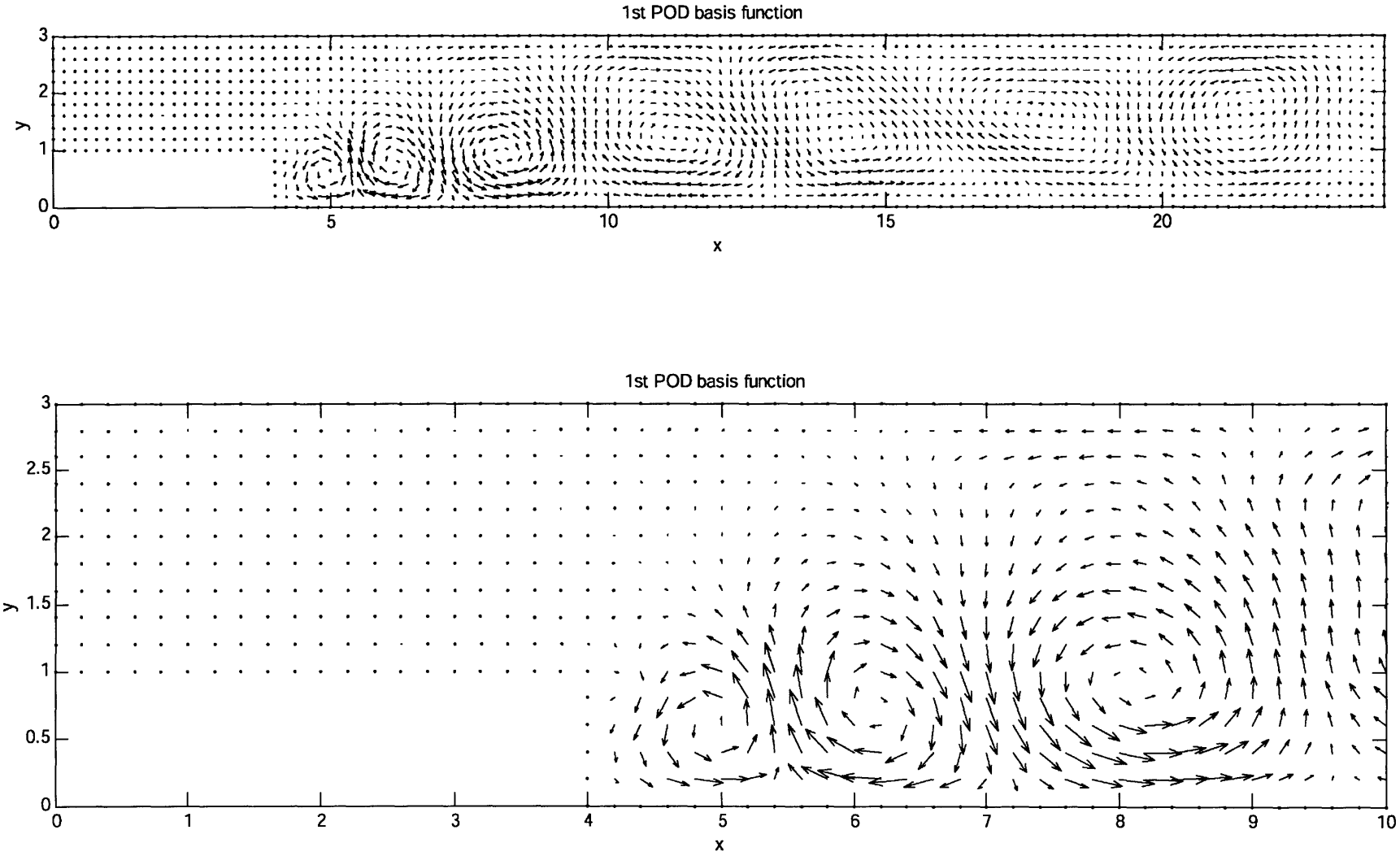

Figure 17 1st POD basis function obtained by applying standard POD method as described in Section III.1 for the whole domain Ω. The velocity profile in Ω′ is magnified in the lower plot.

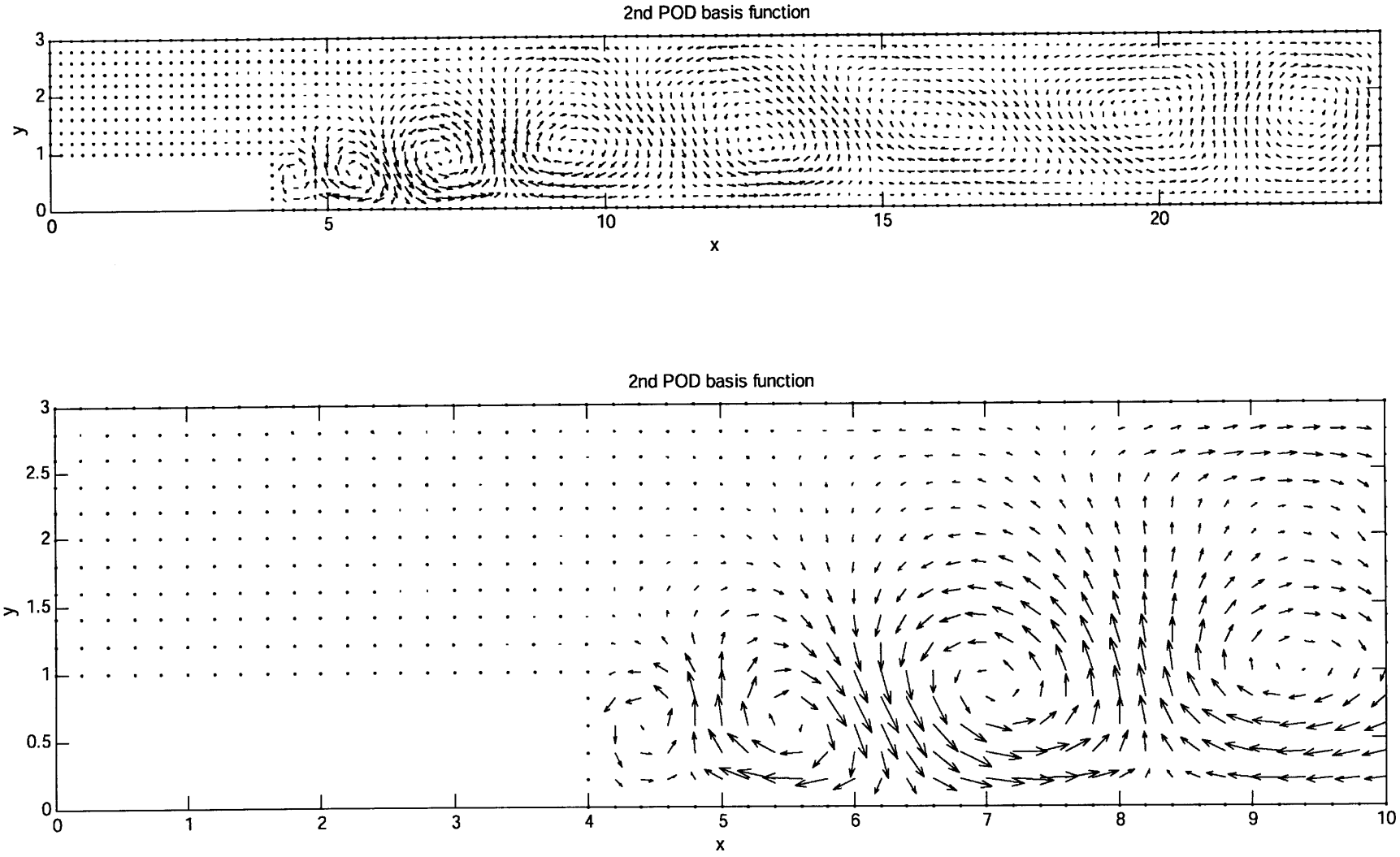

Figure 18 2nd POD basis function obtained by applying standard POD method as described in Section III.1 for the whole domain Ω. The velocity profile in Ω′ is magnified in the lower plot.

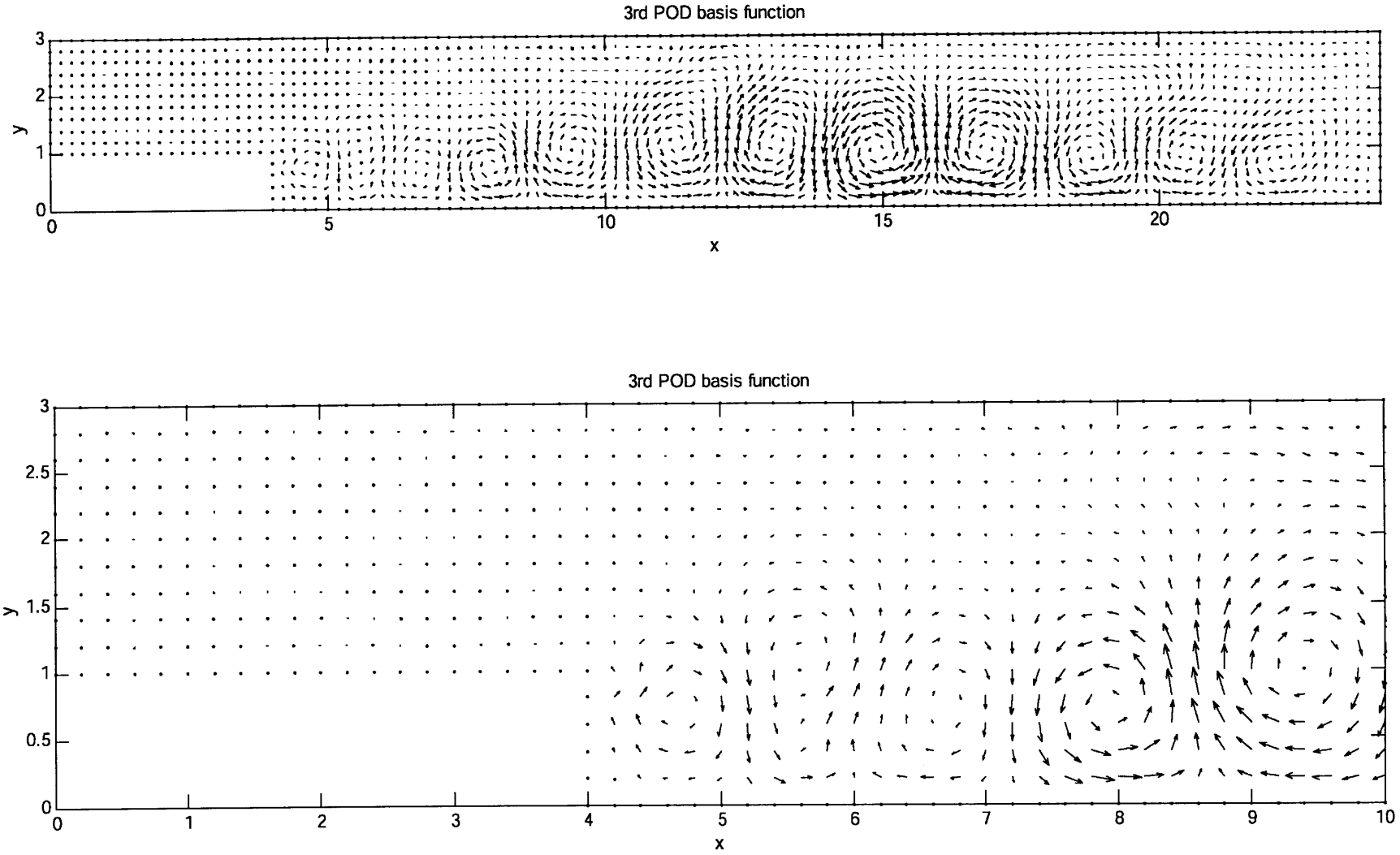

Figure 19 3rd POD basis function obtained by applying standard POD method as described in Section III.1 for the whole domain Ω. The velocity profile in Ω′ is magnified in the lower plot.

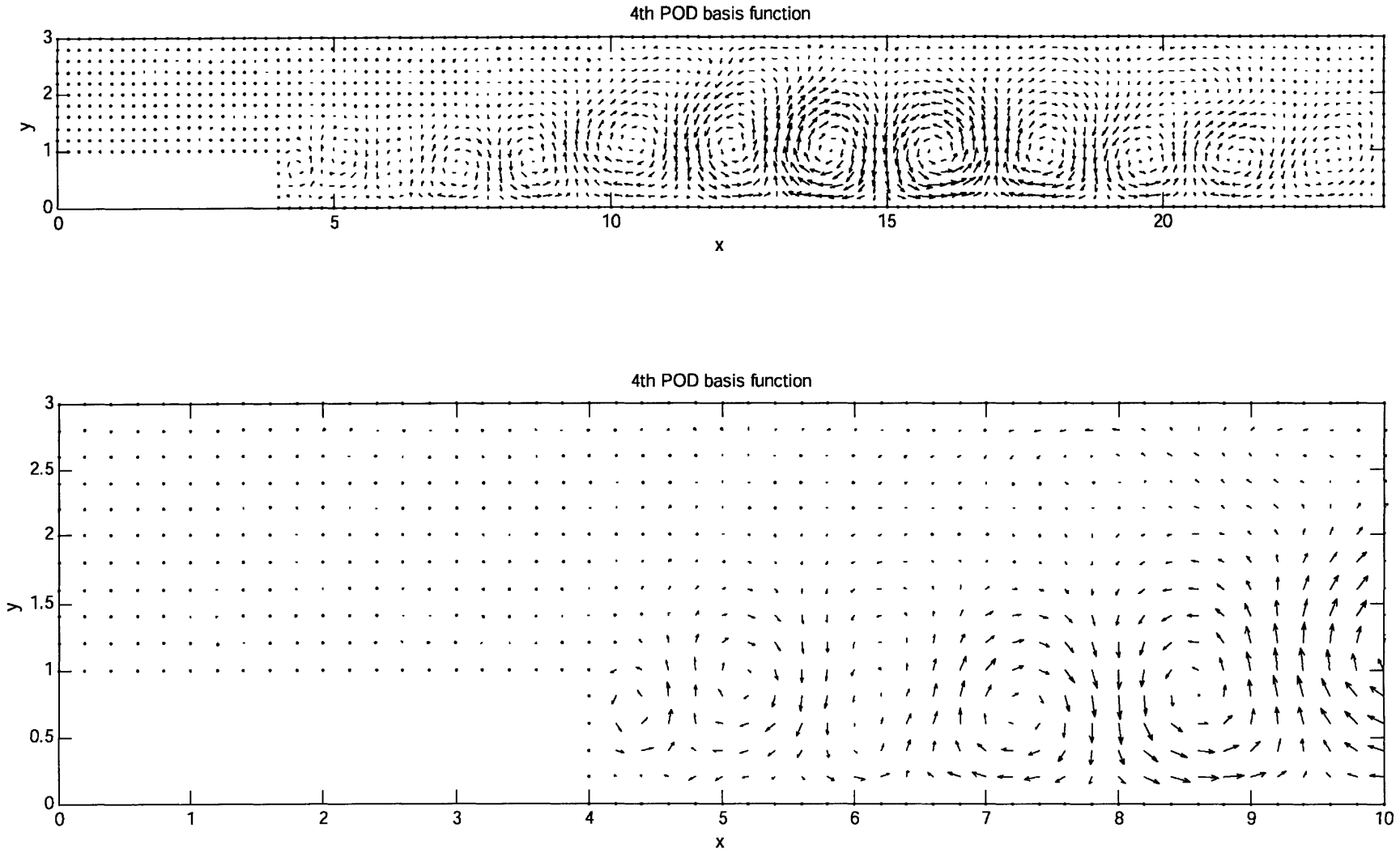

Figure 20 4th POD basis function obtained by applying standard POD method as described in Section III.1 for the whole domain Ω. The velocity profile in Ω' is magnified in the lower plot.

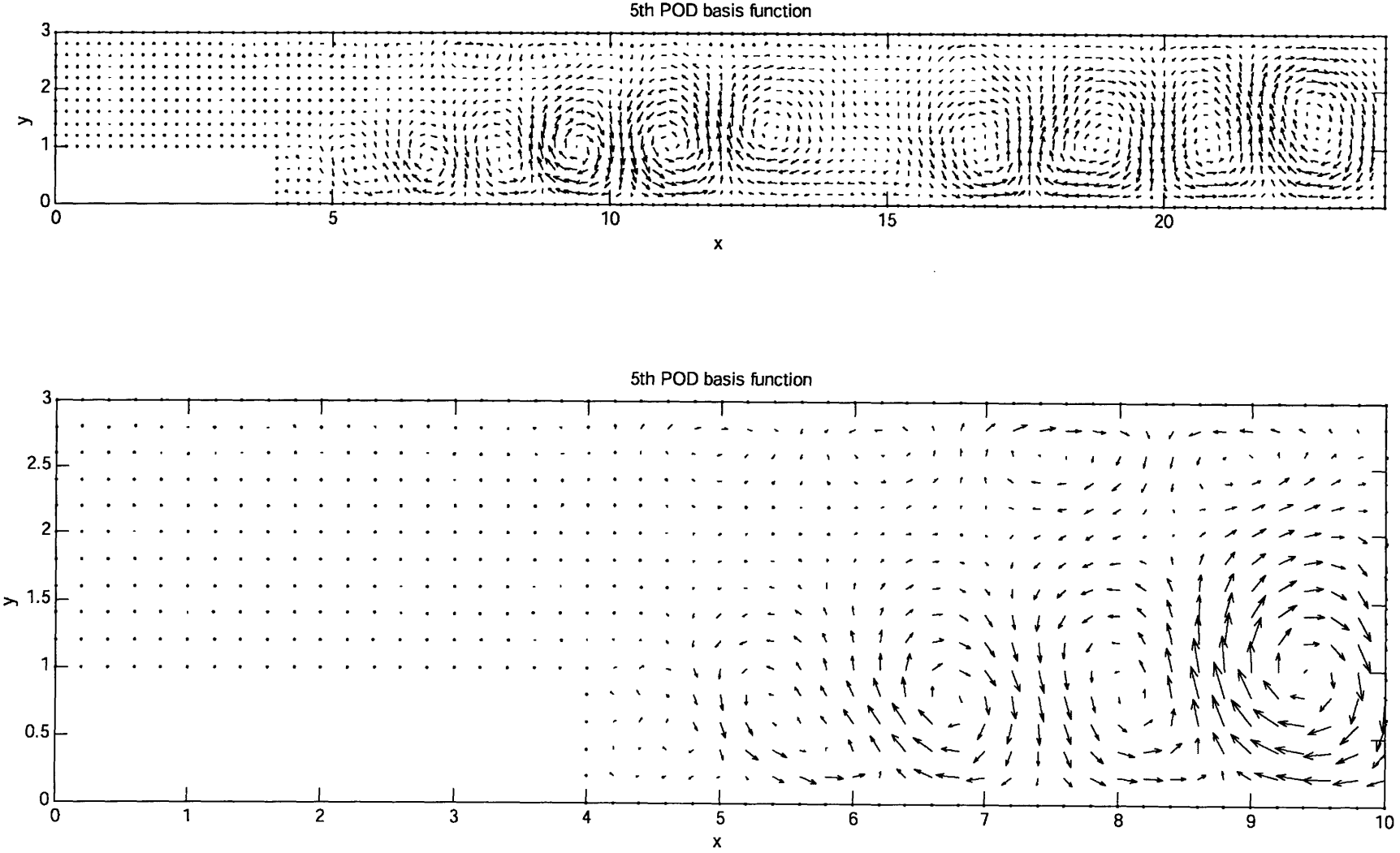

Figure 21 5th POD basis function obtained by applying standard POD method as described in Section III.1 for the whole domain Ω. The velocity profile in Ω' is magnified in the lower plot.

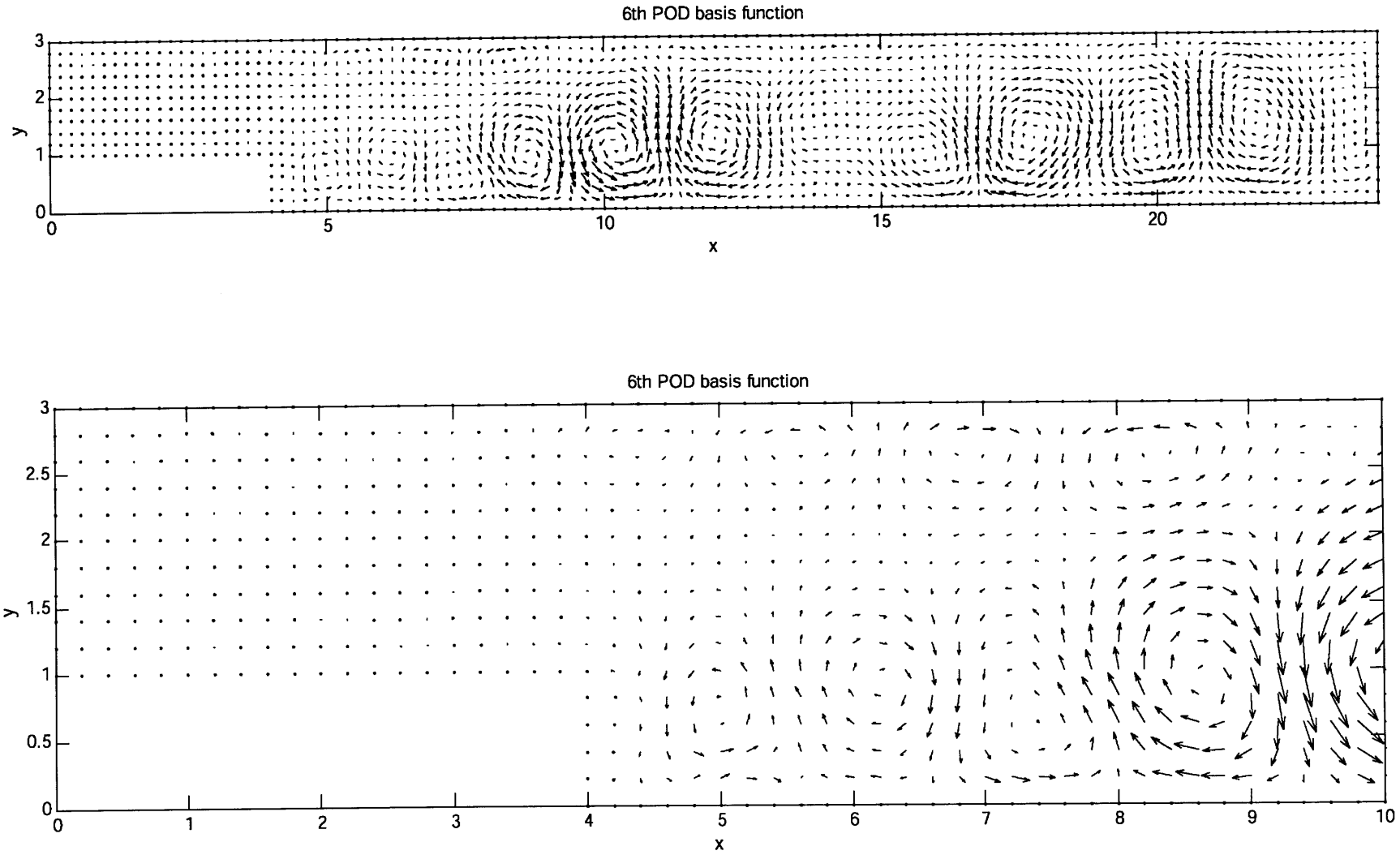

Figure 22 6^{th} POD basis function obtained by applying standard POD method as described in Section III.1 for the whole domain Ω. The velocity profile in Ω' is magnified in the lower plot.

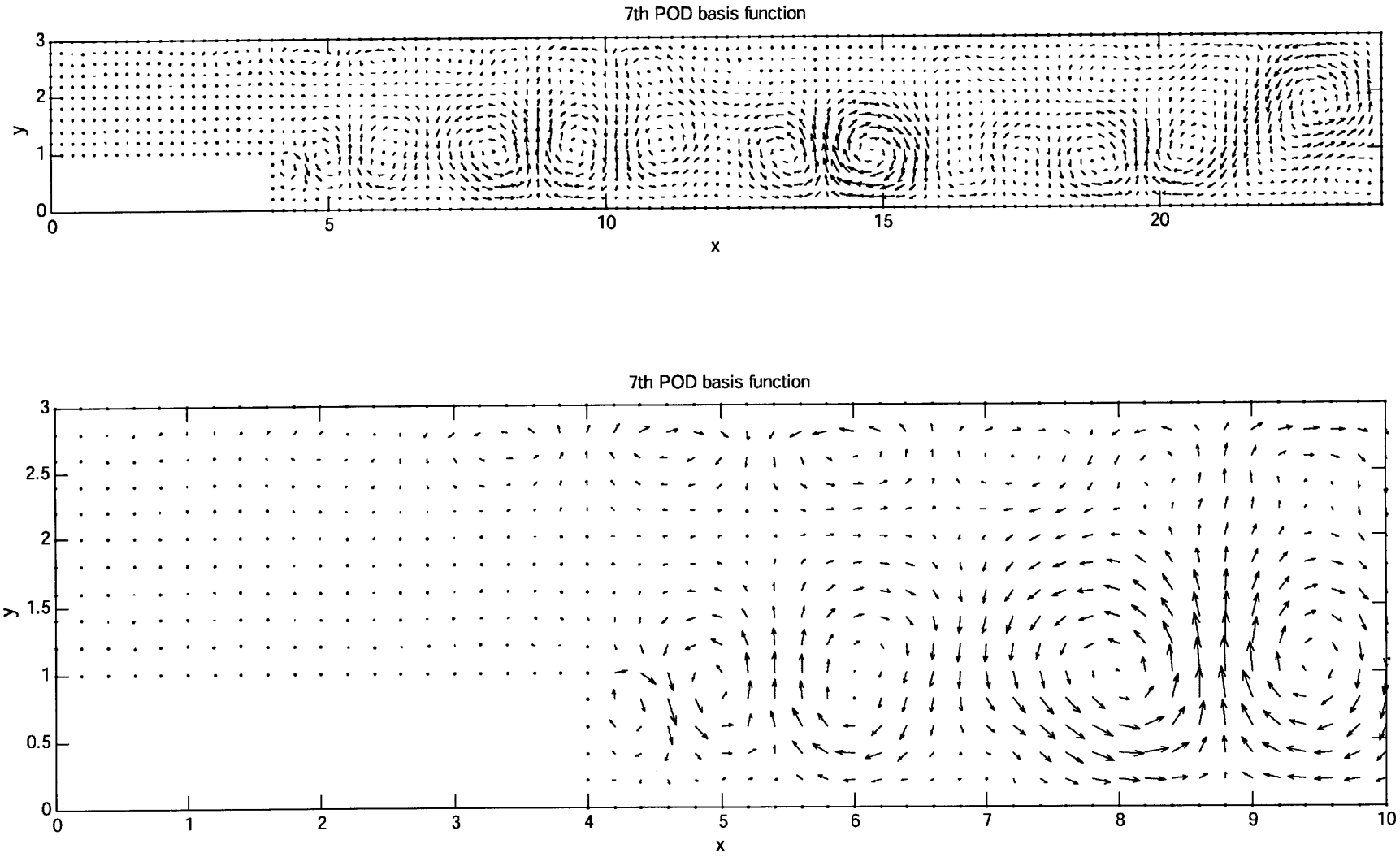

Figure 23 7^{th} POD basis function obtained by applying standard POD method as described in Section III.1 for the whole domain Ω. The velocity profile in Ω' is magnified in the lower plot.

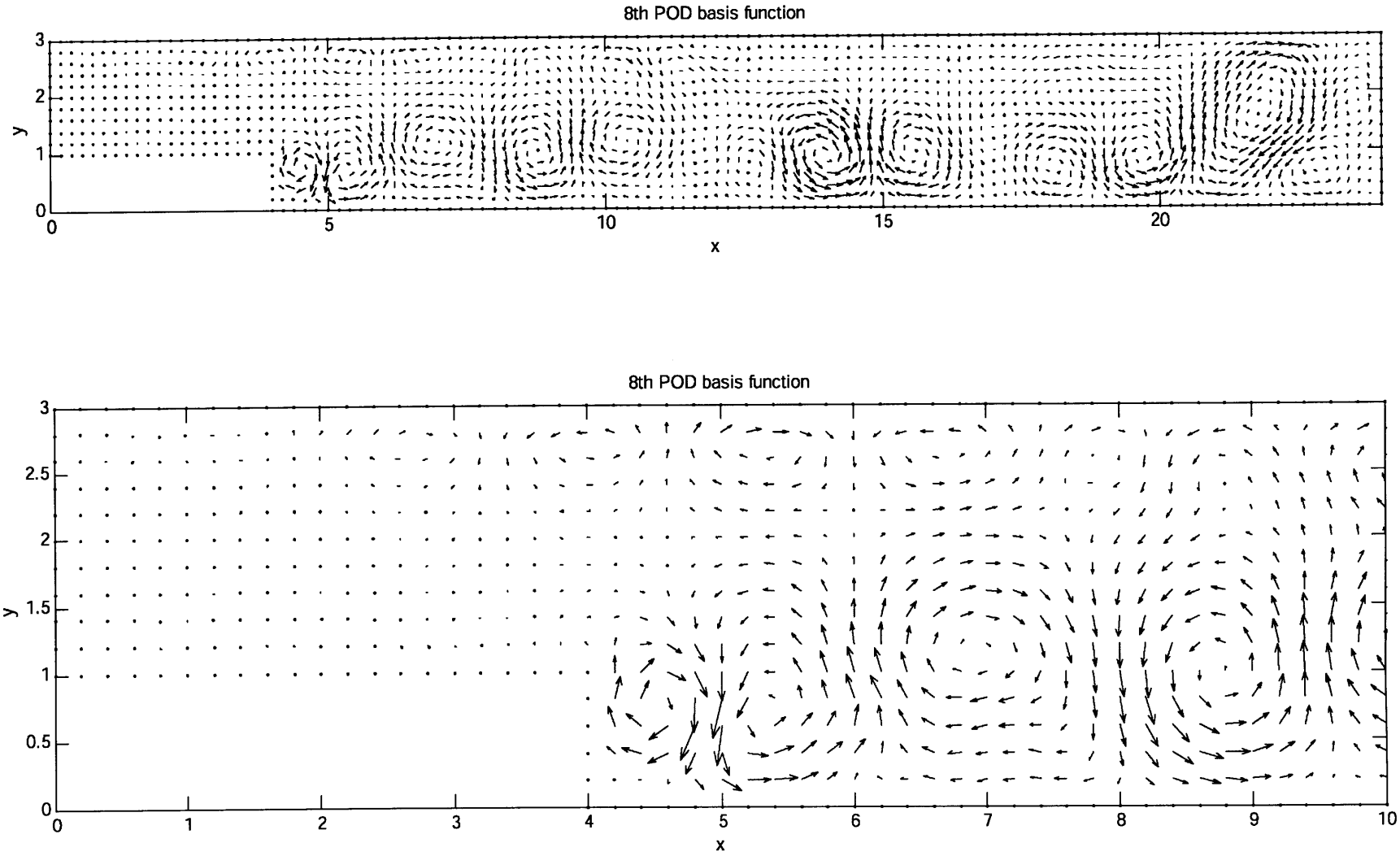

Figure 24 8^{th} POD basis function obtained by applying standard POD method as described in Section III.1 for the whole domain Ω. The velocity profile in Ω' is magnified in the lower plot.

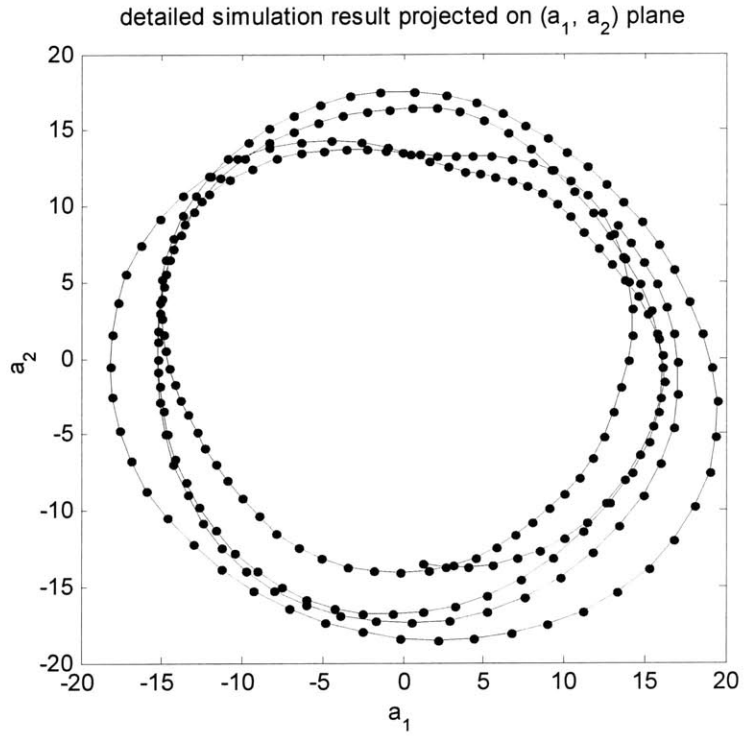

Figure 25 Trajectory of the detailed simulation results projected on the span of the 1st and 2nd basis functions.

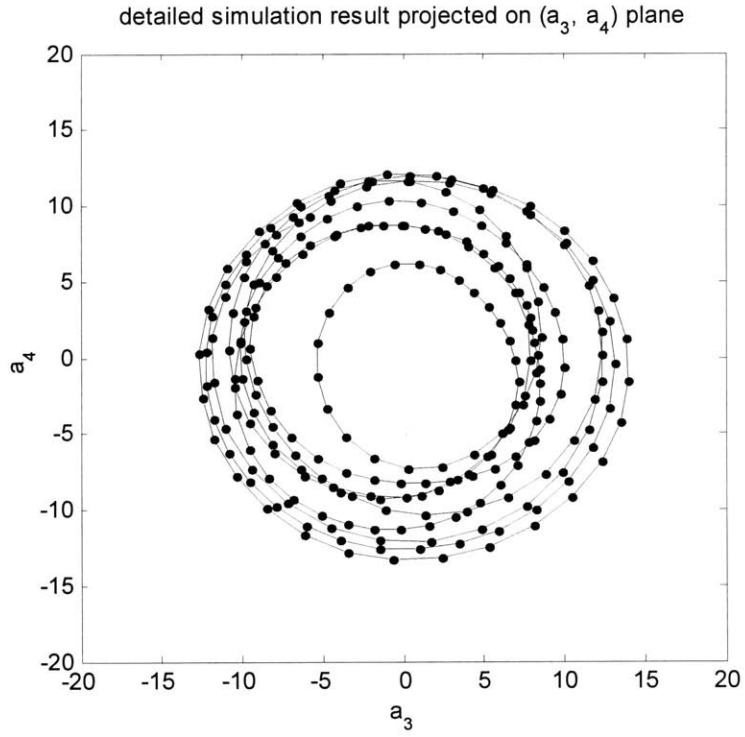

Figure 26 Trajectory of the detailed simulation results projected on the span of the 3rd and 4th basis functions.

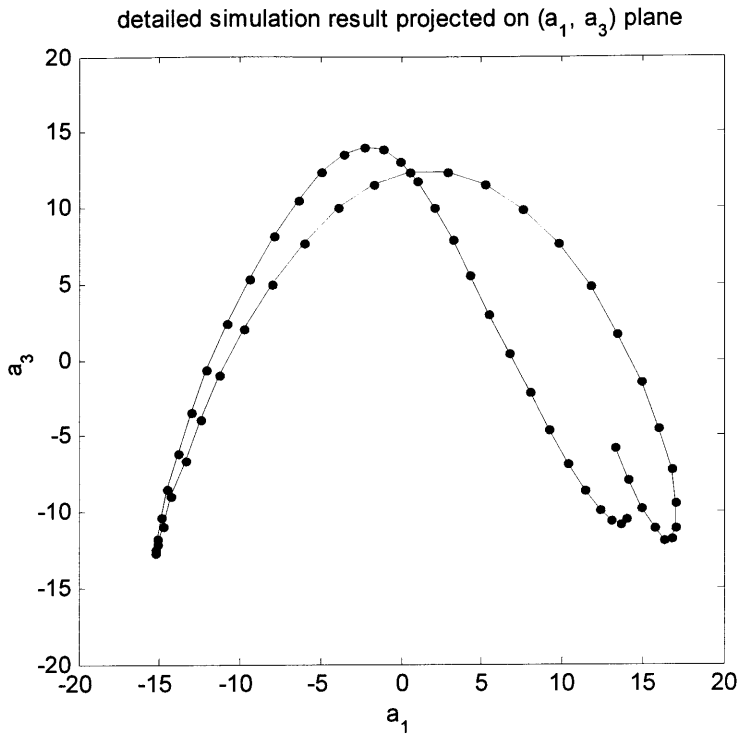

Figure 27 Trajectory of the detailed simulation results projected on the span of the 1st and 3rd basis functions. The number of data points is limited to about one period of the dominant oscillation in the flow to present the frequency ratio more clearly.

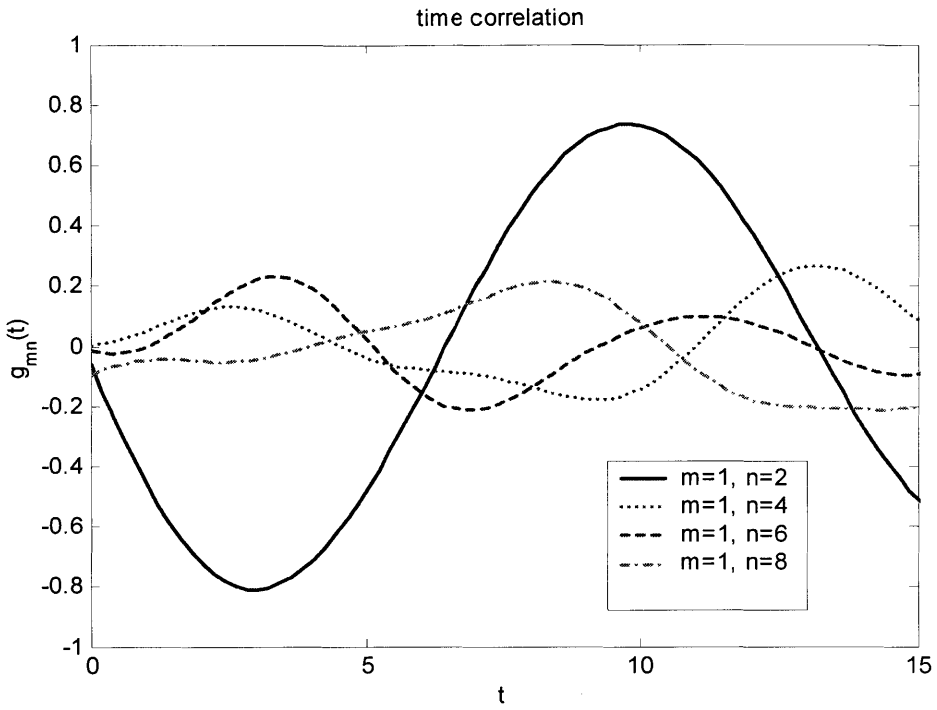

Figure 28 Plot of time correlation functions defined in (42) for $m = 1$.

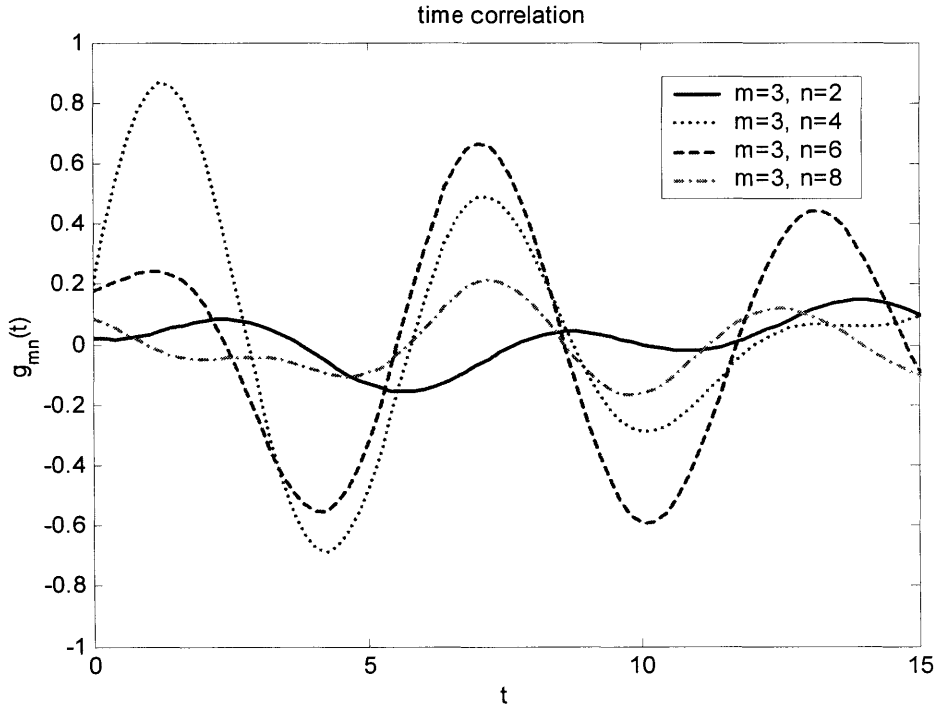

Figure 29 Plot of time correlation functions defined in (42) for $m = 3$.

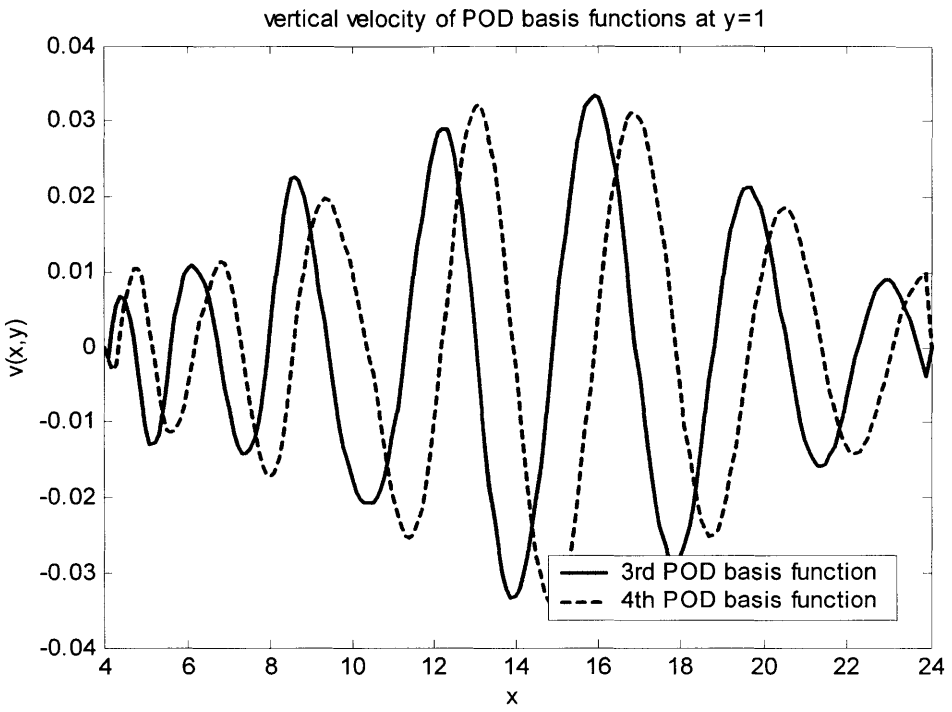

Figure 30 vertical velocity component of the 3rd and 4th POD basis functions at $y = 1$.

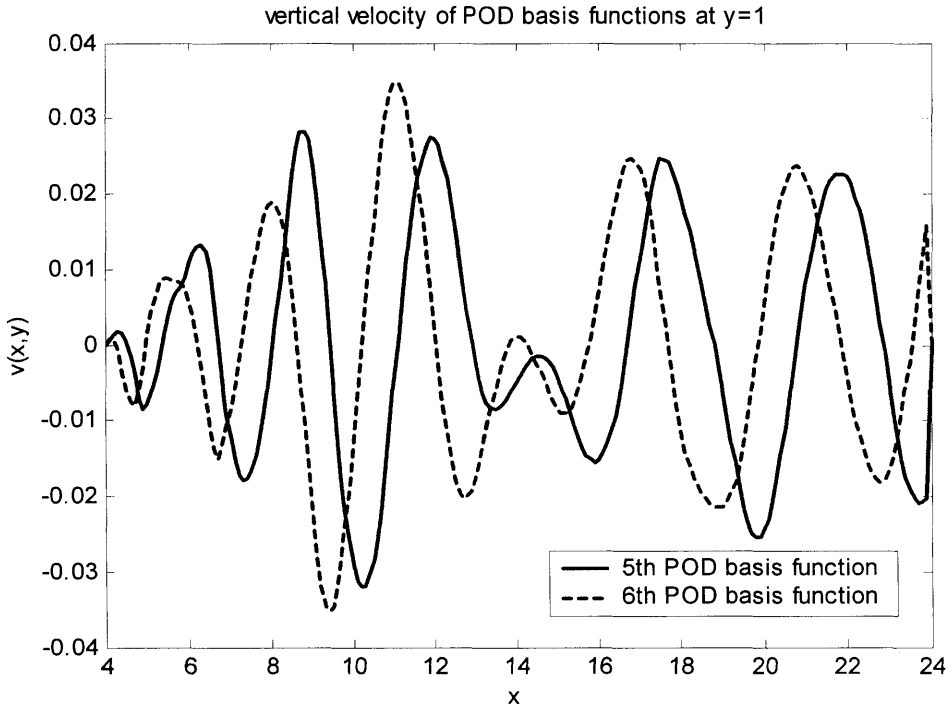

Figure 31 vertical velocity component of the 5th and 6th POD basis functions at $y = 1$.

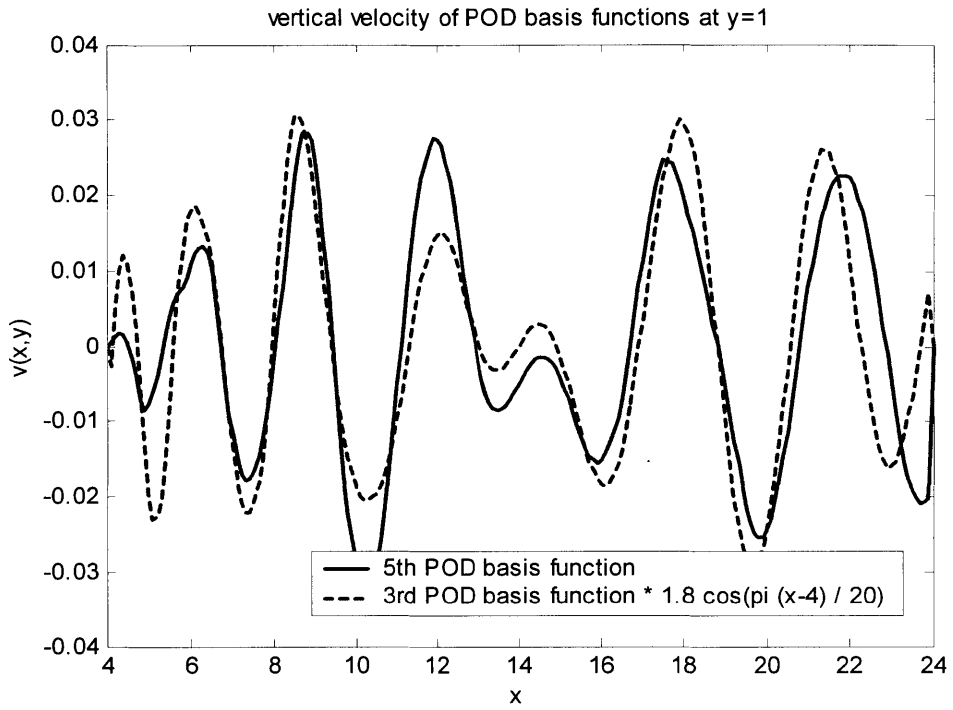

Figure 32 vertical velocity component of the 5th POD basis function and the modulated 3rd basis function at $y = 1$.

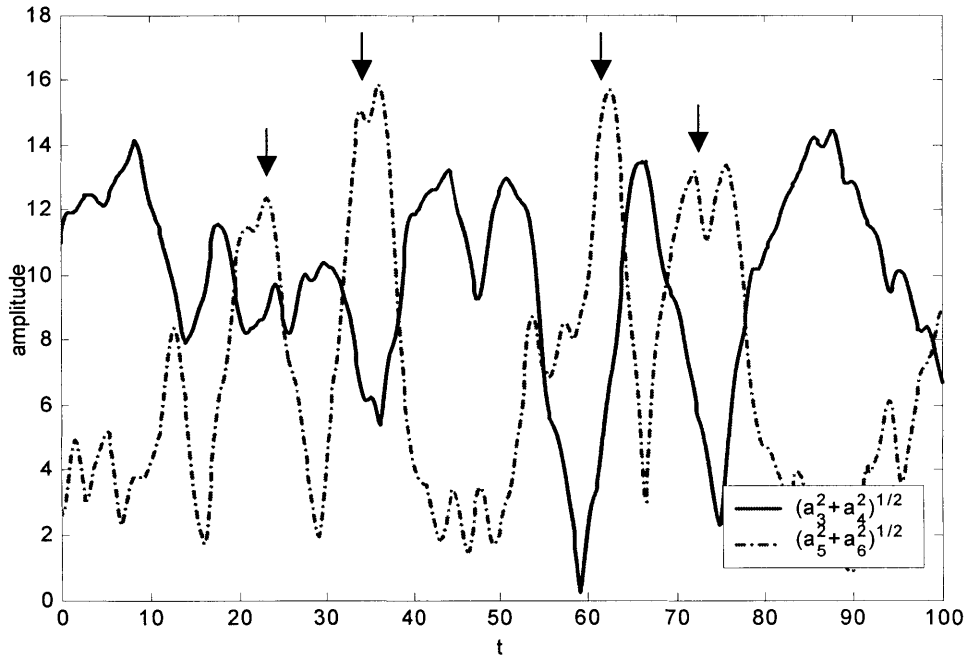

Figure 33 Radius of trajectory projected on the 3rd and 4th modes (solid) and on the 5th and 6th modes (dash-dot). The arrows indicate the excitations of the 5th and 6th modes occurring out of phase to the amplification of the 3rd and 4th modes.

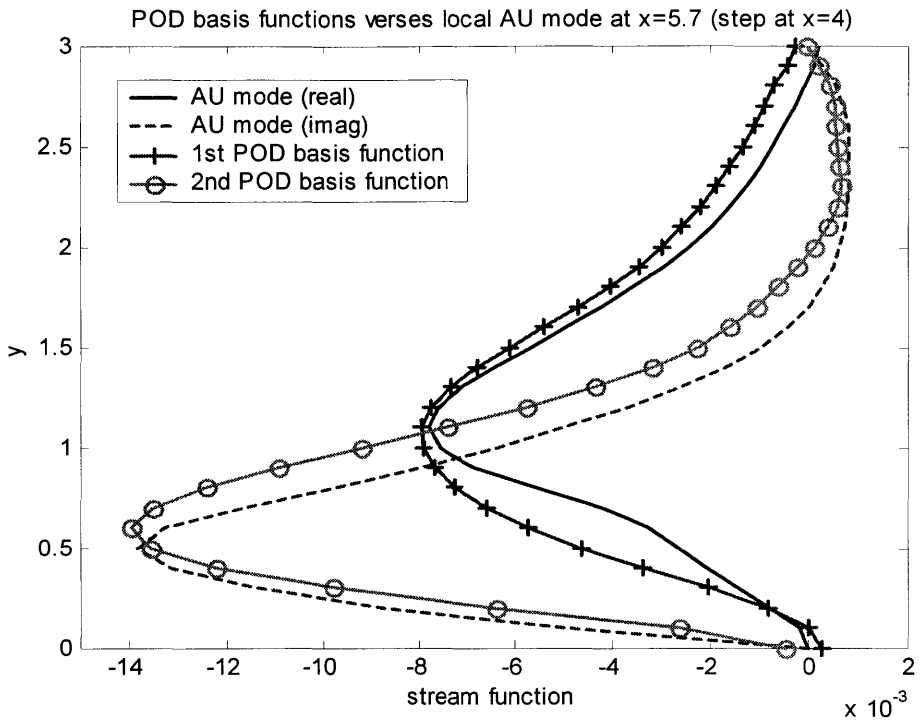

Figure 34 Perturbation stream functions obtained from the absolutely unstable mode and the 1st and 2nd POD basis functions at $x = 5.7$, where the flow exhibits maximum back flow. The step is located at $x = 4$.

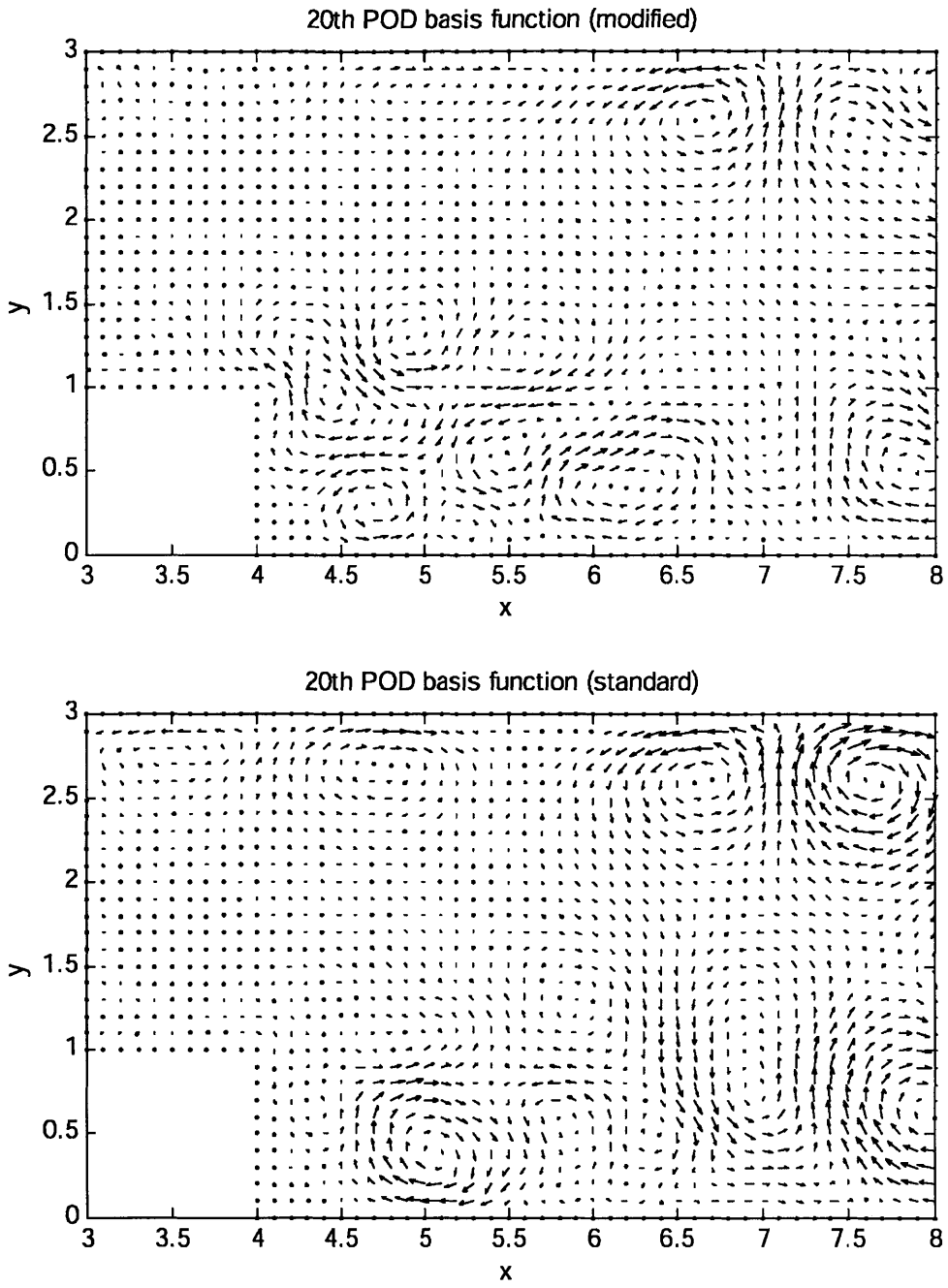

Figure 35 Plots of the basis functions showing the most detailed shape of structures in each group: modified (upper plot) and standard (lower plot). The length scale of the structure in the modified basis function is smaller than that in the standard one.

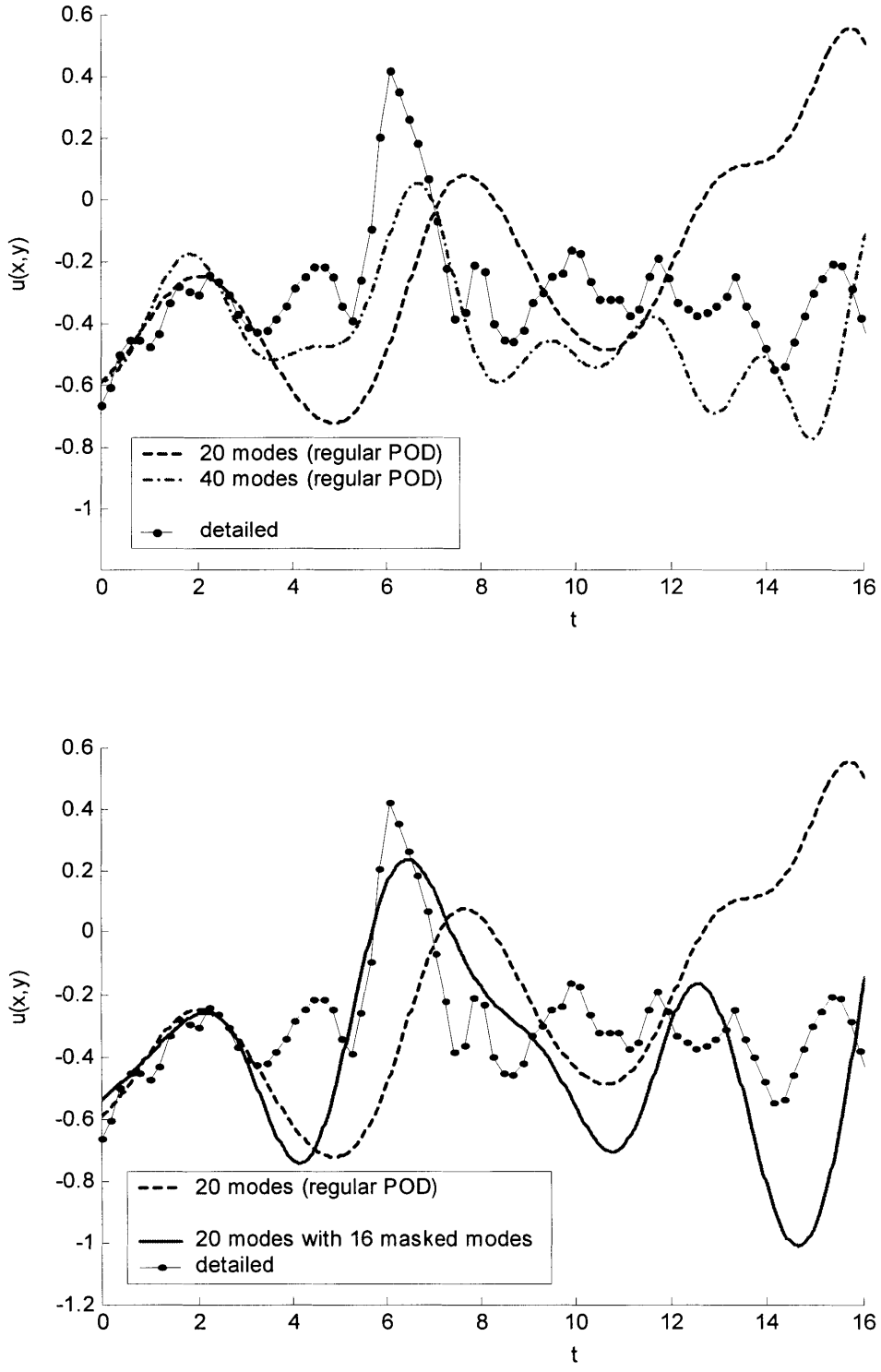

Figure 36 Streamwise velocity tracking at $x = 5$, $y = 0.5$. Note that the step lies at $x = 4$ in Figure 13. Model based on 20 modified basis functions: solid; 20 standard basis functions: dashed; 40 standard basis functions: dash-dot; detailed simulation result: solid/dotted at sampling points

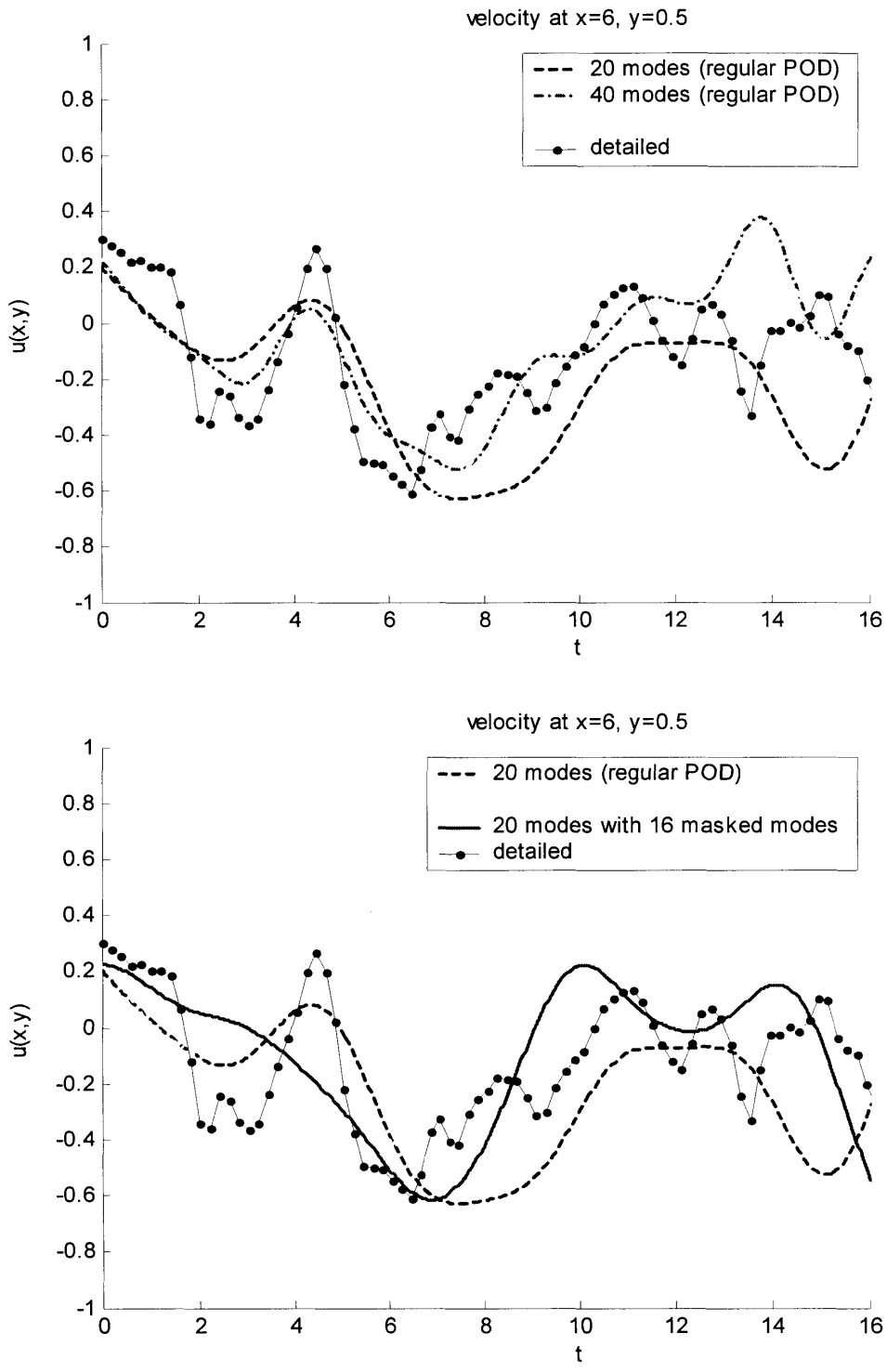

Figure 37 Streamwise velocity tracking at $x = 6$, $y = 0.5$. Note that the step lies at $x = 4$ in Figure 13. Model based on 20 modified basis functions: solid; 20 standard basis functions: dashed; 40 standard basis functions: dash-dot; detailed simulation result: solid/dotted at sampling points

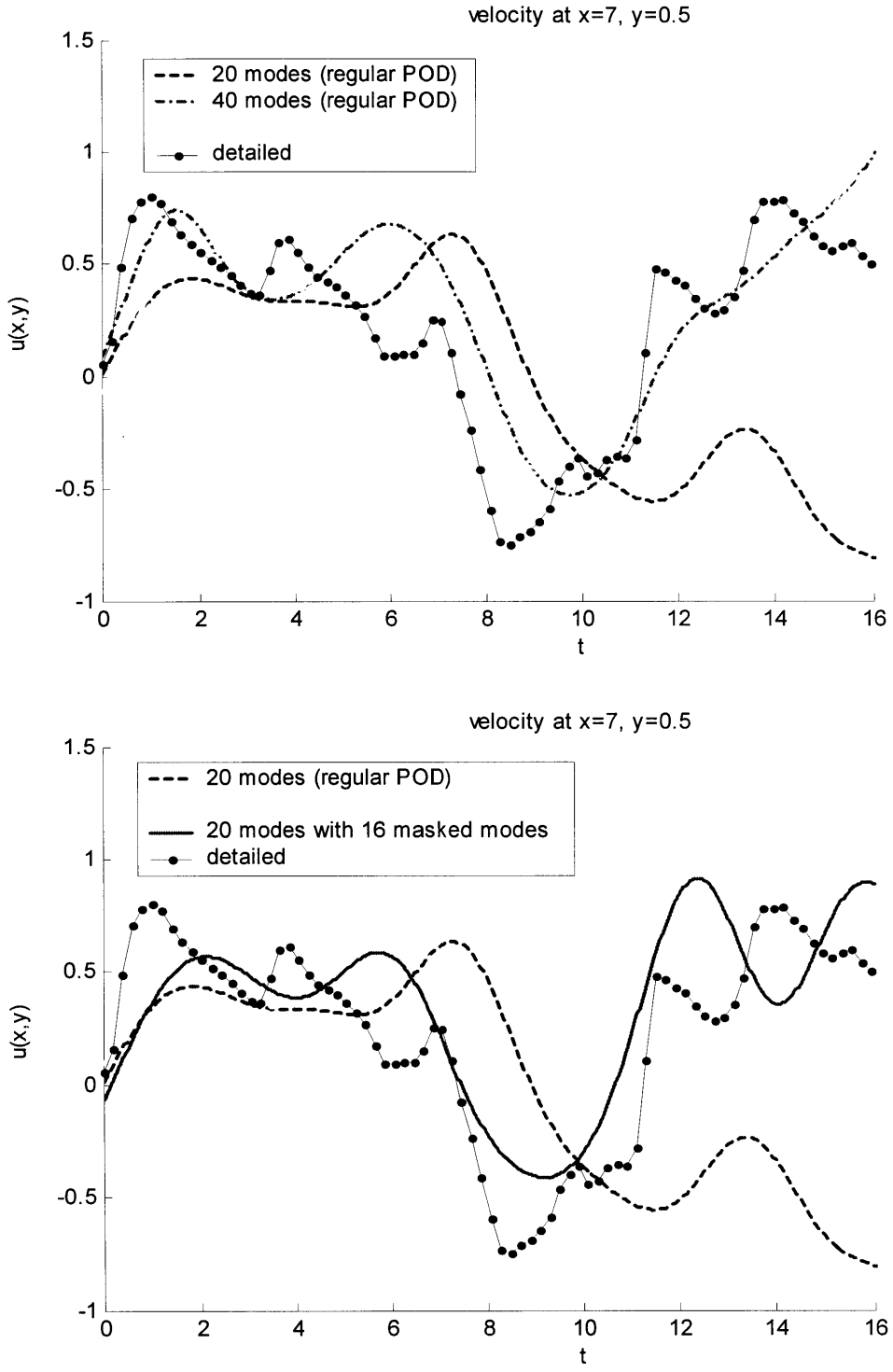

Figure 38 Streamwise velocity tracking at $x = 7$, $y = 0.5$. Note that the step lies at $x = 4$ in Figure 13. Model based on 20 modified basis functions: solid; 20 standard basis functions: dashed; 40 standard basis functions: dash-dot; detailed simulation result: solid/dotted at sampling points

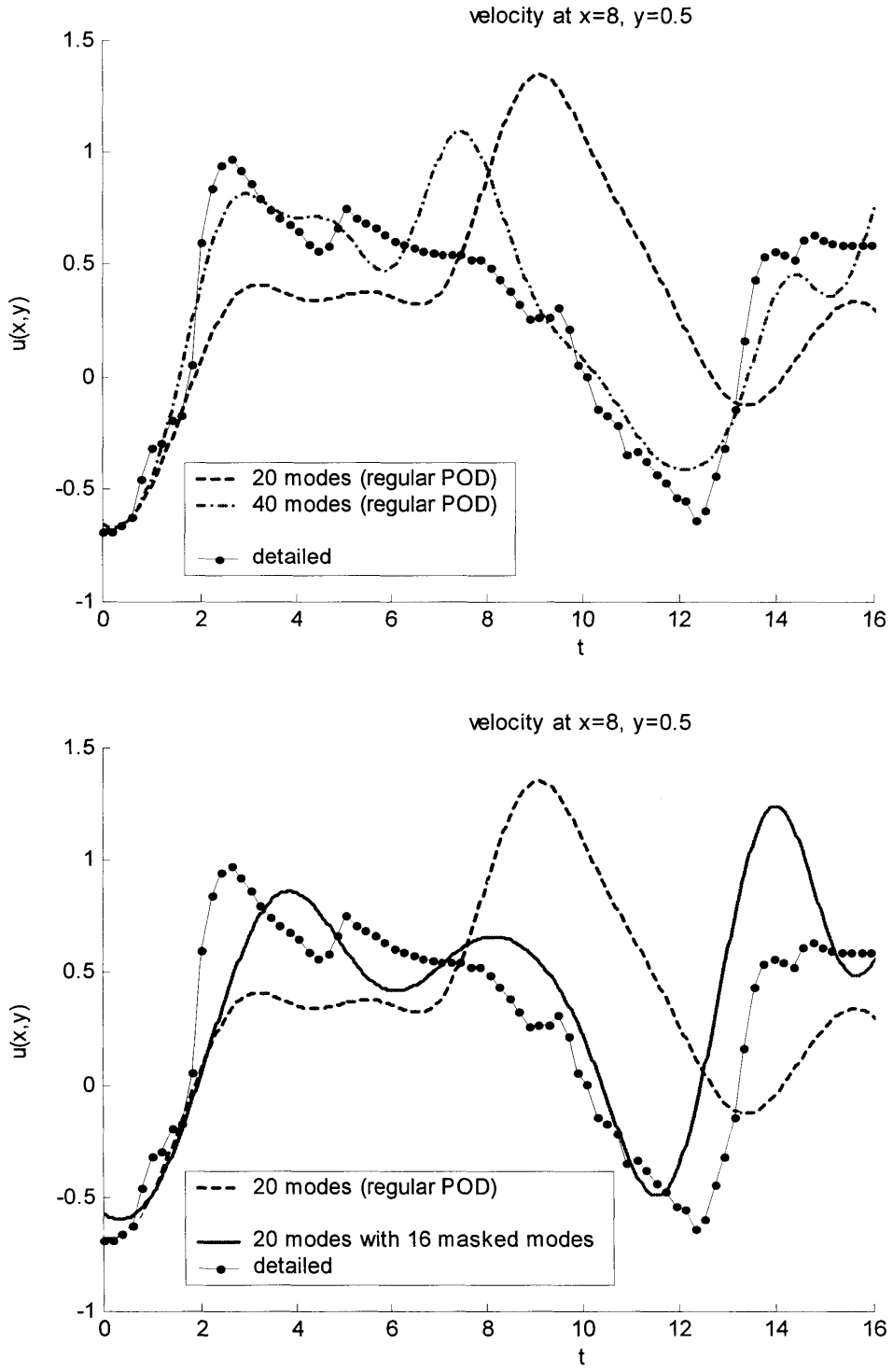

Figure 39 Streamwise velocity tracking at $x = 8$, $y = 0.5$. Note that the step lies at $x = 4$ in Figure 13. Model based on 20 modified basis functions: solid; 20 standard basis functions: dashed; 40 standard basis functions: dash-dot; detailed simulation result: solid/dotted at sampling points

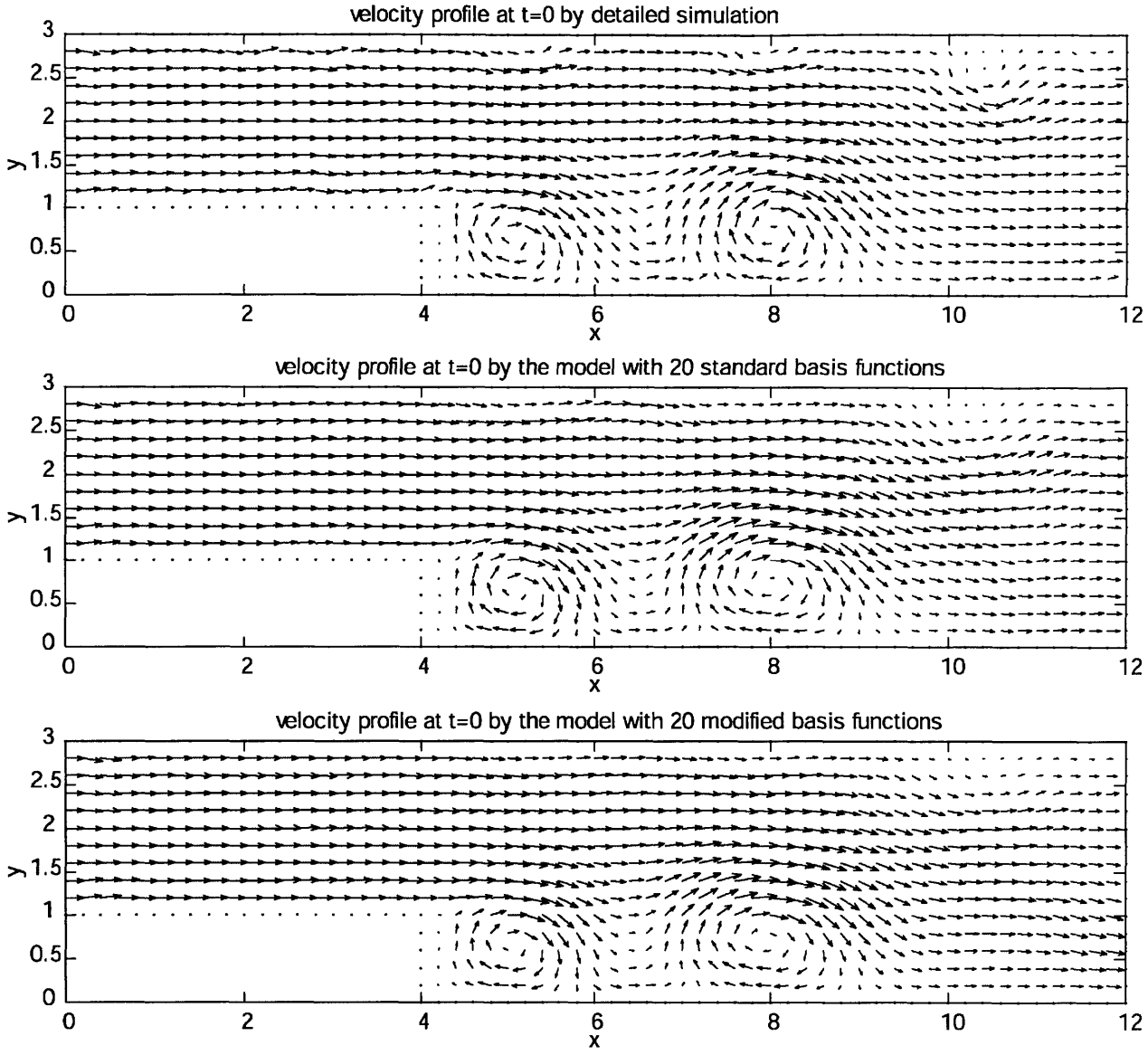

Figure 40 Velocity field at $t = 0$. Both reduced order models reproduce the large scale structures shown in the detailed simulation results reasonably well.

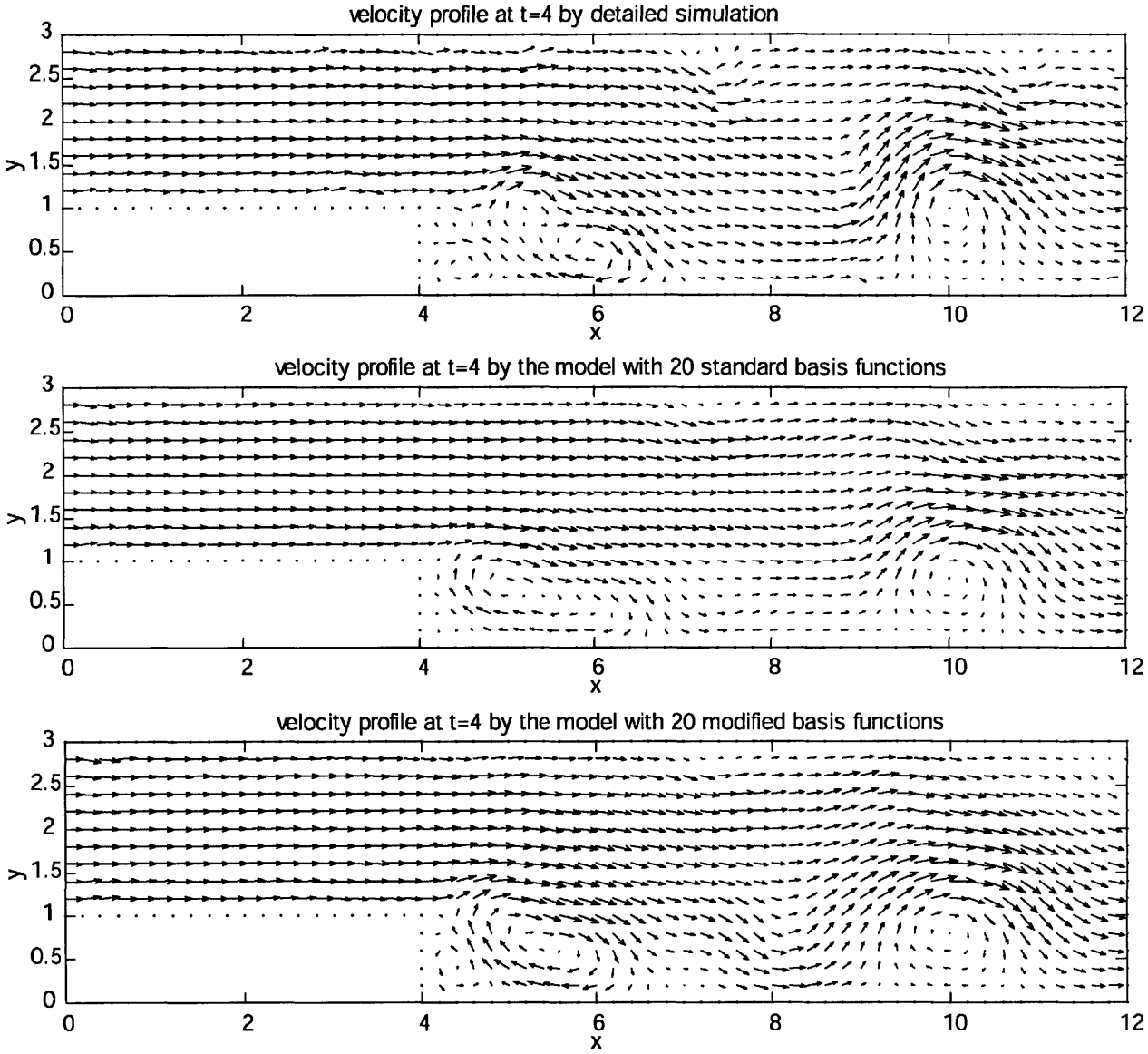

Figure 41 Velocity field at $t = 4$. Both reduced order models reproduce the large scale structures shown in the detailed simulation results near the recirculation zone.

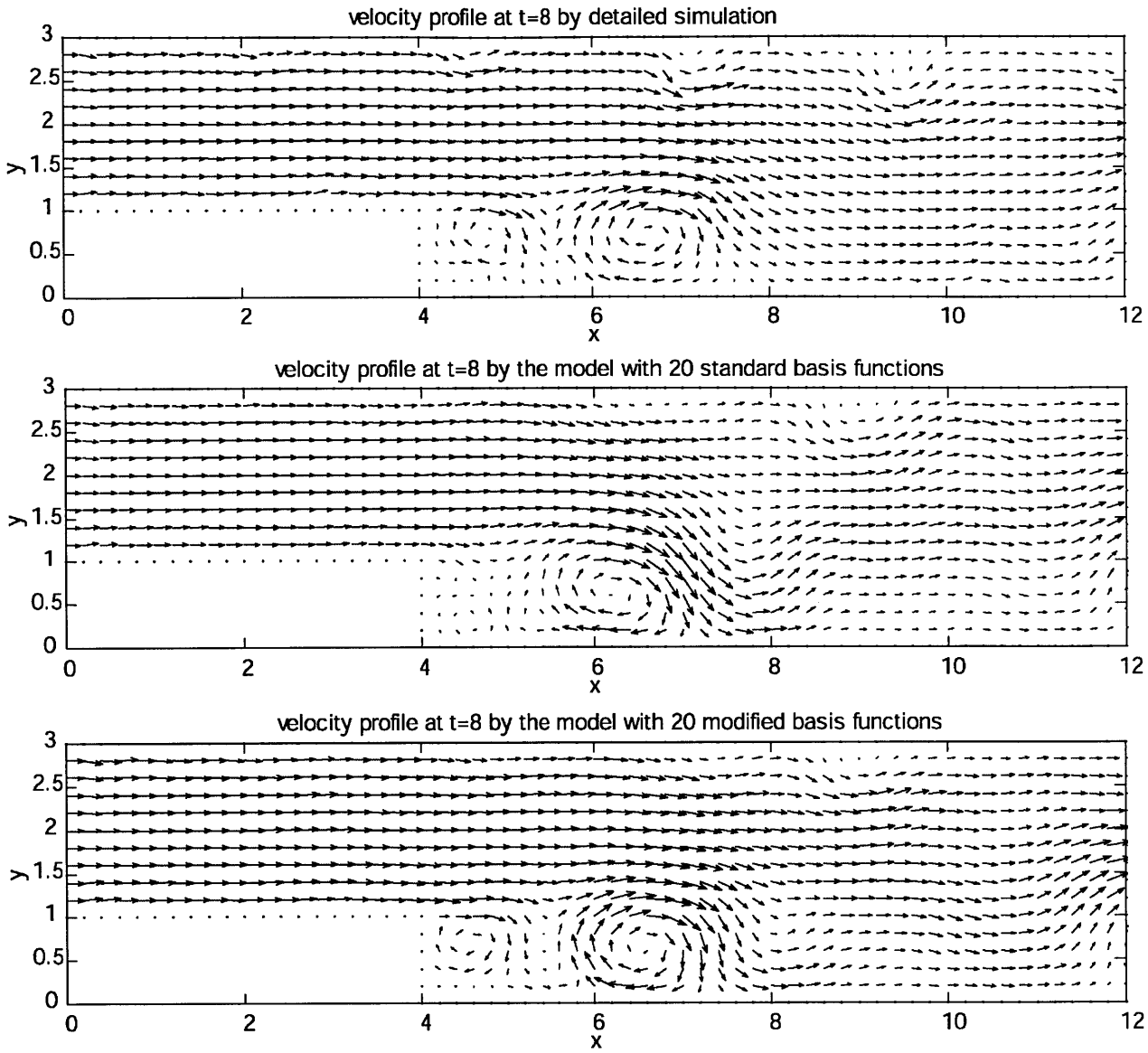

Figure 42 Velocity field at $t = 8$. All the models show two vortices rotating clockwise, but the one based on standard basis functions fails to show the relative strength of those two, i.e. the eddy near the step is very weak. The result of detailed simulation shows relative strength of these vortices similar to that observed in detailed simulation.

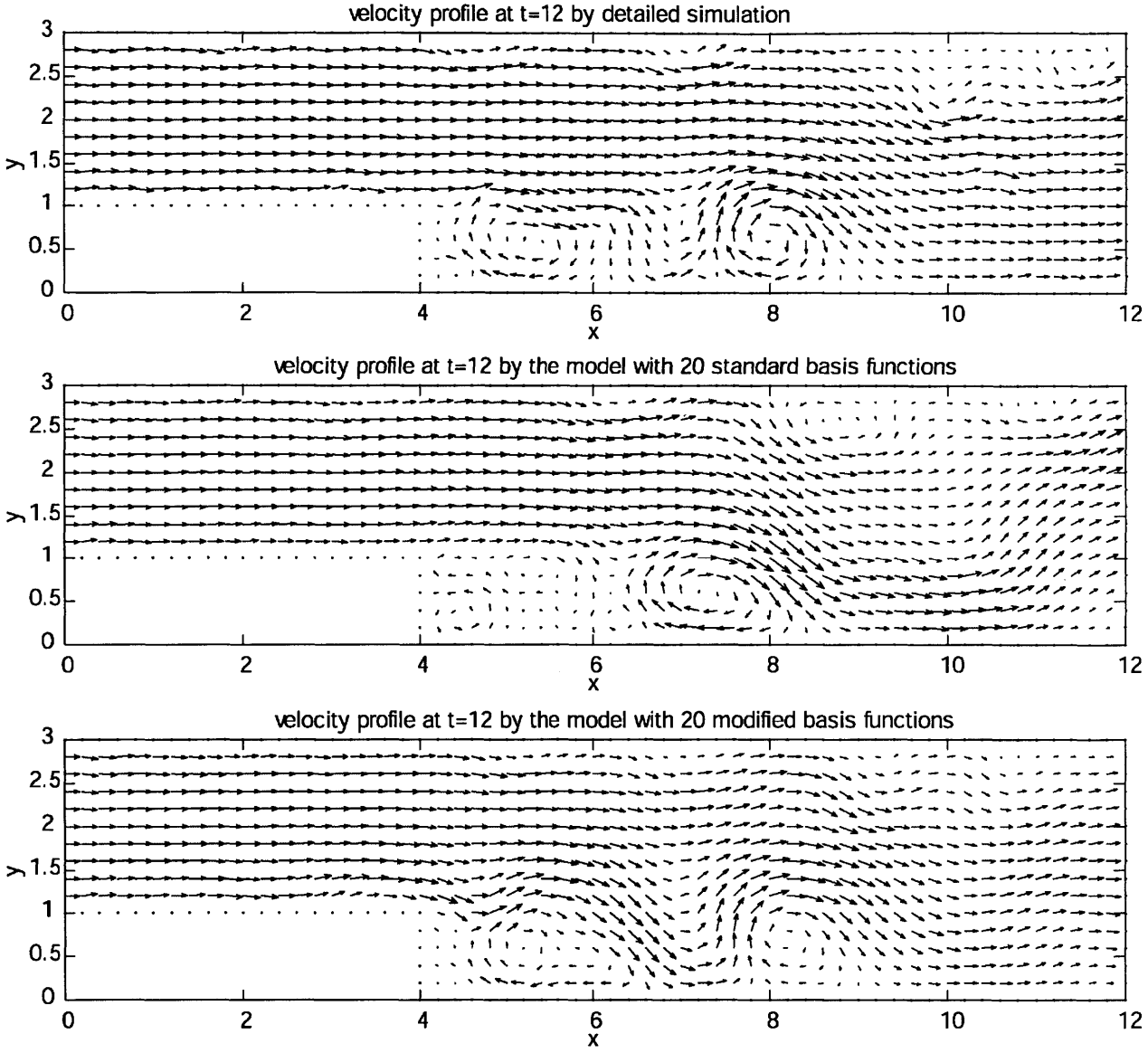

Figure 43 Velocity field at $t = 12$. The model based on standard basis functions shows a very different structure from the result of detailed simulation. The model based on modified basis functions still shows two vortices rotating clockwise at $x = 5$ and $x = 8$, which are also observed in the result of detailed simulation.

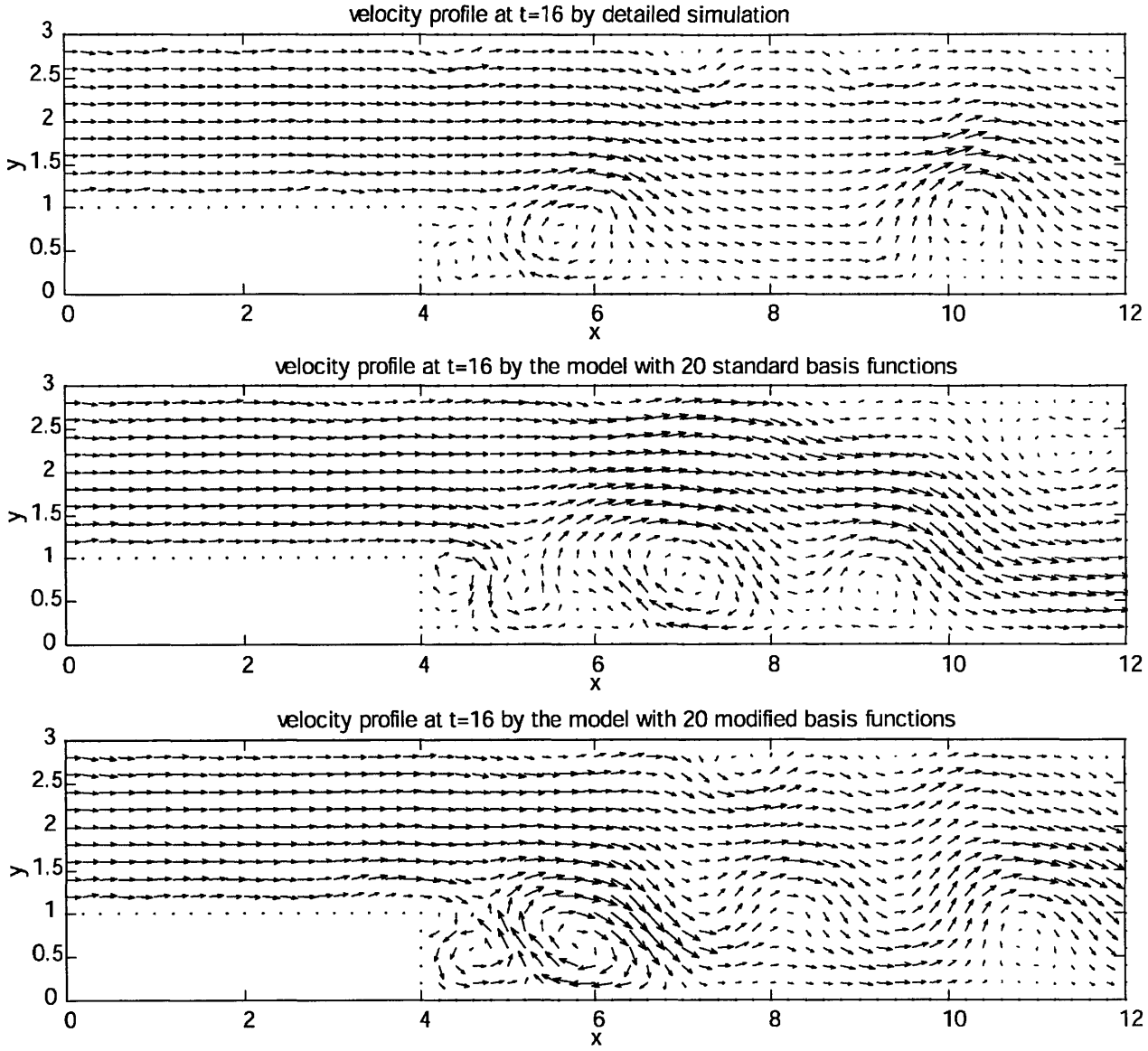

Figure 44 Velocity field at $t = 16$. Although both reduced order models show quite different structures from the result of detailed simulation for the overall domain, the model based on modified basis functions still shows two counter-rotating large vortices near the step, which are similar to the ones observed in detailed simulation result.

IV Conclusions

In this thesis, the possibility that a hydrodynamic mechanism may introduce self-sustained oscillations in a combustor is examined. Motivated by several observations in the literature where combustion instability is reported to occur at multiple frequencies, conditions under which unstable hydrodynamic modes can be present and cause combustion instability are investigated.

In Chapter II, using linear stability analysis of separating shear layers, we have shown that under conditions most often encountered in non reacting and reacting flows downstream a backward facing step, the flow possesses instability modes which may lead to self-sustained hydrodynamic oscillations. The associated frequencies are determined by the shear flow properties, e.g., the shear layer thickness, the amount of backflow, the temperature or density across the shear zone, and the offset between the shear and burning zones. The analysis is used to explain results of numerical simulations of non reacting flows which exhibit strong unsteadiness at frequencies close to those predicted for certain modes, and is shown to match the frequency of pressure oscillation observed in experimental investigations of a backward-facing step combustor approximately.

Based on the reasoning given in Chapter II, we developed reduced order models of this type flows in Chapter III. POD-Galerkin procedure based on numerical data is carried out to determine an overall combustion dynamics model that accurately represents the effect of shear-layer instability so as to carry out a model-based control design. During the process, the problem of extended domain of numerical simulation and the issue of boundary conditions are addressed, and the 'nested weighting procedure' is proposed as the solution. While the main focus of the thesis has been on backward-facing step flows, the tools introduced here are applicable for more general configurations.

References

[1] B.T. Zinn, Pulsating Combustion. Advanced Combustion Methods. Academic Press, 1986.

[2] F. Culick, "Combustion Instabilities in Liquid-Fueled Propulsion Systems," AGARD Conference Proceedings, Paper 1, 450, 1988.

[3] M. Fleifil, A.M. Annaswamy, Z.A. Ghoneim and A.F. Ghoniem, "Response of a Laminar Premixed Flame to Flow Oscillations: A Kinematic Model and Thermoacoustic Instability Results," Combustion and Flame, vol. 106, issue 4, pp.487-510, 1996.

[4] A.M. Annaswamy, M. Fleifil, J.P. Hathout and A.F. Ghoniem, "Impact of Linear Coupling on the Design of Active Controllers for the Thermoacoustic Instability," Combust. Sci. and Tech., vol. 128, pp.131-180, 1997.

[5] T. Lieuwen, Y. Neumeier and B. T. Zinn., "The Role of Unmixedness and Chemical Kinetics in Driving Combustion Instabilities in Lean Premixed Combustors," Combust. Sci. and Tech., vol. 135, pp.193-211, 1998.

[6] A.P. Dowling, "A Kinematic Model of a Ducted Flame," J. Fluid Mech., vol. 394, pp51-72, 1999.

[7] S. Park, A.M. Annaswamy and A.F. Ghoniem, "Heat Release Dynamics Modeling for Combustion Instability Analysis of Kinetically Controlled Burning," AIAA 2001-0780, 39th Aerospace Sciences Meeting and Exhibit, 2001.

[8] J.O. Keller, L. Vaneveld, D. Korschelt, G.L. Hubbard, A.F. Ghoniem, J.W. Daily, and A.K. Oppenheim, "Mechanism of Instabilities in Turbulent Combustion Leading to Flashback," AIAA J., vol. 20, pp.254-262, 1982.

[9] S.R.N. DeZilwa, J.H. Uhm and J.H. Whitelaw, "Combustion Oscillations Close to the Lean Flammability Limit," Combust. Sci. and Tech, vol. 160, pp.231-258, 2000.

[10] K.C. Schadow, E. Gutmark, T.P. Parr, D.M. Parr, K.J. Wilson, and J.E. Crump, "Large-Scale Coherent Structures as Drivers of Combustion Instability," Combust. Sci. and Tech., vol. 64, pp.167-186, 1989.

[11] C.O. Paschereit, W. Weisenstein and E. Gutmark, "Role of Coherent Structures in Acoustic Combustion Control," AIAA 98-2433, 29th AIAA Fluid Dynamics Conference, 1998.

[12] C.O. Paschereit, E. Gutmark and W. Weisenstein, "Reduction of Pressure Oscillations by Direct Excitation of Gas–Turbine Burner's Shear Layer," AIAA 2000-1028, 38th Aerospace Sciences Meeting and Exhibit, 2000.

[13] J.M. Cohen and T.J. Anderson, "Experimental Investigation of Near–Blowout Instabilities in a Lean, Premixed Step Combustor," AIAA 96-0819, 34th Aerospace Sciences Meeting & Exhibit, 1996.

[14] R.W. Pitz and J.W. Daily, "Combustion in a Turbulent Mixing Layer Formed at a Rearward–Facing Step," AIAA J., vol. 21, pp.1565–1570, 1983.

[15] D.M. Driver, H. Lee Seegmiller and J.G. Marvin, "Time-Dependent Behavior of a Reattaching Shear Layer," AIAA J., vol. 25, pp.914–919, 1983.

[16] A.F. Heenan and J.F. Morrison, "Passive Control of Backstep Flow," Experimental Thermal and Fluid Science, vol. 16, pp.122–132, 1988.

[17] H.N. Najm and A.F. Ghoniem, "Numerical Simulation of the Convective Instability in a Dump," AIAA J., vol. 29, pp.911-919, 1991.

[18] P. Huerre and P.A. Monkewitz, "Absolute and Convective Instabilities in Free Shear Layers," J. Fluid Mech., vol. 159, pp.151–168, 1985.

[19] P. Huerre and P.A. Monkewitz, "Local and Global Instabilities in Spatially Developing Flows," Ann. Rev. Fluid Mech., vol. 22, pp.473-537, 1990.

[20] P.G. Drazin and W.H. Reid, Hydrodynamic Stability, Cambridge University Press, 1981.

[21] P.J. Schmid and D.S. Henningson, Stability and Transition in Shear Flows, Springer Verlag, 2001.

[22] K. Kupfer, A. Bers, and A.K. Ram, "The Cusp Map in the Complex-Frequency Plane for Absolute Instabilities," Phys. Fluids, vol. 30, pp.3075-3082, 1987.

[23] C. Fureby, "Large Eddy Simulation of Rearward-Facing Step Flow," AIAA J., vol. 37, pp.1401-1410, 1999.

[24] H. Le, P. Moin and J. Kim, "Direct Numerical Simulation of Turbulent Flow over a Backward-Facing Step," J. Fluid Mech., vol. 330, pp.349-374, 1997.

[25] L. Kaiktsis, G.E. Karniadakis and S.A. Orszag, "Unsteadiness and Convective Instabilities in Two-Dimensional Flow over a Backward-Facing Step," J. Fluid Mech. vol. 321, pp.157-187, 1996.

[26] L. Kaiktsis, G.E. Karniadakis and S.A. Orszag, "Onset of 3-Dimensionality, Equilibria, and Early Transition in Flow over a Backward-Facing Step," J. Fluid Mech., vol. 231, pp. 501-528, 1991.

[27] L. Lees and C.C. Lin, "Investigation of the Stability of the Laminar Boundary Layer in a Compressible Fluid," NACA TN 1115, 1946.

[28] M.C. Soteriou and A.F. Ghoniem, "Effects of the Free-Stream Density Ratio on Free and Forced Spatially Developing Shear Layers," Phys. Fluids, vol. 7, pp. 2036-2051, 1995.

[29] P. Bakewell and J.L. Lumley, "Viscous Sublayer and Adjacent Wall Region in Turbulent Pipe Flows," Phys. Fluids, vol. 10, pp. 1880-1889, 1967.

[30] P. Holmes, L. Lumley and G. Berkooz, Turbulence, Coherent Structures, Dynamical Systems and Symmetry, Cambridge University Press, 1996.

[31] S.S. Ravindran, "A Reduced-Order Approach to Optimal Control of Fluids Using Proper Orthogonal Decomposition," Int. J. Numer. Meth. Fluids, vol. 34, pp.425-448, 2000.

[32] W.R. Graham, J. Peraire and K.Y. Tang, "Optimal Control of Vortex Shedding Using Low-Order Models. Part I - Open-Loop Model Development," Int. J. Numer. Meth, Eng., vol. 44, pp.945-972, 1999.

[33] E. Hopf, "On Nonlinear Partial Differential Equations," Lecture Series of the Symposium on Partial Differential Equations, Berkeley, edited by N. Aronszajn and C.B. Morrey, Jr., 1955.

[34] D. Remfer, "On Dynamical Systems Obtained via Galerkin Projections onto Low-Dimensional Bases of Eigenfunctions," Fundamental Problematic Issues in Turbulence, edited by A. Gyr, W. Kinzelbach and A. Tsinober, Birkhäuser Verlag, 1999.

[35] R. Temam, Navier-Stokes Equations: Theory and Numerical Analysis, AMS, 2001; 1st ed. published in 1979.

[36] J. Sethian and A.F. Ghoniem, "Validation of the Votex Method," J. Comput. Phys., vol. 74, pp.283-317, 1988.

[37] L.F. Shampine and M.W. Reichelt, "The Matlab ODE Suite," SIAM J. Sci. Computt., vol. 18, pp.1-22, 1997.

[38] B.I. Epureanu and E.H. Dowell, "Reduced Order System Identification of Nonlinear Aeroelastic Systems," Proceedings of 1st MIT Conference on Computational Fluid and Solid Mechanics, vol.2, pp. 1158-1162, Elsevier Science, 2001.